

SCALING OF MIXING IN STIRRED TANK CRYSTALLIZATION
REACTORS

by

David McKinnon

Submitted in partial fulfilment of the requirements
for the degree of Master of Applied Science

at

Dalhousie University
Halifax, Nova Scotia
March 2023

© Copyright by David McKinnon, 2023

TABLE OF CONTENTS

TABLE OF CONTENTS.....	ii
LIST OF TABLES	v
LIST OF FIGURES	viii
ABSTRACT	xiii
LIST OF ABBREVIATIONS AND SYMBOLS USED.....	xiv
ACKNOWLEDGEMENTS	xxi
CHAPTER 1: INTRODUCTION	1
1.1. INTRODUCTION.....	1
1.2. OBJECTIVES	3
1.3. THESIS ORGANIZATION.....	4
1.4. SIGNIFICANCE OF THE CURRENT WORK.....	5
CHAPTER 2: BACKGROUND	6
2.1. INTRODUCTION.....	6
2.2. EXPERIMENTAL METHODS FOR CHARACTERIZING FLUID DYNAMICS	6
2.3. CHEMICAL METHODS TO ANALYZE MIXING.....	9
2.4. MODELLING FLUID DYNAMICS	14
2.5. MODELLING MICROMIXING	16
2.6. INTEGRATION INTO CFD.....	19
2.7. SUMMARY.....	26
CHAPTER 3: METHODOLOGY.....	27
3.1. EXPERIMENTAL METHODOLOGY	27
3.1.1. Iodide-Iodate Reaction Background and Analysis	27
3.1.2. Experimental Setup and Procedure.....	29
3.1.3. List of Experiments.....	34
3.1.4. Experimental Results and Discussion.....	35
3.2. MODELLING METHODOLOGY	38
3.2.1. Flow Fields and Turbulence Modelling.....	38
3.2.2. Competitive-Parallel Reactions	40
3.2.3. Scales of Mixing and Mixing Times.....	47
3.2.4. Engulfment Model.....	49

3.3. SIMULATION SEQUENCE	50
3.3.1. Steady-State Flow Field	51
3.3.2. Power Number	51
3.3.3. Competitive-Parallel Reactions	51
3.3.4. Numerical Solvers and Schemes	52
3.4. SUMMARY	53
CHAPTER 4: MODELLING FLUID DYNAMICS IN STIRRED TANKS	55
4.1. INTRODUCTION	55
4.2. BLAIS CASE	55
4.2.1. Geometry	55
4.2.2. Case Setup and Meshing	57
4.3. CHAPPLE CASE	60
4.3.1. Geometry	60
4.3.2. Case Setup and Meshing	62
4.4. RESULTS AND DISCUSSION	67
4.4.1. Mesh Refinement Study	68
4.4.2. Relative Baffle Position	70
4.4.3. Power Number Predictions	71
4.5. SUMMARY	75
CHAPTER 5: VALIDATION OF THE REACTIVE MIXING SOLVER	76
5.1. INTRODUCTION	76
5.2. LIU AND FOX CASE	76
5.2.1. Geometry	77
5.2.2. Case Setup and Meshing	77
5.3. ASSIRELLI CASE	81
5.3.1. Geometry	81
5.3.2. Case Setup and Meshing	83
5.4. AKITI CASE	87
5.4.1. Geometry and Mesh	87
5.4.2. Case Setup	89
5.5. RESULTS AND DISCUSSION	91
5.5.1. Conversion in CIJR	91
5.5.2. Mesh Dependence Study in CIJR	98

5.5.3. Reaction Zone Sensitivity in CIJR	102
5.5.4. Mixing Power in Stirred Tank Reactors	108
5.5.5. Conversion of Mixing Sensitive Reactions in Stirred Tank Reactors	110
5.6. SUMMARY.....	114
CHAPTER 6: MODELLING OF COMPETITIVE-PARALLEL REACTIONS IN SMALL-SCALE CRYSTALLIZATION REACTORS	115
6.1. INTRODUCTION.....	115
6.1.1. Geometry.....	115
6.1.2. Case Setup and Meshing	116
6.1.3. Case Setup.....	119
6.2. RESULTS AND DISCUSSION	121
6.2.1. Yield in Mixing Sensitive Reactions	121
6.2.2. Mesh Dependence Study in Crystallization Reactors	123
6.2.3. Mixing times.....	125
6.2.4. Reaction Zone.....	129
6.2.5. Time Dependent Measurements	132
6.2.6. Sensitivity to Mixing Parameters	133
6.3. SUMMARY.....	135
CHAPTER 7: CONCLUSIONS AND RECOMMENDATIONS	136
7.1. CONCLUSIONS	136
7.2. FUTURE WORK.....	138
REFERENCES.....	139

LIST OF TABLES

Table 2.1:	Summary of the reactive mixing models and turbulence models in recent CFD studies.....	21
Table 3.1:	Dimensions of the stirred tank crystallization reactor used in this work. ...	31
Table 3.2:	Summary of the concentrations used in the experiments.....	33
Table 3.3:	Summary of the sampling procedure during acid dosing.	34
Table 3.4:	Summary of the full list of experiments.....	35
Table 4.1:	Dimensions used in the Blais case study.....	56
Table 4.2:	Computational mesh used in the Blais pitched blade impeller case study.	58
Table 4.3:	Boundary conditions used in Blais stirred tank validation cases.....	59
Table 4.4:	Fluid properties used in the Blais case study.	60
Table 4.5:	Initial conditions used in the Blais case study.....	60
Table 4.6:	Dimensions for the pitched blade impeller and Rushton turbine Chapple case study.....	62
Table 4.7:	Computational meshes used in the Chapple pitched blade impeller and Ruston turbine cases.	63
Table 4.8:	Mesh dependence study for the Chapple case using pitched blade turbine.	65
Table 4.9:	Mesh dependence study for Very Fine Mesh Chapple case using pitched blade turbine.....	66
Table 4.10:	Fluid properties used in the Chapple cases.	66
Table 4.11:	Initial conditions used in the Chapple Rushton turbine cases.	67
Table 4.12:	Initial conditions used in the Chapple pitched blade turbine cases.	67
Table 4.13:	Ratio of power number predictions determined by impeller torque or volume integration of the turbulent energy dissipation rate.....	73
Table 5.1:	Meshes used for the Liu and Fox case.	78
Table 5.2:	Very fine mesh used for the Liu and Fox case.	79
Table 5.3:	Boundary conditions used for the Liu and Fox steady-state flow cases. ...	80
Table 5.4:	Summary of Conditions for the Simulated Cases from Liu and Fox	80
Table 5.5:	Boundary conditions used for the Liu and Fox cases.	80
Table 5.6:	Liquid properties used for the Liu and Fox cases.....	81
Table 5.7:	Dimensions used in the Assirelli et al. Rushton turbine case.....	82
Table 5.8:	Computational meshes used in the Assirelli case.....	84

Table 5.9:	Liquid properties used for the Assirelli case.	85
Table 5.10:	Initial conditions for the incompressible turbulent flow simulations in the Assirelli Rushton turbine cases.	85
Table 5.11:	Boundary and initial conditions used for the Assirelli steady-state incompressible turbulent flow simulations.	86
Table 5.12:	Boundary and initial conditions used for the Assirelli reactive mixing simulations.	86
Table 5.13:	Initial concentrations and volumetric flow rate used in the Assirelli cases.	87
Table 5.14:	Dimensions used in the Akiti case.	88
Table 5.15:	Computational meshes used for the Akiti case.	89
Table 5.16:	Boundary conditions used for the Akiti cases.	90
Table 5.17:	Boundary and initial conditions used for the reactive mixing Akiti case.	90
Table 5.18:	Initial conditions used in the Akiti case.	90
Table 5.19:	Liquid properties used for the Akiti case.	91
Table 5.20:	Initial concentrations, volumetric flow rate, and reaction rate constant used for the Akiti cases.	91
Table 5.21:	Segregation zone impact on mean energy dissipation rate for $Re = 1\ 000$ and $t_r = 317$ ms.	103
Table 5.22:	Segregation zone impact on mean energy dissipation rate for $Re = 400$ and $1\ 000$ for $t_r = 317$ ms using a cut-off variance ratio.	107
Table 6.1:	Dimensions used in the stirred tank crystallization reactor.	116
Table 6.2:	Mesh quality for the stirred tank crystallization reactor case.	118
Table 6.3:	Boundary conditions used for the steady-state incompressible flow cases.	119
Table 6.4:	Boundary and initial conditions used for the stirred tank crystallization reactor case.	119
Table 6.5:	Initial field conditions specified for the stirred tank crystallization reactor case.	120
Table 6.6:	Liquid properties used for the stirred tank crystallization reactor case. ...	120
Table 6.7:	Initial concentrations in the stirred tank crystallization reactor case.	120
Table 6.8:	Initial concentration of injected acid and source terms for each Reynolds number used in the stirred tank crystallization reactor cases. ...	121
Table 6.9:	Impact of grid size on segregation index for $Re = 25000$ and $C_{A0} = 400$ mol/m ³ using each mesh summarized in Table 6.2.	125

Table 6.10:	Segregation zone impact on mean energy dissipation rate for $Re = 8333-25000$ and $C_{A0} = 400 \text{ mol/m}^3$ with various cut-off variance ratio on the intermediate mesh.....	132
-------------	--	-----

LIST OF FIGURES

Figure 3.1:	Reactor geometry with the 50 mm retreat curve impeller showing feeding locations close to the impeller (black dot) and just below the free surface (red dot).....	30
Figure 3.2:	Images showing the feeding locations close to the impeller blade tip for both impeller types. The top of the blade tip and feed tube outlet is in line with the 100 mL graduation mark.....	31
Figure 3.3:	Schematic diagram of the dosing system for the EasyMax402 reactor with feed additions made through a PTFE 1/8 in OD (3.175 mm), 1/16 in ID (1.59 mm) tube positioned for dosing close to the impeller and just below the free surface.....	32
Figure 3.4:	Relationship between UV spectrum of the samples drawn from the EasyMax during acid dosing and segregation index. UV spectrum (left) varying with respect to wavelength where triiodide corresponds to 353 nm. Segregation index and UV at 353 (right) as a function of time.	36
Figure 3.5:	Relationship between segregation index X_S and concentration of acid for fixed Reynolds numbers. Solid black lines indicate the main set of experiments performed using the retreat curve impeller and feeding close to the impeller. The grey dotted line indicates the additional set of experiments where subsurface dosing was performed. The grey dashed line indicates the dataset obtained using pitched blade impeller. ...	37
Figure 3.6:	Segregation index X_S varying as a function of Reynolds number for fixed concentration of acid.....	37
Figure 4.1:	Geometry used in the Blais case study.....	56
Figure 4.2:	Visual description of boundary conditions and mesh interface between rotating and stationary domains. The size of rotating domain was chosen such that its boundary is halfway between the impeller tip in the radial direction and two blade widths above and below in the axial direction.....	59
Figure 4.3:	Geometries used in the Chapple case study: (i) side view of the pitched blade impeller case, (ii) side and top views of Rushton turbine cases where impeller blade thickness was varied ($e = 0.00089$ m and 0.00259 m).....	61
Figure 4.4:	Meshes used in the Chapple Rushton turbine cases showing $e/D = 0.034$ (left) and $e/D = 0.011$ (right).....	64
Figure 4.5:	Effect of the number of computational mesh cells on predicted power number with $Re = 1\ 000$ (A) and $Re = 60\ 000$ (B).....	68
Figure 4.6:	Distributions of turbulent energy dissipation rate in the Chapple pitched blade impeller case at Reynolds number of 60 000. Mesh	

	length scale of 0.0025 m (A), 0.002 m (B), 0.0016 m (C), and 0.0009 m (D).	69
Figure 4.7:	Effect of computational mesh on predicted velocity profiles with $Re = 60\,000$ (left) and predicted velocity profiles for $Re = 100\,000$ (right).	70
Figure 4.8:	Effect of the baffle position relative to impeller on predicted power number for the Chapple PBT case with $Re = 4\,000$	71
Figure 4.9:	Effect of baffle position on predicted velocity profiles for the Chapple PBT case with $Re = 4\,000$	71
Figure 4.10:	Power number curve for the pitched blade turbine Blais case.	72
Figure 4.11:	Comparison of power number predictions with experimental data from Chapple et al. (2002) for a pitched bladed turbine impeller. Simulations were performed using the Mid Mesh.	74
Figure 4.12:	Power number curve for both Rushton turbine Chapple cases with varying blade thicknesses. Triangles: $e/D = 0.034$ (2.59 mm). Diamonds: $e/D = 0.011$ (0.89 mm).	75
Figure 5.1:	Geometry used for Liu and Fox (2006) confined impinging jet reactor case using the fourth Bourne reaction scheme.	77
Figure 5.2:	Geometry used for the Assirelli et al. (2002) stirred tank reactor simulations.	82
Figure 5.3:	Geometry of the six-blade downward-pumping 45° pitched blade turbine of the Akiti and Armenante (2004) case.	88
Figure 5.4:	Impact of characteristic reaction time on the conversion of reactant D in the competitive-parallel reactions varying with respect to jet Reynolds number: logarithmic vertical scale (left) and linear vertical scale (right).	92
Figure 5.5:	Distribution of segregation zones for $Re_j = 400$ (left) and $Re_j = 1\,000$ (right). Both use $\sigma = 0.0112$, intermediate mesh, and $t_r = 317$ ms.	94
Figure 5.6:	Distribution of segregation zones for (left to right) $Re_j = 400$ and $Re_j = 1\,000$. Distribution of turbulent kinetic energy dissipation rate in the segregation zones (top row) and distribution of turbulent kinetic energy dissipation rate on the symmetry plane (bottom row). Segregation zones use $\sigma = 0.0112$. Intermediate mesh was used in the analysis.	95
Figure 5.7:	CFD predictions of the mean energy dissipation and DMP conversion varying with respect to jet Reynolds number.	96
Figure 5.8:	Turbulent energy dissipation rate distribution for (left column) intermediate mesh at a fixed $Re_j = 400$ and $t_r = 317$ ms and (right column) intermediate mesh at $Re_j = 1\,000$, $t_r = 317$ ms. All use $\sigma = 0.0112$. Mean values of ε are shown as red dashed lines.	97

Figure 5.9:	DMP conversion (X_D) varying with number of cells for coarse mesh, intermediate mesh, fine mesh, and ultra fine mesh at $Re_j = 1\ 000$ and $t_r = 317$ ms.	98
Figure 5.10:	Distribution of the reaction and segregation zones for $Re_j = 1\ 000$ and $t_r = 317$ ms for coarse mesh (left), intermediate mesh (middle), and fine mesh (right).	99
Figure 5.11:	Turbulent energy dissipation rate distribution for (left column) coarse mesh and (right column) fine mesh at a fixed $Re_j = 1\ 000$ and $t_r = 317$ ms. Mean of ε is shown as red dashed lines.	100
Figure 5.12:	Turbulent energy dissipation rate distribution for (left column) intermediate mesh and (right column) very fine mesh at a given $Re_j = 1\ 000$ and $t_r = 317$ ms. Mean of ε is shown as red dashed lines.	101
Figure 5.13:	Distribution of the reaction and segregation zones for $Re_j = 1\ 000$ and $t_r = 317$ ms using the intermediate mesh for $\sigma = 0.00976$ (left), $\sigma = 0.0112$ (middle), and $\sigma = 0.01525$ (right).	103
Figure 5.14:	Sensitivity of distribution of the turbulent energy dissipation rate in each segregation zone for $Re_j = 1\ 000$ and $t_r = 317$ ms for $\sigma = 0.00976$ (left column), $\sigma = 0.0112$ (middle column), and $\sigma = 0.01525$ (right column).	104
Figure 5.15:	Sensitivity of distribution of the turbulent energy dissipation rate in each segregation zone for $Re_j = 1\ 000$ and $t_r = 317$ ms for $\sigma = 0.00488$ (left column), $\sigma = 0.0112$ (middle column), and $\sigma = 0.0305$ (right column).	105
Figure 5.16:	Distribution of turbulent energy dissipation rate for $Re_j = 400$ (left) and $Re_j = 1\ 000$ (right) and $t_r = 317$ ms.	106
Figure 5.17:	Distribution of segregation zones for $Re_j = 400$ (left) and $Re_j = 1\ 000$ (right) and $t_r = 317$ ms and $a_2/a_{2,max} \geq 0.01$	106
Figure 5.18:	Average turbulent energy dissipation rate of different zones as a function of mixing time (left axis) and conversion (right axis). Simulations used the intermediate mesh with $t_r = 317$ ms.	108
Figure 5.19:	Comparisons between the experimental and simulated power number values for the Assirelli et al. case with varying Reynolds number (left) and varying with grid size (right) for the coarse mesh, intermediate mesh, and fine mesh for $N = 552$ rpm ($Re = 85\ 970$).	109
Figure 5.20:	Comparisons between the experimental and simulated power number values for the Akiti case varying with Reynolds Number (left) and varying with the number of cells (right) for a fixed Reynolds number ($Re = 69\ 360$).	110
Figure 5.21:	Comparisons between the experimental and simulated segregation index (X_S) for the Assirelli case varying Re ($N = 300, 420, 522, 552$	

	rpm) (left) and varying with grid size for the coarse mesh, intermediate mesh, and fine mesh (right) at a fixed $Re = 85\,970$ ($N = 552$ rpm).....	111
Figure 5.22:	Distribution of turbulent kinetic energy dissipation rate for the Assirelli case with $Re = 46\,722$ (left) and $Re = 85\,969$ (right).	112
Figure 5.23:	Comparison of E-model implementation with simulation results from Duan et al. (2016) showing depletion of component A during the first addition of feed element for fixed Re ($N = 300$ and 420 rpm) for the Assirelli case.....	112
Figure 5.24:	Comparisons between the experimental and simulated X_{S2} for the Akiti case varying with Re ($N = 100, 200, 300, 400$ rpm) (left) and varying with grid size for coarse mesh, intermediate mesh, and fine mesh (right) at a fixed $Re = 69\,360$ ($N = 400$ rpm).	113
Figure 5.25:	Comparisons between the simulated Duan et al. (2016) data and simulated E-model X_S for the Akiti case sensitivity to environment volume changes with self-engulfment (left) and sensitivity to environment volume changes without self-engulfment (right).	114
Figure 6.1:	Geometry of the EasyMax402 reactor with the retreat curve impeller used in experiments for this work.....	116
Figure 6.2:	Comparisons between the experimental and simulated segregation index values for the crystallization stirred tank with varying injection acid concentration for $Re = 8333$ (top left), $Re = 16667$ (top right), and $Re = 25000$ (bottom) for the intermediate mesh summarized in Table 6.2.	122
Figure 6.3:	Impact of varying Courant number on segregation index in the stirred tank crystallization reactor case using the intermediate mesh shown in Table 6.2. Reynolds number of $16\,667$ and acid concentration of 200 mol/m^3	123
Figure 6.4:	Impact of varying cell number on segregation index in the stirred tank crystallization reactor case using the meshes shown in Table 6.2. Reynolds number of $16\,667$ and acid concentration of 400 mol/m^3	124
Figure 6.5:	Impact of varying Reynolds number on global blend time in the stirred tank crystallization reactor case using the intermediate mesh shown in Table 6.2. Simulations performed over the range of Reynolds number of $2\,083$ – $33\,333$, corresponding to stirring speeds of $50, 100, 200, 400, 600,$ and 800 rpm.	126
Figure 6.6:	Small-scale segregation mixing time t_{SSS} for $Re = 8\,333, 16\,667,$ and $25\,000$ with the intermediate mesh.	127
Figure 6.7:	DQMOM-IEM predictions of the mean mixing time as a function of average energy dissipation compared to the reduced order model of Bourne and Baldyga (1989).	128

Figure 6.8:	Turbulent energy dissipation rate distribution in the reaction zone for the crystallization reactor case for variance ratio 1×10^{-6} at $Re = 16\ 667$ (top left), variance ratio 1×10^{-5} at $Re = 16\ 667$ (top middle), variance ratio 1×10^{-3} at $Re = 16\ 667$ (top right), variance ratio 1×10^{-6} at $Re = 25\ 000$ (bottom left), variance ratio 1×10^{-5} at $Re = 25\ 000$ (bottom middle), and variance ratio 1×10^{-3} at $Re = 25\ 000$ (bottom right). All simulations use the intermediate mesh.	130
Figure 6.9:	Turbulent energy dissipation rate distribution for the crystallization reactor case averaged over the full tank (transparent black), averaged over the reaction zone using a variance ratio of 1×10^{-4} (red), averaged over the reaction zone using a variance ratio of 1×10^{-3} (green), averaged over the reaction zone using a variance ratio of 1×10^{-2} (blue), averaged over the reaction zone using a variance ratio of 1×10^{-1} (solid black). Reynolds number $Re = 8\ 333$ (200 rpm left) using intermediate mesh. Reynolds number $Re = 25\ 000$ (600 rpm right) using intermediate mesh.	131
Figure 6.10:	Turbulent energy dissipation rate distribution for the crystallization reactor case averaged over the full tank and averaged over the reaction zone by matching variance ratio. Reynolds number $Re = 8\ 333$ (200 rpm), $16\ 667$ (400 rpm) and $25\ 000$ (600 rpm) using intermediate mesh.	131
Figure 6.11:	Segregation index varying as a function of crystallization reactor case using the intermediate mesh summarized in Table 6.2.....	133
Figure 6.12:	Effect of E-model predictions with and without self-engulfment on predicted segregation index X_S for Reynolds number $Re = 16\ 667$ (400 rpm).....	134
Figure 6.13:	Effect of empirical mixing coefficient C_ϕ on predicted segregation index X_S for Reynolds Number $Re = 16\ 667$	135

ABSTRACT

A solver was developed in OpenFOAM to simulate fluid dynamics and competitive-parallel reactions in stirred tank crystallization reactors. The model uses the direct quadrature method of moments (DQMOM) coupled with the interaction-by-exchange-with-the-mean (IEM) model to estimate global mixing sensitive reaction yields. Model development and validation was completed for one small-scale confined impinging jet reactor (CIJR) and two larger-scale stirred tank reactors that utilized the third Bourne, fourth Bourne, and Villermaux-Dushman reactions. Experimental Villermaux-Dushman reaction yield measurements were collected in a small-scale EasyMax 402 crystallization reactor and compared with the implemented DQMOM-IEM model predictions. Experimental measurements were performed using a 50 mm retreat curve, near-impeller dosing with sulfuric acid concentration of 100–400 mol/m³, and impeller speeds of 200–600 rpm. Although the DQMOM-IEM solver predictions are in good agreement with experimental trends, it is necessary to adjust the mechanical-to-scalar (C_ϕ) empirical mixing coefficient to obtain good fits for some cases.

LIST OF ABBREVIATIONS AND SYMBOLS USED

Abbreviations

$B(OH)_4^-$	Borate ion
$B(OH)_3$	Boric acid
CAD	Computer-aided design (software)
CFD	Computational Fluid Dynamics
DMP	2,2-dimethoxypropane
CIJR	Confined impinging jet reactor
DQMOM	Direct quadrature method of moments
EDD	Engulfment-deformation-diffusion
E-model	Engulfment model
GAMG	Geometric-algebraic multi-grid (solver)
GC	Gas chromatography
H^+	Hydrogen ion
H_2SO_4	Sulfuric Acid
HCl	Hydrochloric acid
HPLC	High performance liquid chromatography
I^-	Iodide ion
IO_3^-	Iodate ion
I_2	Iodine
I_3^-	Triiodide
IEM	Interaction by exchange with the mean
IO_3^-	Iodate ion
KI	Potassium iodide
KIO_3	Potassium iodate
LDA	Laser Doppler anemometry
LES	Large Eddy Simulations
LSS	Large-scale segregation
NaOH	Sodium hydroxide
OpenFOAM	Open-source Field Operation and Manipulation (software)
PDF	Probability density function

PIV	Particle Image Velocimetry
PLIF	planar laser-induced fluorescence
RANS	Reynolds-Averaged Navier-Stokes
RC	Retreat curve
RSM	Reynolds stress model
RTD	Residence time distribution
SALOME	CFD pre-processing software
SIMPLE	Semi-Implicit Momentum Linked Equations
SSS	Small-scale segregation

Symbols

∇p	pressure gradient (Pa)
$\nabla \bar{u}$	Mean velocity gradient (s^{-1})
$(\nabla \bar{u})^T$	Transpose of mean velocity gradient (s^{-1})
\bar{a}	Mean mixture fraction (m^3/m^3)
a_1	Mixture fraction (m^3/m^3)
a_2	Mixture fraction variance (m^3/m^3)
$a_{2,1}$	Mixture fraction variance in the inertial-convective subrange (m^3/m^3)
$a_{2,2}$	Mixture fraction variance in the viscous-convective subrange (m^3/m^3)
$a_{2,3}$	Mixture fraction variance in the viscous-diffusive subrange (m^3/m^3)
$a_{2,max}$	Maximum LSS variance (m^3/m^3)
a_3	LSS variance (m^3/m^3)
B	Baffle width (m)
C	Off-bottom clearance (m)
$C_{1\varepsilon}$	Model constant for $k-\varepsilon$ turbulence model (-)
$C_{2\varepsilon}$	Model constant for $k-\varepsilon$ turbulence model (-)
$C_{i\infty}$	Concentration of component i in the local environment of the growing eddy (mol/m^3)
C_{i10}	Surrounding concentration of component i for the incorporation model (mol/m^3)
C_i	Concentration of component i (mol/m^3)
$C_{i\infty}$	Concentration of component i in the local environment of the growing eddy (mol/m^3)

C_ϕ	Empirical mixing coefficient
C_μ	Model Constant for Turbulent Viscosity (-)
C_{Ak}	Local concentration of component A in fluid environment k (mol/m ³)
C_{A0}	Initial concentration of component A (mol/m ³)
\overline{C}_A	Average concentration of component A in both environments (mol/m ³)
C_A	Time varying concentration of component A based on reduced-order engulfment model
$C_{A\infty}$	Environment concentration of component A based on reduced-order engulfment model (mol/m ³). Updates between feed addition steps.
C_{Bk}	Local concentration of component B in fluid environment k (mol/m ³)
C_{B0}	Initial concentration of component B (mol/m ³)
\overline{C}_B	Average concentration of component B in both environments (mol/m ³)
C_B	Time varying concentration of component B based on reduced-order engulfment model (mol/m ³)
$C_{B\infty}$	Environment concentration of component A based on reduced-order engulfment model (mol/m ³). Updates between feed addition steps.
C_{Dk}	Local concentration of component D in fluid environment k (mol/m ³)
C_{D0}	Initial concentration of component D (mol/m ³)
\overline{C}_D	Average concentration of component D in both environments (mol/m ³)
$\overline{\overline{C}}_D$	mass-weighted average concentration of component D in both environments (mol/m ³)
C_D	Time varying concentration of component D based on reduced-order engulfment model (mol/m ³)
$C_{D\infty}$	Environment concentration of component D based on reduced-order engulfment model (mol/m ³)
C_{P1k}	Local concentration of component P ₁ in fluid environment k (mol/m ³)
C_{P10}	Initial concentration of component P ₁ (mol/m ³)
\overline{C}_{P1}	Average concentration of component P ₁ in both environments (mol/m ³)
C_{P1}	Time varying concentration of component P ₁ based on reduced-order engulfment model (mol/m ³)
$C_{P1\infty}$	Fixed environment concentration of component P ₁ based on reduced-order engulfment model (mol/m ³)
$\overline{\overline{C}}_{P1}$	mass-weighted average concentration of component P ₁ in both environments (mol/m ³)
C_{P2k}	Local concentration of component P ₂ in fluid environment k (mol/m ³)

C_{P20}	Initial concentration of component P ₂ (mol/m ³)
$\overline{C_{P2}}$	Average concentration of component P ₂ in both environments (mol/m ³)
C_{P2}	Time varying concentration of component P ₂ based on reduced-order engulfment model (mol/m ³)
$C_{P2\infty}$	Fixed environment concentration of component P ₂ based on reduced-order engulfment model
$\overline{\overline{C_{P2}}}$	mass-weighted average concentration of component P ₂ in both environments (mol/m ³)
D	Impeller diameter (m)
D_{disk}	Impeller disk diameter (m)
D_{hub}	Impeller hub diameter (m)
D_T	Mass diffusivity coefficient (1×10^{-9} m ² /s)
D_{shaft}	Impeller shaft diameter (m)
Da_{II}	Second Damköhler number (-)
E	Engulfment parameter (s ⁻¹)
e	Impeller blade thickness (m)
$g(t)$	Model growth function for the incorporation model (m ³ /s)
G_k	Turbulent kinetic energy production rate (m ² /s ³)
H	Liquid reactor height and chamber height (m)
H_F	Axial feed position (m)
H_{hub}	Impeller hub height (m)
k_2	Rate constant of reaction 2 (various units: s ⁻¹ or mol ¹² /m ¹² /s)
k	Turbulent kinetic energy (m ³ /s ²)
K_B	Equilibrium constant of iodine, iodide, and triiodide reaction (L/mol)
L	Impeller blade length (m)
M	Impeller torque (N m)
N	Impeller rotation frequency (s ⁻¹)
N_p	Power Number (-)
$N_{p,\varepsilon}$	Turbulent kinetic energy dissipation rate-based Power Number (-)
$N_{p,M}$	Torque based Power Number (-)
P_ε	Turbulent kinetic energy dissipation rate-based Power (W)
P_M	Torque based Power (W)

r_F	Radial position of feed addition point (m)
R_1	Tank bottom radius for crystallization reactor (m)
R_2	Tank bottom radius for crystallization reactor (m)
R_2	Reaction rate of reaction 2 (mol/s)
Re	Reynolds number (-)
Re_t	Local turbulent Reynolds number (-)
$S_{2\infty}$	Source term of reaction 2 coupled to an infinitely-fast reaction 1 (s^{-1})
Sc_t	Turbulent Schmidt number (-)
t	Time (s)
t_{eng}	Mixing time based on the engulfment model (s)
t_{LSS}	Large scale segregation decay time (s)
t_m	Characteristic micromixing time for incorporation model (s)
t_r	Characteristic reaction time (s)
t_{mix}	Characteristic micromixing time (s)
$\overline{t_{mix}}$	Mean micromixing time (s)
t_{SSS}	Small-scale segregation decay time (s)
T	Internal tank diameter (m)
T	Temperature (K)
\vec{u}	Mean velocity vector (m/s)
V	Reactor volume (m^3)
V_{cell}	Computational cell volume (m^3)
V_e	Volume of the reaction zone in E-model (m^3)
V_{inj}	Injection volume (m^3)
V_{tank}	Tank volume (m^3)
W	Molecular Weight (kg/kmol)
W_b	Impeller Blade width (m)
X_1	Mixture fraction in the first environment of the DQMOM-IEM model (m^3/m^3)
X_2	Mixture fraction in the second environment of the DQMOM-IEM model (m^3/m^3)
X_D	Conversion of reactant D (m^3/m^3)
X_{S2}	Yield of product P_2 in the third Bourne reaction (m^3/m^3)

X_S	Selectivity or segregation index (m^3/m^3)
X_{Sk}	Stoichiometric mixture fraction (m^3/m^3)
$Y_{r,n}$	Reaction progress variable for reaction r in the n environment (m^3/m^3)
Y_{ST}	Maximum yield (m^3/m^3)
Y	Yield (m^3/m^3)
Z	CIJR chamber length (m)

Greek Letters

α_1	Volume fraction of the first environment in the DQMOM-IEM model (m^3/m^3)
α_2	Volume fraction of the second environment in the DQMOM-IEM model (m^3/m^3)
ε	Turbulent Kinetic Energy Dissipation Rate (m^2/s^3 or W/kg)
δ	CIJR outlet diameter
γ	Micromixing Time Parameter (s^{-1})
μ	Dynamic Viscosity of the fluid (Pa s or kg/m/s)
ν	Kinematic Viscosity of the fluid (m^2/s)
ν_t	Turbulent Kinematic Viscosity of the fluid (m^2/s)
π	Ratio of the Circumference of a Circle to its Diameter (-)
ρ	Fluid density (kg/m^3)
σ	Cut-off point for defining regions in the flow field (m^3/m^3)
σ_k	Model constant
σ_ε	Model constant
τ	Stress-rate tensor (s^{-1})
τ_G	Characteristic mixing time in the inertial-convective subrange (s)
τ_s	Characteristic meso-mixing time for E-model (s)

Subscripts

0	Initial Value
i	Components ($i = A, B, C, D, E, T, P_1, P_2$)
j	Feed (or parcel) addition number for engulfment model
k	Environment indicator
n	Fluid environment number

r Reaction number
 ∞ Surrounding

ACKNOWLEDGEMENTS

First, I would like to acknowledge my supervisor, Dr. Jan Haelssig, for his support, guidance and mentoring through my degree.

Subsequently, I would like to thank my committee members, Dr Adam Donaldson, Dr. Quan (Sophia) He, and Dr. Stanislav Sokolenko for reading my thesis and providing thoughtful feedback and suggestions.

Additionally, I would like to thank my colleagues for their expertise, experience sharing and help. Especially, I would like to thank Dr. Mahmoud Mirmehrabi, Dr. Sam Tadayon, Pavan Batchu and Eric Torrey at Solid State Pharma, who supported me throughout my degree and helped me set up and perform my experiments.

Finally, I would like to thank my wife, Madisen McKinnon, family, and friends for their love and support throughout my life.

CHAPTER 1: INTRODUCTION

1.1. Introduction

Mixing plays an important role in many industries due to its effect on product properties. Poor mixing in pharmaceutical crystallization can result in undesired product quality in terms of inconsistent particle size distribution, poor morphology, and entrapment of impurities. Poor mixing can also result in inconsistencies in the polymorphic form if regions of high local levels of supersaturation form, as well as increased costs due to difficult scale-up protocols and process development (Kresta et al., 2016). In crystallization, the intensity and uniformity of macromixing and micromixing affects particle morphology and particle size distribution. In the case of parallel-competitive reactions, poor mixing can raise the amount of undesired product while lowering the yield and purity of desired products. Improving understanding of mixing processes is necessary for reliable estimates of yield, purity, and reaction rate during scale-up. When developing computational fluid dynamics (CFD) models to assess the impact of mixing on particle properties formed during crystallization, characterizing local mass transfer and reaction rates should be a first step. In this work, the specific goals are to characterize mixing in stirred tank crystallization reactors at various scales and to develop a validated CFD model that can accurately predict these effects.

The use of stirred tank reactors is common for product development and large-scale processing in the pharmaceutical industry. Stirred tank reactors that rely on mechanical agitation can have zones with inefficient mixing, especially for fast precipitation reactions that are prone to mass-transfer limitations. This makes design and scale-up of reactors for new drug candidates challenging when existing infrastructure relies on these units. The use of microreactors is becoming an increasingly popular alternative during development due to their smaller confined dimensions that promotes more efficient and uniform mixing. In general, these smaller chemical reactors are favourable compared to stirred tank reactors because they achieve smaller diffusion lengths for mass transport, as well as more uniform distribution of mixing rate and energy dissipation and have shorter characteristic mixing times. However, such reactors are prone to plugging when used for crystallization, and therefore stirred tanks continue to be the dominant configuration for this type of process.

The application of CFD as a tool to analyze reactor performance during scale-up allows for estimates of local fluid dynamics and transport processes in various systems. Therefore, CFD has the potential to mitigate economic impact as it relates to process design of new drug candidates and/or conducting costly experiments.

Much CFD research has focused on investigating mixing at the microscopic/molecular scale (i.e., micromixing) in reactors given its importance for scale-up of stirred tank reactors (Cheng et al., 2016; Duan et al., 2016). Evaluating the impact of mixing on precipitation and crystallization processes through CFD models is becoming a reasonable option relative to sometimes costly experiments. In the late 90s and extending into the 2000s, the research group lead by Fox developed and validated a direct-quadrature-method-of-moments (DQMOM) coupled with an interaction-by-exchange-with-the-mean (IEM) model for determining local mixing times (Liu & Fox, 2006). This DQMOM-IEM model has since been used to simulate competitive-parallel reactions for characterizing mixing in various systems including confined impinging jet reactors (Gavi et al., 2007; Marchisio, 2009) and stirred tank reactors (Duan et al., 2018, 2019). The model has also been extended by Marchisio and Barresi (2003) to evaluate precipitation processes using a range of solvents (Lavino et al., 2021; Para et al., 2022). Yang and colleagues reviewed and highlight the importance of micromixing models that have been implemented historically as it relates to chemical reactors (Mao & Yang, 2017), stirred tank reactors (Cheng et al., 2012), and more recently, antisolvent crystallization processes (Qu et al., 2021).

Chemical methods for assessing micromixing performance have been developed for both flow and batch systems. They rely on the selectivity of competitive-parallel or -series reactions, which can be correlated with the micromixing efficiency. The reaction rate must be chosen strategically such that the selectivity is strongly impacted by mixing in the system of interest. The iodide-iodate (Fournier et al., 1996; Guichardon & Falk, 2000), third Bourne (Akiti & Armenante, 2004; Bourne & Yu, 1994), and fourth Bourne reactions (Baldyga et al., 1998) have been used to characterize micromixing performance in stirred tanks. In this work, the iodide-iodate test system, also known as the Villermaux-Dushman

reactions, was chosen for the experiments due to the ability to easily measure by-product triiodide (I_3^-) concentration using a spectrophotometer.

1.2. Objectives

The primary objective of this work was to develop a custom solver in the OpenFOAM (Open-source Field Operation and Manipulation) software package to simulate competitive-parallel reactions for characterizing reactive mixing in stirred tank reactors. The solver is intended to be used to model fluid dynamics, mass transfer, and chemical reactions in stirred tank crystallization reactors. This development required validation in two steps. First, validation of predicted pseudo steady-state flow fields and turbulence parameters of single-phase incompressible Newtonian flow fields was performed. Subsequently, validation of predicted yield predictions of mixing sensitive competitive-parallel reactions was completed. The first validation was done by direct comparison of power number and local velocity profile model predictions with several experimental case studies of various geometries from literature. The second validation step was achieved through direct comparison of experimental yield measurements of mixing sensitive reactions in both continuous flow systems and batch reactors. Experimental data was gathered by performing in-house competitive-parallel reaction experiments, and data drawn from literature investigations was also used for comparison and validation.

The developed model was utilized to perform computational analysis of single-phase flow and mixing performance analysis in one continuous flow and three stirred tank reactor geometries: confined impinging jet reactor of Liu and Fox (2006), stirred tank reactor of Akiti and Armenante (2004), stirred tank reactor of Assirelli et al. (2002), and the EasyMax reactor from this work. The purpose of these investigations was to apply the implemented CFD model over a broad range of geometries and conditions and draw insight into the predictability of multi-scale mixing processes in various systems to aid in developing scale-up strategies that relate to anti-solvent crystallization. A summary of the specific objectives for this work is as follows:

- Compile past and current modelling techniques that have been used to simulate competitive-parallel reactions. Additionally, evaluate experimental approaches to

compare turbulent energy dissipation rate in small and large-scale stirred tank reactors that can be used to evaluate model performance.

- Validate fluid flow and turbulence predictions in stirred tank reactors by direct comparison with power number and local velocity profiles to data gathered from literature. At the same time, verify the meshing strategy by comparing predictions made using multiple reference frame (MRF) and sliding mesh approaches for the impeller region.
- Develop a new OpenFOAM solver to predict micromixing performance by evaluating micromixing times and competitive-parallel reaction yields.
- Verify the CFD solver using experimental data from literature.
- Conduct experiments varying initial reactant concentration and impeller speed to characterize mixing rate and reaction rate independently for a small-scale 300 mL EasyMax stirred tank reactor. Use these experimental data to perform further model validation.
- Consolidate and expand commonly used postprocessing methods that integrate simple mechanistic micromixing models with CFD to evaluate micromixing performance.

1.3. Thesis Organization

This thesis is divided into seven chapters. Chapter 2 summarizes important literature related to characterizing hydrodynamics and mixing sensitive reaction modelling in stirred tank reactors. Chapter 3 outlines the experimental methodology, including the application of the Villermaux-Dushman reaction scheme. Chapter 3 also contains solver development, including transport equations employed to evaluate reaction yield and mixing times. An overview of the reduced-order E-model and its implementation in MATLAB is also provided. Chapter 4 contains the fluid dynamics validation studies performed by comparing predictions to the experimental measurements of power number and local velocity profiles of Chapple et al. (2002). Chapter 4 also includes the fluid dynamics validation of model power number predictions by comparing to the simulation and experimental results of Blais et al. (2016), which includes both MRF and sliding mesh techniques. Chapter 5 contains reaction model validation for the fourth Bourne

competitive-parallel using experimental and simulation data for flow through a confined impinging jet reactor (Johnson & Prud'homme, 2003; Liu & Fox, 2006). Chapter 5 also expands the model developments from continuous flow to batch and contains reaction model validation using experimental and simulation data for chemical reactions and turbulent mixing in larger-scale stirred tank reactors that use the third Bourne and Villiermaux-Dushman reaction schemes. This chapter also includes postprocessing techniques and expands the analysis commonly used in literature investigations. Chapter 6 contains reaction model verification using experimental measurements collected in this work for the Villiermaux-Dushman reaction scheme in a smaller-scale EasyMax 402 reactor and a retreat curve impeller. Chapter 6 also includes blend times, micromixing times, and attempts to relate local mixing times to global mixing with the purpose of assisting scale-up procedures. Chapter 7 summarizes the conclusions and recommendations of this work.

1.4. Significance of the Current Work

The scientific contributions resulting from this work are as follows:

1. The coupling of the incompressible steady-state flow field and turbulence model to the DQMOM-IEM reactive mixing model in OpenFOAM to evaluate micromixing times in stirred tank reactors.
2. Verification and validation of the newly developed solver using continuous flow systems and batch reactors. Mesh dependence studies apply full-cycle monitoring of both flow parameters and yield parameters. Comprehensive evaluations of key mixing parameters and their impact on CFD results.
3. Development of a novel method to post-process reaction zone data based on the distribution of turbulent kinetic energy dissipation rate that provides a link between 1D models and CFD investigations.

CHAPTER 2: BACKGROUND

2.1. Introduction

A brief overview of experimental and numerical approaches that have been adopted in literature for characterizing fluid dynamics and micromixing performance in stirred tank reactors is presented in this chapter. First, a summary of experimental techniques for evaluating mixing performance using dimensional analysis and chemical methods is presented. The methods described focus on techniques that can be compared with CFD model prediction for validation. Second, a summary of modelling techniques applied in CFD to predict yield of mixing sensitive competitive-parallel reactions is provided.

2.2. Experimental Methods for Characterizing Fluid Dynamics

Mixing is controlled by three parallel mechanisms: macromixing, mesomixing, and micromixing. Macromixing is the largest scale of mixing and is often characterized by the residence time distribution (RTD) of a tracer in continuous reactors or by the blend time in batch reactors. Macromixing represents the bulk blending of material in the reactor. Global blend time in stirred tank reactors is often determined by injection of a tracer and is the time that it takes for the tracer signal to dissipate below 5% of the injected value. Conversely, micromixing is the smallest scale of mixing and occurs in the smallest eddies below the Kolmogorov scale at the molecular level. Micromixing is the final step in mixing before contact of two molecules for reaction. Micromixing is influenced by deformation, engulfment, and molecular diffusion (Bałdyga & Pohorecki, 1995). Mesomixing can be described as the time to dissipate the feed plume by turbulent dispersion and disintegration of large eddies. Mesomixing occurs at a time scale between macro and micromixing, which makes it relevant to stirred tank reactors when reagents are dosed through a pipe. To maintain product quality and selectivity of desired products, reactors should be operated to avoid mixing-limited conditions or mixing should be as uniform as possible. The impact of mixing limitations can be managed by operating with a mixing rate that is fast and uniform through the reactor due to the strong dependence on turbulent energy dissipation rate. This section provides a summary of the necessary background on mixing and flow field generation by impellers studied in this thesis.

A typical stirred tank reactor consists of a cylindrical tank equipped with rectangular baffles and a rotating impeller in the centre (Chapple et al., 2002). In literature, a standard configuration consists of a flat or curved reactor bottom, four baffles connected to the reactor walls, and a liquid height typically set to the diameter of the tank. The distance from the bottom of the tank to the impeller is referred to as the clearance of the impeller. Typical investigations employ a Rushton turbine, a downward pumping pitched blade impeller, or an upward pumping pitched blade impeller. Retreat curve impellers are commonly used in crystallization because they provide more gentle mixing, but they are often neglected in literature investigations of fluid dynamics, scaling, and mixing performance. Various impellers were investigated in this thesis either by simulation or experimental studies. These include standard and non-conventional stirred tank reactors using Rushton turbines, standard reactors using downward pumping pitched blade impellers, and a curved bottom crystallization reactor equipped with a three-blade retreat curve impeller without baffling.

The mixing power is an important design parameter for stirred tank reactors and is strongly dependent on the turbulent intensity of the flow. Flow conditions are usually divided into three operating regimes: laminar, transition, and turbulent. These operating regimes are assessed by the Reynolds number. In stirred tank reactors, the characteristic length scale is the impeller diameter, and the characteristic velocity scale is based on the impeller tip speed. The Reynolds number for stirred tank reactors is expressed as follows:

$$\text{Re} = \frac{\rho ND^2}{\mu} \quad (2.1)$$

where Re is the Reynolds number (-), ρ is the fluid density (kg/m^3), N is the impeller rotation frequency (s^{-1}), D is the impeller diameter (m), μ is the fluid viscosity (Pa s), and the product ND is the impeller tip speed (m/s). Flows operating at $\text{Re} < 10$ are said to be laminar, $\text{Re} > 20\,000$ is fully turbulent, and transition occurs when Re is between laminar and turbulent conditions. Many industrial reactors are operated under fully turbulent conditions, but turbulent intensity often varies locally through the vessel.

Another dimensionless number commonly used to characterize fluid dynamics is related to the power consumption. The power consumption, also known as power draw or mixing

power, is the power delivered to the fluid by the rotating impeller. For the scaling of pharmaceutical crystallization processes, power per unit volume of fluid is often the key parameter. Different approaches have been used to aid scale-up, including specific power, mixing time, and impeller tip speed; however, due to the variability in geometry and tank reactor shapes, literature correlations often fail as they strongly depend on the flow fields used in the specific stirred tank system (Nienow, 2014). Dimensional analysis methods are used to compare impeller performance that relate power input to properties of the impeller, N and D . Power number, also known as Newton number, is related to the drag coefficient of a specific impeller shape rotating at a fixed stir speed (Paul et al., 2004). From a fluid mechanics prospective, it is analogous to the drag coefficient representing the sum of pressure and viscous forces. The dimensionless power number is expressed as follows:

$$N_p = \frac{P}{\rho N^3 D^5} \quad (2.2)$$

where N_p is the power number (-) and P is the power delivered to the fluid (W). The value of the power number varies depending on stirred tank reactor geometry, impeller geometry, liquid volume, impeller location, and flow regime. Power number can be determined by experimentally measuring torque on the impeller shaft. Typical literature investigations vary Reynolds number and measure impeller torque to generate a power number curve as a function of Reynolds number. Reynolds number is typically varied by changing the viscosity of the working fluid in the stirred tank reactor and/or changing the impeller speed while keeping other variables constant. The power number evaluated through impeller torque measurements is given by the following expression:

$$N_{p,M} = \frac{2\pi NM}{\rho N^3 D^5} \quad (2.3)$$

where $N_{p,M}$ is the power number determined by evaluating torque on the impeller shaft (-) and M is the torque (N m). In this equation, the numerator contains the power delivered to the fluid $2\pi NM$ (W) through torque. From a CFD perspective, this expression for power can be represented as the total turbulent kinetic energy dissipation rate in the whole reactor vessel. Measurements of impeller torque offer relatively simple experimental methodology for characterizing the energy balance on a global scale and is an important parameter for CFD model validation.

Other methods attempt to characterize fluid dynamics locally such as Laser Doppler anemometry (LDA), planar laser-induced fluorescence (PLIF), and particle image velocimetry (PIV). These systems are non-invasive techniques that can be used to characterize flow fields within a mixing device. These methods measure local velocity profiles. Typical non-invasive laser measurements focus on the region close to the impeller blades. Attempts have been made to estimate the energy dissipation close to the rotating impeller blade tip by correlating velocity gradients. For example, Chapple et al. (2002) used LDA to measure local velocity profiles at the tip of a Rushton turbine and a pitched blade impeller and compared the data to CFD predictions velocity profiles directly. Comparisons of experimental velocity profiles with CFD predictions is a common method for model validation in recent literature. Blais et al. (2016) suggests that comparing with velocity profiles provides qualitative verification, whereas power curves give more quantitative comparisons. In this thesis, CFD predictions are validated against literature examples where power number estimates are available from either simulation studies or experimental measurements. Additionally, one validation case is used to compare local LDA velocity profiles in a pitched blade impeller of Chapple et al. (2002) to CFD predicted velocity profiles.

2.3. Chemical Methods to Analyze Mixing

Chemical methods provide an indirect measurement of micromixing performance for both flow and batch systems. They rely on the selectivity of competitive-parallel or competitive-consecutive reactions, which can be correlated with the micromixing efficiency (Bourne, 2003). This section provides a summary of different chemical methods that have been implemented to characterize mixing performance in various systems. Popular methods include competitive-parallel reactions of the hydrolysis of 2,2-dimethoxypropane and neutralisation of sodium hydroxide proposed by Baldyga et al. (1998), the neutralization and hydrolysis of ethyl chloroacetate of Bourne and Yu (1994), and the iodide-iodate reactions, also known as Villermaux-Dushman reactions, developed by Fournier et al. (1996), Guichardon and Falk (2000), and Guichardon and Falk (2011). Although micromixing has a drastic impact on the conversion of chemical reactions, blend time or bulk mixing time also impacts reaction conversion because the reagents must come into

contact before mixing at a molecular level. Blend time is often measured by injection of a conductive tracer and monitoring the conductivity. It is often taken as the time to reach/dissipate to 95% of its steady-state concentration value. As noted by Fitschen et al. (2021), this method becomes challenging due to the mixing time being sensitive to the position of the probes and the position of the feeding. Therefore, Fitschen et al. (2021) developed a novel method to track the history of mixing using image processing. The imaging method can identify stagnant zones of poor mixing that is not possible using the tracer method. Blend time predictions in this work are evaluated by monitoring the global coefficient of variation (COV) and are presented in Chapter 6 in an EasyMax402 reactor. The results are compared with correlation data of Grenville (1992), but the focus of this work is on the micromixing occurring at the smallest length scales.

Chemical reactions having mixing-sensitive product yields are used to characterize mixing efficiency at the molecular scale (i.e., micromixing). When two competing reactions differ in reaction rate, the yield of the slow reaction will be (1) almost zero if mixing is perfect (system is said to be controlled by reaction kinetics), or (2) comparable with the yield of the faster reaction if mixing cannot be completed before significant reaction has already occurred (system is limited by mixing or mass transfer).

Generally, all reaction schemes that have been implemented for assessing micromixing performance rely on the coupling of a fast reaction, which is considered instantaneous relative to the mixing time, with a slower reaction, which has a time scale on the same order of magnitude as the mixing process. When mixing is faster than the slower reaction, mixing on the molecular scale is complete before the slower reaction can begin. This results in low conversion of the slow reaction. On the other hand, when mixing is slow relative to the slower reaction, there is a non-uniform distribution of reagents and conversion of the slower reaction begins to increase. To obtain a quantitative analysis of the mixing process, the reaction kinetics of the slower reaction need to be accurately known, and the amount to reaction product should be easily and accurately measurable.

Baldyga et al. (1998) proposed the test reaction that consists of the hydrolysis of 2,2-dimethoxypropane (DMP) and neutralisation of sodium hydroxide (NaOH) where reaction (I) and (II) compete for hydrochloric acid (HCl):



where component A represents HCl, component B is NaOH, and component D being DMP. Reactions (2.I) and (2.II) are described by second-order rate laws. This scheme is commonly known as the fourth Bourne reaction, where the slower reaction is catalytic with respect to component A (i.e., the acid). Baldyga et al. (1998) originally applied this reaction scheme in a stirred tank reactor operating with a Rushton turbine, but it has more recently been implemented in continuous flow systems likely due to the energy dissipation difference. Johnson and Prud'homme (2003) performed experiments in various confined impinging jet reactors (CIJR) and measured the conversion of component D to investigate mixing quality at different characteristic reaction and mixing times. Liu and Fox (2006) extended the work of Johnson and Prud'homme by simulating the CIJR to predict yield of the slower reaction. The rate constant of the slower reaction is given by the following equation:

$$k_2 = 7.32 \times 10^7 e^{(-5556/T)} 10^{(0.05434 + 7.07 \times 10^{-5} C_S)} \quad (2.4)$$

where T is the temperature (K), and component C_S represents sodium chloride concentration. At 298 K and a fixed sodium chloride concentration of 90 mol/m³, this results in a rate constant of the slower reaction given by $k_2 = 0.67313$ mol/m³/s. The characteristic reaction time t_r is defined as $t_r = 1/(k_2 C_{A0})$, where C_{A0} was taken as the average concentration of component A after mixing if no reaction takes place. Components A, B, and D follow a molar ratio of 1:1.05:1, respectively. In this work, this reaction was avoided due to the recent trend in its use in continuous flow geometries where the energy dissipation is typically orders of magnitude larger than in stirred tank reactors. Paul et al. (2004) recommends this scheme for higher energy dissipation rates.

A second reaction scheme proposed by Yu and Bourne (1994) is shown in Reactions (2.III) and (2.IV). In this scheme, the hydrolysis of ethyl monochloroethanoate ($\text{CH}_2\text{ClCOOC}_2\text{H}_5$) and neutralization of HCl reactions compete for limiting NaOH:



where component A represents NaOH, component B is HCl, component D is ethylchloroacetate, and component P₂ represents product ethanol. Reactions (2.III) and (2.VI) are described by second-order rate laws. This scheme is commonly known as the third Bourne reaction, where the primary difference from Reactions (2.I) and (2.II) is that the slower reaction is not catalytic with respect to component A. Yu and Bourne (1994) first implemented this reaction scheme in a stirred tank reactor, and it has since been adopted in other investigations using stirred tank reactors by Rozen (1995), Vicum et al. (2004), Baldyga et al. (2005), and Akiti and Armenante (2004). The reaction rate constant of the slower reaction k_2 is 0.023 mol/m³/s at 20 °C using typical reagent concentrations. Johnson and Prud'homme (2003) comment on some observed limitations in this reaction scheme, noting that ethylchloroacetate was degraded by acid leading to 4.5% reduction to this reagent in 30 minutes. For this reason, the scheme was avoided due to experiments requiring an initial stirred mixture of ethylchloroacetate and HCl before NaOH dosing. Additionally, experiments aimed at investigating micromixing require very long feed addition times that are often greater than 30 minutes, which would likely lead to non-mixing related induced production of by product P₂. Reactants and products can be experimentally measured using HPLC or GC.

Fournier et al. (1996) proposed the iodide-iodate reaction scheme that was later updated by Guichardon and Falk (2000) and Commenge and Falk (2011). The iodide-iodate reactions consist of a neutralization reaction and a redox reaction in competition for hydrogen ions:



where component A is the (limiting) hydrogen ions H⁺, component B represents borate ions B(OH)₄⁻, component D are iodide ions I⁻ (excess), component E is iodate ions IO₃⁻

(limiting), component P₂ represents iodine I₂. Formation of iodine I₂ (P₂) is used as a measure of micromixing performance. The rate of the slower reaction is expressed using fifth order kinetics:

$$R_2 = k_2(C_A)^2(C_D)^2(C_E) \quad (2.5)$$

where R_2 is the rate of reaction (mol/L/s), k_2 is the reaction rate constant (L⁴/mol⁴/s), C_A is the concentration of component A hydrogen ions H⁺ (mol/L), C_D is the concentration of component D iodide ions I⁻ (mol/L), C_E is the concentration of component E iodate ions IO₃⁻ (mol/L). The reaction rate constant k_2 is a function of ionic strength. Some discrepancies in the reaction rate constant k_2 of the slower reaction have been noted in literature (Arian & Pauer, 2021b; Baqueiro et al., 2018b; Bourne, 2008; Kölbl & Schmidt-Lehr, 2010b; Manzano Martínez et al., 2020). Iodine I₂ (P₂) reacts with iodide ions I⁻ (D) to form triiodide ions I₃⁻ according to the quasi-instantaneous equilibrium reaction:



where component P₃ represents triiodide ions I₃⁻. The equilibrium constant for reaction (2.VII) is taken to be 736 L/mol at 298 K. The equilibrium reaction allows for the evaluation of iodine I₂ (P₂) by measuring triiodide ions I₃⁻ (P₃) by UV-VIS spectrophotometry at a wavelength of 353 nm. More detail is given in Chapter 3. The fifth order reaction kinetics makes this scheme more challenging to implement (Habchi et al., 2014). Habchi et al. (2014) gives guidance for iteratively adjusting reagent concentrations to the turbulence level.

The iodide-iodate (Fournier et al., 1996; Guichardon & Falk, 2000) and third Bourne reactions (Bourne & Yu, 1994) have been extensively used to characterize micromixing performance in stirred tanks. Each reaction scheme presents unique challenges; however, in this work, the iodide-iodate test system was chosen for the experiments due to the ability to easily measure by-product triiodide (I₃⁻) concentration using a UV-VIS spectrophotometer. Furthermore, other studies have reported acid catalyzed decomposition of ethylchloroacetate in the third Bourne reaction (Johnson & Prud'homme, 2003), which would negatively impact the accuracy of the results when using this reaction.

When using the iodide-iodate test system, Schikarski et al. (2019) comment on the difficulty obtaining a continuous plot of selectivity varying with Re due to the concentrations measurements being limited to the detector range. Bourne (2003) has reported that, although the iodide-iodate reaction scheme gives good qualitative results, the results may not be quantitative and difficult to extrapolate between flow systems due to the complex kinetics. Quantitative results require that the kinetics of the reactions, especially for the slower reaction, be fully characterized under a given mixing condition. Only recently have the kinetics of the Villermaux-Dushman reactions been under active investigation by multiple independent research groups through the late 2010s to 2022 (Arian & Pauer, 2021a; Baqueiro et al., 2018a; Kölbl & Schmidt-Lehr, 2010a; Kotowicz & Jasińska, 2021; Manzano Martínez et al., 2020; Wenzel et al., 2018). Bourne suggests the differences in the model predictions could be due to lack of modern analytical techniques, variation in reactant concentrations, ionic strengths, buffers, and/or anions used by various research groups. The original kinetics of Guichardon et al. (2000) are used in this work due to its extensive use in micromixing models, but it is recognized that a comprehensive kinetic model of these reactions covering the full range of conditions may not yet be available.

2.4. Modelling fluid dynamics

Computational investigations of power number typically evaluate torque by integrating the pressure along the rotating impeller and shaft. This integration results in a force that is multiplied by a radial distance to obtain the moment, also known as torque. This parameter is often used for monitoring computational mesh dependence, where grid independence is typically said to be converged when power number stops changing with respect to number of computational cells (Coroneo et al., 2011; Duan et al., 2018). Coroneo et al. (2011) performed CFD simulations in a standard stirred tank operating with a Rushton turbine and evaluated power number based on the total turbulent kinetic energy dissipation rate. The power is expressed by Eq. (2.2), where the numerator is the total turbulent energy dissipated. Coroneo et al. (2011) compared power number based on torque with power number based on turbulent kinetic energy dissipation rate. In accordance with Paul et al. (2004), the authors observe that torque-based power numbers are in good agreement with

experimental values and energy dissipation rate based power number generally underpredicts the experimental measurements. It is generally well recognized that the power predictions based on energy dissipation rate require much higher mesh resolution than those based on torque. In fact, the difference between the torque-based and energy dissipation rate based power predictions is often used as a measure of the quality of the computational mesh. For example, Coroneo et al. (2011) used energy dissipation rate power number predictions to determine mesh convergence.

The quality of the fluid dynamics predictions depends not only on the quality of the mesh, but also on other model assumptions, most critically on the chosen turbulence model. Joshi and colleagues provide a series of excellent comprehensive reviews on turbulence models for stirred tanks for a number of different impeller types. It is generally well known that large-eddy simulation (LES) turbulence models are better suited for stirred tank reactors due to the non-isotropic handling of turbulent flows. However, these models have a significantly higher computational cost than Reynolds-averaged Navier-Stokes (RANS) models. Therefore, RANS approaches such as $k-\varepsilon$ and RSM, which give reasonable estimates of fluid dynamics in stirred tank reactors operating at high Reynolds numbers, remain widely used for process engineering analysis of chemical reactions or precipitation processes (Cheng et al., 2017). Other turbulence models that can be applied to stirred tank reactors exist, including direct numerical simulation (DNS). However, due to the high computational cost of these methods, their use in an industrial and engineering setting is limited by resources. More recently, Lattice Boltzmann Large Eddy Simulations are being explored as an alternative to finite volume methods due to its improved simulation time (Haringa, 2022; Kuschel et al., 2021).

Duan et al. (2019) followed the approach of Coroneo et al. (2011) of computing both dissipation-based and torque-based power numbers to use as a measure of mesh independence. The length scales range between 1.4×10^{-3} m (300 000 cells) and 0.83×10^{-3} m (1 400 000 cells). With each grid, Duan et al. (2019) also compared velocity and turbulent kinetic energy profile predictions at the impeller tip and determined that all three variables stop changing appreciably at a length scale of 1.0×10^{-3} m (1 090 000 cells). In the same investigation of Duan et al. (2019) compared predictions made using a standard

k - ε turbulence model, RNG turbulence model, Reynolds stress model (RSM), and SST k - ω turbulence model for an unbaffled stirred tank reactor operating at $Re = 960$ using a Rushton turbine. Duan et al. (2019) reported RSM gives the best agreement with experimental data based on local velocity profiles at low Reynolds numbers. Each turbulence approach performs very similar when considering local profiles of flow and turbulence variables. Overall, the standard k - ε is an acceptable turbulence model given other sources of error not accounted for such as mesh resolution and non-isotropic turbulence. This thesis adopts the standard k - ε turbulence model due to its applicability to industry and frequent use in literature investigations of stirred tank reactors.

2.5. Modelling Micromixing

Many simplified models have been proposed to correlate and predict reactive mixing experiments. The engulfment model (E-model) proposed by Bourne and Baldyga (1989) is a simple set of ordinary differential equations that are used to estimate reaction yield in mixing-limited systems. The E-model originates from the engulfment-deformation-diffusion model (EDD model) of Bourne and Baldyga (1990). The E-model assumes that the mixing process is controlled by the viscous-convective region, which Bourne and Baldyga termed engulfment, at length scales at or below the Kolmogorov scale. The E-model is derived based on the assumption that very small volumes of concentrated A are added to a large excess volume of second reactant B (i.e., $V_{A0} \ll V_{B0}$). In this way, Bourne and Baldyga take the reaction zone as the region where A is in excess. The simplest formulation of the E-model is expressed as mass transfer by micromixing (engulfment) of local surroundings B into a growing reacting volume of A. This reaction zone grows according to the following expression:

$$\frac{dV_e}{dt} = EV_e \quad (2.6)$$

where V_e is the volume of the reaction zone (m^3), E is the engulfment rate coefficient and applies to the viscous-convective sub-region of the concentration spectrum, and the product EV_e is the rate that surrounding reactants are incorporated into the reaction zone. Initially, the volume of reaction zone refers to the region where component A is present so that

$V_e(t = 0) = V_{A0}$ where $V_{A0} = 0$. A mass balance on component i in the growing reaction zone gives the following equation:

$$\frac{d(V_e C_i)}{dt} = E V_e C_{i,\infty} + R_i V_e \quad (2.7)$$

where $C_{i,\infty}$ is the concentration of component i in the local environment of the growing eddy, $E V_e C_{i,\infty}$ is the rate at which component i is added to the growing volume by engulfment, and $R_i V_e$ is the production rate of component i in the reaction zone. Concentration C_i of component i is constant and uniform within the growing volume due to the assumption that diffusion is very fast relative to engulfment. Applying the product rule to Eq. (2.7) and combining with Eq. (2.8) after rearranging gives the following expression:

$$\frac{dC_i}{dt} = E(C_{i,\infty} - C_i) + R_i \quad (2.8)$$

where C_i is taken as a uniform concentration inside the growing reaction zone (mol/m^3). The engulfment rate coefficient considers dissipation and viscosity and is given according to the following expression:

$$E = 0.058 \left(\frac{\varepsilon}{\nu} \right)^{1/2} \quad (2.9)$$

and the characteristic time describing micromixing is inversely proportional to $1/E$ under isotropic turbulence conditions. The E-model is a result of assuming slow engulfment relative to diffusion in the reaction-diffusion equation (Bourne & Baldyga, 1990). It is important to note that in Eq. (2.9) the interaction term between fluid environments is modelled by the first term on the RHS as $E(C_{i,\infty} - C_i)$.

Baldyga et al. (1997) modified the E-model to include the impact of self-engulfment. The self-engulfment term is added to the end of the original model formulation and can be thought of as an efficiency term to account for equal volume mixing:

$$\frac{dV}{dt} = EV \left(1 - \frac{V e^{-t/\tau_s}}{V_0} \right) \quad (2.10)$$

$$\frac{dC_i}{dt} = E(C_{i,\infty} - C_i) \left(1 - \frac{V e^{-t/\tau_s}}{V_0} \right) + R_i \quad (2.11)$$

where the efficiency term representing self-engulfment is given as $(1 - V\exp(-t/\tau_s)/V_0)$. The interaction term is still modelled as a concentration difference driving force. Schwarzer and Peukert (2004) expanded the model of Baldyga et al. (1997) by adding compartments that act as extra environments that are allowed to interact based on mixing rules. The extended EDD model proposed by Schwarzer and Peukert (2004) improve the original work of Baldyga et al. (1997) by considering equal volume mixing.

The interaction-by-exchange-with-the-mean (IEM) model was introduced by Villiermaux and Devillon (1972) and Costa and Trevissoi (1972). The IEM model relates the mass exchange rate to a concentration difference. In its original formulation, fluid engulfment does not depend on viscosity. Villiermaux and Falk (1994) and Fournier et al. (1996) extended the IEM model to include engulfment parameters, making it similar to the E-model. This modified model is commonly known as the incorporation model and was derived based on the earlier work. In this model, a limiting reactant (aggregates) is added to a large excess of surrounding reactant fluid. The surrounding environment interacts with the limiting reactant and a concentration difference drives mass transfer from the surroundings to reactant aggregates. The characteristic time for incorporation is assumed equal to the micromixing time t_m . Aggregates are assumed to grow exponentially according to one of the following expressions:

$$g(t) = e^{(t/t_m)} \text{ or } g(t) = 1 + \frac{t}{t_m} \quad (2.12)$$

The second term for the exponentially growing environment $g(t)$ results from a Taylor expansion of the first term when the ratio t/t_m is small. The concentrations of each component j are described by the following set of differential equations:

$$\frac{dC_j}{dt} = (C_{j10} - C_j) \frac{1}{g} \frac{d(g)}{dt} + R_j \quad (2.13)$$

where C_{j10} represents the surrounding environment (mol/L), C_j is the concentration of component j (mol/L), R_j is the reaction rate expression for component j and is a function of the kinetics involved. For $g(t) = \exp(t/t_m)$ the species balance equation result in the following expression:

$$\frac{dC_j}{dt} = (C_{j10} - C_j) \frac{1}{t_m} + R_j \quad (2.14)$$

where the interaction term is represented by $(C_{j10} - C_j)/t_m$. It is important to note the similarities in Eq. (2.15) and Eq. (2.9) for the IEM model and E-model, respectively. These models show similar mathematical forms with the difference being in their respective time constant parameters. Bourne and Baldyga (1999) suggest differences in model predictions is not due to parameters alone, but model predictions are also strongly influenced by the treatment of the reaction zone. The E-model treats the reaction zone as a localized growing volume with time where excess A is present, while the IEM-model considers a fixed size reactor volume that covers the whole domain.

Both the incorporation model and the E-model have been extensively used in the literature for characterizing mixing performance and the trends are generally similar. They can both be used to analyze the order of magnitude, or scale, of the micromixing time for a given flow system. For example, Yang et al. (2005) studied micromixing performance of a rotating packed bed reactor where iodide-iodate reaction conversions were obtained experimentally, and the results were analyzed using the incorporation model by plotting reaction conversion (segregation index X_S) as a function of micromixing time. Yang et al. (2005) assumed a constant concentration of C_{A0} shown in Eq. (2.5) which may lead to overestimates in R_2 . In this way, the segregation index vs micromixing time plot is used as a so called ‘calibration’ curve that assigns a mixing time to a segregation index. These mixing models are commonly used in current literature and have not significantly deviated from their original formulation in the early 1990s. More recent investigations include a comprehensive look at the incorporation model for analyzing micromixing times from Arian and Pauer (2021). John van der Schaaf and colleges have used this approach extensively in a rotor-stator spinning disk (Manzano Martínez et al., 2020)

In the present study, the E-model of Bourne and Baldyga (1990) was used for comparison to CFD modelling because its mathematical description is naturally linked to turbulent parameters through the E parameter.

2.6. Integration into CFD

Several sub-grid scale mixing (i.e., gradients that exist below the scale of the smallest computational cell) approaches have been employed in CFD codes to describe reactions

where mixing on the molecular scale becomes important (Öncül et al., 2009). Fox (2003) provides a detailed summary of reactive mixing models specific to CFD. Bourne and Baldyga (1999) review turbulent reacting flow models using reduced order methods as well as a computational framework. This section only provides a brief background of information related to the coupling of a micromixing model to CFD simulations of flow fields. The section starts with a discussion of the direct-quadrature-method-of-moments (DQMOM) employed to solve the composition probability density function (PDF) that makes it possible to calculate sub-grid scale mixing effects based on fluid environment approaches. The remainder of this section discusses other techniques that have been used to analyze mixing within CFD. Table 2.1 provides a summary of common micromixing models implemented to simulate turbulent reacting flows within the past two decades. Turbulence models and modifications to sub-grid scale source term parameters are outlined in Table 2.1. The table is not intended to be comprehensive, but it is intended to provide a sense of commonly used approaches found in literature. Perhaps the most common approaches employed in CFD to simulate competitive-parallel reactions in stirred tank reactors are the DQMOM-IEM (Liu & Fox, 2006) and the multiple-time-scale turbulent mixer model (Vicum et al., 2004). Both models significantly depend on turbulence variables, including turbulent kinetic energy and the dissipation rate of turbulent kinetic energy.

Table 2.1: Summary of the reactive mixing models and turbulence models in recent CFD studies.

Reference	Model	Geometry
Marchisio and Barresi (2003)	Turbulence: RANS $k-\varepsilon$ Micromixing Model: DQMOM-IEM(3) C_φ : 0.25–4.0 Source terms: Villermaux-Dushman reaction	Taylor-Couette reactor
Wang and Fox (2004)	Turbulence: RANS $k-\varepsilon$ Micromixing Model: DQMOM-IEM(2) C_φ : 2.0 Source terms: reactive-precipitation with nucleation and growth kinetics	Plug-flow reactor
Woo et al. (2006)	Turbulence: RANS $k-\varepsilon$ Micromixing Model: DQMOM-IEM(3) C_φ : 2.0 Source terms: reactive-precipitation with nucleation and growth kinetics	Stirred Tank Reactor
Liu and Fox (2006)	Turbulence: RANS $k-\varepsilon$ Micromixing Model: DQMOM-IEM(2) C_φ : function of local Reynolds number Source terms: fourth Bourne reaction	Confined impinging-jets reactor
Vicum et al. (2004)	Turbulence: RANS $k-\varepsilon$ Micromixing Model: Multiple-time-scale turbulent mixer model and E-model C_φ : inertial-convective, engulfment and diffusion time constants Source terms: N/A	Stirred tank reactor
Gavi et al. (2007)	Turbulence: RANS $k-\varepsilon$, LES with Smagorinsky (1963) SGS model Micromixing Model: DQMOM-IEM(2) C_φ : function of local Reynolds number Source terms: fourth Bourne reaction	Confined impinging-jets reactor
Marchisio (2009)	Turbulence: LES with Smagorinsky (1963) SGS model Micromixing Model: DQMOM-IEM(2) C_φ : function of local Reynolds number and varied 0.5–4.0 Source terms: fourth Bourne reaction	Confined impinging-jets reactor
Cheng et al. (2016)	Turbulence: RANS: $k-\varepsilon$ and anisotropic two-phase explicit algebraic stress model	Stirred tank reactor

Reference	Model	Geometry
	Micromixing Model: FM-PDF C_φ : 0.5 Source terms: reactive-precipitation with nucleation and growth kinetics	
Duan et al. (2018)	Turbulence: RANS: k - ϵ	Stirred Tank Reactor
Duan et al. (2019)	Micromixing Model: DQMOM-IEM(2) C_φ : function of local Reynolds number and varied 0–2.0 Sc_t : varied 0.1–0.8 Source terms: fourth Bourne reaction (Duan et al., 2018) and competitive-consecutive reactions (Duan et al., 2019)	
Duan et al. (2016)	Turbulence: RANS: k - ϵ	Stirred Tank Reactor
Duan et al. (2020)	Micromixing Model: mixture fraction and its variance coupled with E-model C_φ : function of local Reynolds number Source terms: N/A	

*All investigations use $Sc_t = 0.7$ unless otherwise noted.

The research by Fox and colleagues developed and validated a direct-quadrature-method-of-moments (DQMOM) coupled to an IEM model for evaluating local reaction rates and large and small scale mixing times (J. C. Cheng & Fox, 2010; Liu & Fox, 2006; Wang & Fox, 2004). A derivation of the model is provided in Appendix B of Fox (2003) and later expanded by Marchisio and Fox (2005). Tang et al. (2007) give a detailed description on the transported PDF methods. Haworth (2010) evaluated different PDF approaches in a comprehensive comparison review. In the multi-environment method, the joint composition PDF transport equation is approximated to have a shape represented by a set of single point delta functions (environments) with variable probability. Multi-environment micromixing models discretize composition space into a set of environments (or probability modes) that interact and exchange mass at an exchange rate through micromixing. Common approaches consider two environments; however, other numbers of environments have been employed as well (Öncül et al., 2009). Studies evaluating reactive crystallization often use a three-environment approach, represented as DQMOM-IEM (3) in Table 2.1, where initially liquids are segregated into two environments, a third environment is generated when the two environments come into contact. The fluid environments are represented as a mass or volume fraction that can be converted into

species concentrations. The purpose of implementing a multi-environment mixing model is to consider sub-grid scale effects in each computational cell for the system by applying source terms to the transport equations. The source terms add an unknown mixing rate constant that is intended to represent the unresolved boundary layer scales. The molecular diffusion term in the joint composition PDF transport equation is closed by the IEM model. In this multi-environment PDF approach, a full PDF method is recovered when the number of environments goes to infinity. Previous literature has demonstrated that two environments are enough for accurate estimates of sub-grid scale mixing (Öncül et al., 2009).

The composition PDF transport equation for incompressible flow involving reactive scalars is described by the following equation:

$$\frac{\partial f}{\partial t} + \nabla \cdot (\bar{\mathbf{U}}f) + \frac{\partial}{\partial x_i} (\langle (u_i | \psi) \rangle f) = - \frac{\partial}{\partial x_i} (\langle (\Gamma_i \nabla^2 \phi'_i | \psi) \rangle f) - \frac{\partial}{\partial x_i} (\Gamma_i \nabla^2 \phi_i f + S_i(\phi) f) \quad (2.15)$$

For isotropic turbulence, $\nabla^2 \phi_i$ is zero. The transported PDF requires a closure model for the molecular diffusion term. The chemical source term S_i is closed directly using mass balances of reactants. The IEM model is a linear driving force of the difference in scalars represented by the following expression:

$$\langle (\Gamma_i \nabla^2 \phi'_i | \psi) \rangle = \frac{1}{2} \frac{\varepsilon_\alpha}{\langle \phi_i'^2 \rangle} (\langle \phi_\alpha \rangle - \psi_\alpha) = \frac{1}{2} \frac{C_\phi \varepsilon}{k} (\langle \phi_\alpha \rangle - \psi_\alpha) \quad (2.16)$$

The IEM approximation is a popular closure model due to its simplicity and computational efficiency. The method introduced by Liu and Fox (2006) has been extended to stirred tank reactors by Duan et al. (2018) to estimate mixing effects on competitive-parallel reactions. Model results were compared to experiments conducted by Baldyga and Makowski (2001). In a follow-up investigation, Duan et al. (2019) applied the model to larger scales with the goal of improving wastewater treatment process efficiencies through better understanding of the reactive mixing process. Other closures have also been implemented. For example, Madadi-Kandjani et al. (2017) considered a Fokker-Planck closure for molecular diffusion to model competitive-consecutive reactions with an extended QMOM to approximate the composition PDF that showed good results.

Baldyga et al. (2001) studied the effects of mixing on competitive-parallel reactions in a stirred tank reactor. Turbulent flow fields were obtained using a standard k - ε model. The flow fields were then analyzed with what Baldyga et al. (2001) refers to as the multiple-time-scale turbulent mixer model. In this model, the variance of mixture fraction is composed of three terms that account for different time scales of turbulence and mixing. The mixture fraction variance is expressed as follows:

$$a_3 = (a_1 - \bar{a})^2 = a_{2,1} + a_{2,2} + a_{2,3} \quad (2.17)$$

where a_3 represents deviations of the mixture fraction from the mean value, a_1 is the mixture fraction, \bar{a} is the mean mixture fraction, a_2 is the mixture fraction variance, $a_{2,1}$ is the inertial-convective subrange, $a_{2,2}$ is the viscous-convective subrange, and $a_{2,3}$ is the viscous-diffusive subrange. The partitions applied to a_2 attempt to represent the decay of concentration variance for meso-mixing (inertial-convective subrange) and micromixing or Engulfment through the viscous-diffusive subrange. The mixture fraction variance components are related to the source terms for the production and dissipation of large and small-scale segregation:

$$\frac{\partial a_{2,1}}{\partial t} + \nabla \cdot (\bar{\mathbf{U}} a_{2,1}) = \nabla \cdot (D_T \nabla a_{2,1}) + \nabla \cdot \left(\frac{v_t}{Sc_t} \nabla a_{2,1} \right) + 2D_T |\nabla a_1|^2 - \frac{1}{\tau_s} a_{2,1} \quad (2.18)$$

$$\frac{\partial a_{2,2}}{\partial t} + \nabla \cdot (\bar{\mathbf{U}} a_{2,2}) = \nabla \cdot (D_T \nabla a_{2,2}) + \nabla \cdot \left(\frac{v_t}{Sc_t} \nabla a_{2,2} \right) + \frac{1}{\tau_s} a_{2,1} - E a_{2,2} \quad (2.19)$$

$$\frac{\partial a_{2,3}}{\partial t} + \nabla \cdot (\bar{\mathbf{U}} a_{2,3}) = \nabla \cdot (D_T \nabla a_{2,3}) + \nabla \cdot \left(\frac{v_t}{Sc_t} \nabla a_{2,3} \right) + E a_{2,2} - \frac{1}{\tau_G} a_{2,3} \quad (2.20)$$

where τ_s is the characteristic meso-mixing time in the inertial-convective subrange and is expressed as follows:

$$\frac{1}{\tau_s} = 2 \left(\frac{\varepsilon}{k} \right) \quad (2.21)$$

E is the engulfment rate given as Eq. (2.10) and the characteristic time for mixing at the Batchelor scale τ_G occurs by deformation and molecular diffusion. Baldyga et al. (2001) describes this as a function of the Schmidt number (Sc):

$$\tau_G = \frac{1}{E} \left(0.303 + \frac{17050}{Sc} \right)^{-1} \quad (2.22)$$

It is important to note the source terms for micromixing in Eq. (2.18)–(2.20). The dissipation term in $a_{2,1}$ is equal to the production term in $a_{2,1}$, the dissipation term in $a_{2,2}$ is equal to the production term in $a_{2,3}$ until the final length scale is reached. Gradients in mixture fraction produce variance until it is totally dissipated. The model has been adopted in other works including Vicum et al. (2004) and Vicum and Mazzotti (2007). Lindenberg et al. (2008) use this model to determine mixing times and to visualize mixing and reaction zones in two continuous flow mixers. Lindenberg et al. (2008) use variance cut-off of 0.001. Mixing times are based on the residence time in the complete mixing zone.

Duan et al. (2016) coupled the E-model with self-engulfment to CFD to investigate micromixing performance in the stirred tank reactors of Assirelli et al. (2002) and Akiti and Armenante (2004). The experiments implemented the third Bourne reaction and iodide-iodate schemes and assessed micromixing performance by measuring conversion of the slower reactions. Duan et al. (2016) performed CFD simulations in the stirred tank reactors by solving the Reynolds-averaged transport equations for mean mixture fraction (a_1) and its variance (a_2) according to Liu and Fox (2006) and Gavi et al. (2007). The authors estimated averaged turbulence variables in the reactions zone according to a mixture fraction variance weighted mean of turbulent kinetic energy dissipation rate. Duan et al. (2016) then used these variables in the E-model to estimate conversion of the slower reaction. Duan et al. (2016) showed the impact of feeding location on the distribution of mixture fraction variance with a cut-off defined as $a_2/a_{2\max} \geq 0.001$. In a more recent investigation, Duan et al. (2020) performed the same analysis in a gas-liquid and solid-liquid stirred tank reactor following experiments of Hofinger et al. (2011).

Besten (2021) investigated micromixing performance in a rotor-stator spinning disc reactor using the iodide-iodate reaction scheme and analyzed micromixing times by coupling the multiple-time-scale turbulent mixer model to the E-model. Besten (2021) adopts a similar approach to that of Duan et al. (2016) where the turbulent energy dissipation rate in the mixing zone was determined by the weighted mixture-averaging mixture fraction variance $a_{2,2}$ because it is at the micromixing sub-scale.

The work in this thesis adopts the same modelling approach as Liu and Fox (2006) and Duan et al. (2018), where the competitive-parallel reactions are modelled using the two-environment DQMOM model coupled with an IEM model to close the molecular diffusion term in a CFD framework. Separately, following Duan et al. (2016), the E-model was implemented in MATLAB to aid interpretation of turbulent mixing model predictions and assess model sensitivity. This provides comparison of two modelling approaches with experimental data.

2.7. Summary

In this chapter, approaches for simulating fluid dynamics and competitive-parallel reactions were reviewed. These approaches include reduced-order modelling techniques such as the E-model and the IEM model. Additionally, more rigorous multidimensional approaches have been employed in a CFD framework, including the DQMOM-IEM model and the multiple-time-scale turbulent mixer model. Each approach has advantages and disadvantages. The reduced-order models are not suitable for non-uniform mixing rates due to the simplicity of the global averaged turbulence energy dissipation rate; however, they are much less computationally demanding, and they require some effort to couple to CFD. CFD methods have shown good agreement with experiments when high Reynolds number flows are employed. Theoretical closure models cannot be developed based on mixing-length scale because mesh resolution would be too fine; therefore, empirical closure models are used to estimate local mixing rates. After the mixing is validated, it is relatively easy to implement nucleation and crystal growth rates into the DQMOM-IEM formulation because it simply requires changing the source terms and kinetic expression in the model.

In this study, a DQMOM-IEM approach is used to simulate competitive-parallel reactions because the source terms can be modified, and it is suitable to track local concentration and reaction rates. This method has been employed in stirred tank reactors and its extension to predict crystallization is relatively straightforward. The main weakness of this method is that the model relies on an empirical formulation for mixing rate, but this cannot be easily avoided without resolving the length scales of turbulent and molecular transport.

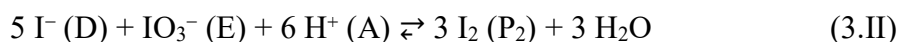
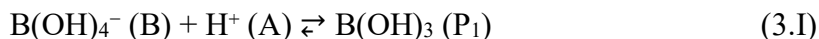
CHAPTER 3: METHODOLOGY

Chapter 2 provided a brief overview of common chemical methods for assessing micromixing performance. This chapter provides a summary of the experimental and numerical research methodology used to analyze micromixing in a small-scale stirred tank EasyMax 402 reactor. The experimental data is used for validation of the newly developed OpenFOAM solver in Chapter 6.

3.1. Experimental Methodology

3.1.1. Iodide-Iodate Reaction Background and Analysis

This work uses the Villiermaux-Dushman reactions proposed by Fournier et al. (1996) where iodide-iodate reaction and neutralization of boric acid compete for the limiting reagent sulfuric acid. The neutralization reaction (3.I) can be considered to be infinitely fast, and it is coupled with a finite-rate reaction (3.II):



where borate ions B(OH)_4^- (B) in reaction (3.I) and iodine ions, iodide I^- (D), and iodate IO_3^- (E), in reaction (3.II) compete for common hydrogen ions H^+ (A). In the experiments, mixing quality is assessed by dosing limiting reagent sulfuric acid H_2SO_4 into a mixture of borate ions B(OH)_4^- (B), excess iodide ions I^- (D), and iodate ions IO_3^- (E).

If mixing is near perfect, hydrogen ions H^+ (A) from injected sulfuric acid H_2SO_4 are completely consumed by reaction (3.I). If mixing quality is poor, hydrogen ions H^+ (A) are consumed in both reactions according to the mixing rate. The former results in a mixture containing negligible amounts of iodine I_2 (P_2), while the latter triggers formation of iodine I_2 (P_2). Therefore, the amount of iodine I_2 (P_2) produced is used as a qualitative measure of mixing performance.

The iodine I_2 (P_2) formed in reaction (3.II) can further react in a quasi-instantaneous reaction with iodide ions I^- (D) which forms an equilibrium with triiodide ions I_3^- (P_3):



The concentration of triiodide ions I_3^- (P_3) in this work was measured using a UV-6300PC Spectrophotometer (VWR) at a wavelength of 353 nm. A range of wavelengths for screening was not considered, but for each measurement the spectrum was visually monitored to ensure peak absorbance at 353 nm. The concentration of triiodide ions I_3^- (P_3) is quantified by applying the Beer-Lambert law, which linearly relates light absorbance to the triiodide ion concentration:

$$[I_3^-] = \frac{OD}{\epsilon_{353}l} \quad (3.1)$$

where OD denotes the optical density (absorbance), ϵ_{353} is the extinction coefficient of triiodide ions I_3^- (P_3) at a wavelength of 353 nm (m^2/mol), and l is the optical path length within the measurement cell (m). The linear relationship between absorbance and triiodide ion I_3^- (P_3) was verified by calibration (see Appendix A). The extinction coefficient of triiodide ions I_3^- (P_3) at a wavelength of 353 nm was found to be 2 387 m^2/mol . All experiments use quartz cells with a path length of $l = 0.010$ m.

To calculate the amount of iodine I_2 (P_2) formed, a mass balance of reaction (3.II) was coupled to the equilibrium constant of reaction (3.III):

$$[I^-] = [I^-]_0 - \frac{5}{3}([I_2] + [I_3^-]) - [I_3^-] \quad (3.2)$$

$$K_B = \frac{[I_3^-]}{[I_2][I^-]} \quad (3.3)$$

where K_B (L/mol) is the equilibrium constant of reaction (3.III). The dependence of K_B on temperature is given by the following expression (Palmer et al., 1984):

$$\log_{10}(K_B) = \frac{555}{T} + 7.355 - 2.575 \log_{10} T \quad (3.4)$$

where T is the temperature (K). The analysis in this work uses an equilibrium constant at 25 °C and results in $K_B = 736$ L/mol. After combining Eq. (3.2) and Eq. (3.3), the concentration of iodine I_2 (P_2) can be calculated explicitly from the following quadratic expression:

$$\frac{-5}{3}([I_2])^2 + \left([I^-]_0 - \frac{8}{3}[I_3^-]\right)([I_2]) - \frac{[I_3^-]}{K_B} = 0 \quad (3.5)$$

The segregation index (X_S) is employed to quantify micromixing performance, as proposed by Fournier et al. (1996). From a mixing perspective, X_S represents the normalized selectivity towards the slower reaction (3.II):

$$X_S = \frac{Y}{Y_{ST}} \quad (3.6)$$

where Y is the yield of iodine I_2 (P_2) relative to the amount of hydrogen ions H^+ (A) available for 1:1 mixing:

$$Y = \frac{V_{tank}([I_2] + [I_3^-])}{0.5V_{inj}[H^+]_0} \quad (3.7)$$

where $[H^+]_0$ is the initial concentration of hydrogen ions (mol/L), $[I_2]$ is the concentration of iodine formed (mol/L) by reaction (3.II) and is evaluated using Eqs. (3.1)–(3.5) outlined. The formation of iodine I_2 is assumed to be caused by mixing effects only, and therefore pH must remain between 7 and 10. $[I_3^-]$ is the concentration of triiodide (mol/L) due to the equilibrium reaction (3.III) and measured experimentally. V_{tank} is the volume of the tank (m^3) and V_{inj} is the volume of injected sulfuric acid (m^3).

Y_{ST} is the maximum value for Y and is calculated when reactions (3.I) and (3.II) occur at the same time scale (i.e., if the system were completely mixing limited). Therefore, Y_{ST} is given by the following equation:

$$Y_{ST} = \frac{6[IO_3^-]_0}{6[IO_3^-]_0 + [B(OH)_4^-]_0} \quad (3.8)$$

where $[IO_3^-]_0$ is the initial concentration of iodide ions (mol/L) and $[B(OH)_4^-]_0$ is the initial concentration of borate ions (mol/L). Thus, the theoretical maximum value of X_S is 1 under infinitely slow mixing conditions and the theoretical minimum value is 0 under infinitely fast mixing conditions.

3.1.2. Experimental Setup and Procedure

Various concentrations of sulfuric acid solution were injected at locations near the impeller and at a subsurface location just below the free surface to characterize mixing at these key locations in the reactor. The main set of experiments used a three bladed 50 mm diameter retreat curve impeller. An additional limited number of experiments used a four blade 38

mm diameter pitched blade impeller to investigate the impact of impeller geometry on mixing performance.

Figure 3.1 provides a summary of the dimensions of the stirred tank reactor system investigated. The point shown in black indicates the main feeding location close to the impeller tip. The point shown in red indicates subsurface feeding where a limited number of experiments were performed at this feed location. The impeller was placed so that the top of the blade tip was in line with the 100 mL graduation mark on the vessel wall and results in an off-bottom clearance of 0.010 m ($C = 0.010$ m). This was done to ease day-to-day setup and maintain consistency between experiments. The acid was injected through a PTFE tube using a syringe pump. Impeller feeding was performed mid way between the blade tip and vessel wall to avoid the tube hitting the vessel walls. A visual illustration of the feed location is shown in Figure 3.2.

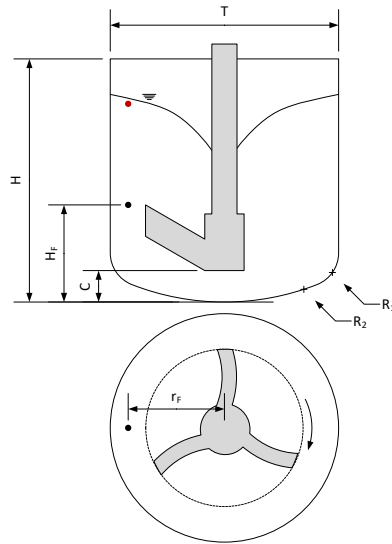


Figure 3.1: Reactor geometry with the 50 mm retreat curve impeller showing feeding locations close to the impeller (black dot) and just below the free surface (red dot).

Table 3.1: Dimensions of the stirred tank crystallization reactor used in this work.

Name and Symbol	Dimension (m)
Internal tank diameter, T	0.0726
Off-bottom clearance, C	0.010
Blade width, W_b	0.010
Tank radius, R_1	0.010
Tank radius, R_2	0.080
Radial feed position, r_F	0.0307
Axial feed position, H_F	0.028875

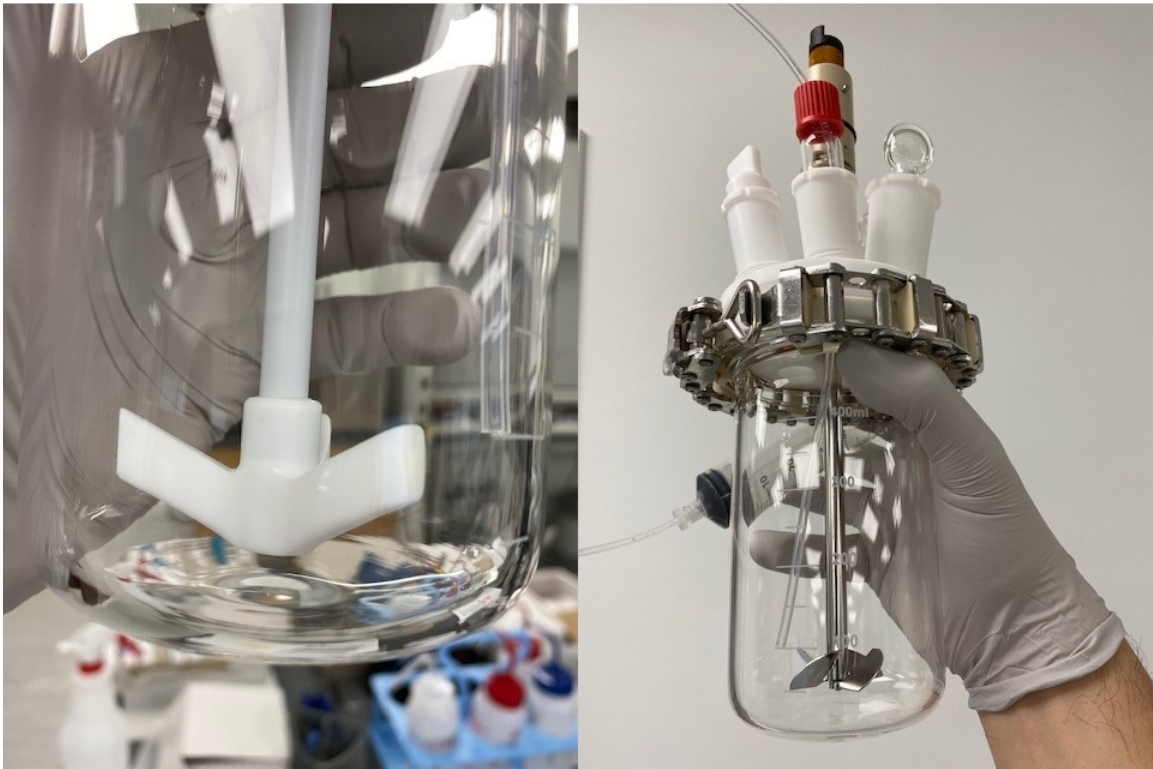


Figure 3.2: Images showing the feeding locations close to the impeller blade tip for both impeller types. The top of the blade tip and feed tube outlet is in line with the 100 mL graduation mark.

A schematic representation of the acid dosing system is shown in Figure 3.3. The EasyMax402 reactor is equipped with a PTFE cover plate and 6 ports of size $3 \times 1/2$ in, $2 \times 3/4$ in, and a single $3/8$ in port for the overhead stirrer. Two nested PTFE bushing adapters, $1/2$ in male $\times 1/4$ in female and $1/4$ in male $\times 1/8$ in female, were placed in the $1/2$ in port on the cover. A bored-through stainless steel compression fitting, for a $1/16$ in OD tube with a $1/4$ in NPT male thread, was screwed into the smaller PTFE bushing

adapter. The PTFE bushing adapter was used to protect the EasyMax lid from damage due to the stainless steel compression fitting. The compression fitting allowed for easy vertical adjustments to the feeding location. Hard plastic PTFE tubing with an outer diameter (OD) of 1/8 in (3.175 mm) and an internal diameter (ID) of 1/16 in (1.59 mm) was used for acid injection chosen because it should be rigid enough to avoid motion due to the motion of the fluid, and it is small enough to not significantly impact the surrounding flow field. It should be noted that stainless steel tubing with a smaller diameter was considered as an alternative to PTFE due to its rigidity, but PTFE was chosen over stainless due to the potential impact of corrosion that would compromise acid injection. PFA clear tubing with 1/16 in ID and 1/8 in OD, was used between the dosing tube and the syringe pump (Chemyx Fusion 100 Syringe pump). All piping equipment was purchased from McMaster-Carr (*McMaster-Carr*, n.d.). Part numbers are summarized in Figure 3.3.

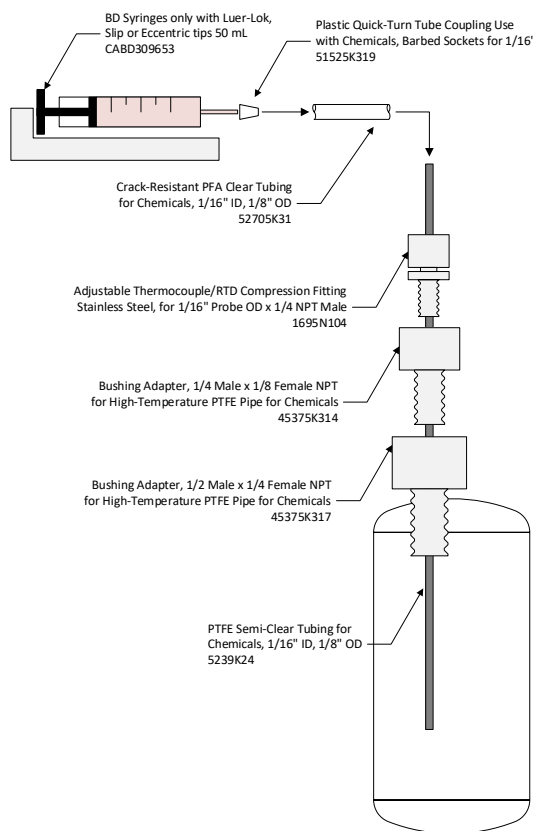


Figure 3.3: Schematic diagram of the dosing system for the EasyMax402 reactor with feed additions made through a PTFE 1/8 in OD (3.175 mm), 1/16 in ID (1.59 mm) tube positioned for dosing close to the impeller and just below the free surface.

The reactor vessel was filled with a buffer solution containing the reaction substrate boric acid ($B(OH)_3$) with sodium hydroxide (NaOH) to maintain a constant pH at around 9.14. Solutions of potassium iodide (KI) and potassium iodate (KIO_3^-) were then added to the buffer solution. All experiments used a volume of 300 mL before acid dosing. Sulfuric acid (H_2SO_4) was then slowly fed at the specified feed location. New solutions of each reagent were made before each experiment due to the sensitivity to light. Initial and final pH of the solution must be higher than ~ 7.1 to avoid thermodynamic induced formation of iodine (I_2). To ensure produced iodine (I_2) is due to mixing limitations only, pH measurements were taken before and after acid dosing experimental runs.

Table 3.2 outlines the concentrations of reagents used. These concentrations follow guidance from Fournier et al. (1996), Guichardon and Falk (2000), and Assirelli et al. (2002). The bulk buffer solution and iodine ion concentrations are fixed for all experiments. Sulfuric acid was the only concentration that was varied between concentration sets. This was done to ensure reaction times and mixing rates are varied independently. The difficulty in the Villiermaux-Dushman approach lies in the dependence of X_S on concentrations and running with fixed concentration sets it becomes challenging to stay within the calibration range of the detector.

Table 3.2: Summary of the concentrations used in the experiments.

Reactants	Set of Concentrations (mol/L)				
	Set 1 (C_1)	Set 2 (C_2)	Set 3 (C_3)	Set 4 (C_4)	Set 5 (C_5)
Boric acid $B(OH)_3$	0.1818	0.1818	0.1818	0.1818	0.1818
Sodium hydroxide NaOH Borate ions $[B(OH)_4]^-$	0.0909	0.0909	0.0909	0.0909	0.0909
Potassium iodide KI	0.0117	0.0117	0.0117	0.0117	0.0117
Potassium iodate KIO_3	0.0023	0.0023	0.0023	0.0023	0.0023
Sulfuric acid H_2SO_4	0.15	0.10	0.20	0.30	0.40

Note: Run 6 in Table 3.4 was performed using sulfuric acid concentration of 0.05 mol/L.

Table 3.3 provides a summary of the sampling procedure followed for each concentration set during acid dosing. Concentration set 1 (C_1) ran with an acid injection rate of 4 mL/min.

All other concentration sets ran with an acid injection rate of 2 mL/min. A total of 7 samples were drawn before, during, and after each experiment for UV analysis. Samples were taken before to ensure that the initial solution had negligible iodine ions present before the experiment was performed. A final sample was collected after all acid was added. Samples were collected during acid dosing to help maintain a constant volume during the experiments and to ensure that the selectivity of the iodide-iodate reaction stayed constant throughout the run. The time dependent selectivity measurements during each run provide additional verification measurements that are compared with model predictions summarized in Chapter 6.

Table 3.3: Summary of the sampling procedure during acid dosing.

UV Sample	Sampling Intervals									
	Set 1 (C_1)		Set 2 (C_2)		Set 3 (C_3)		Set 4 (C_4)		Set 5 (C_5)	
	Time (min)	Vol. (mL)	Time (min)	Vol. (mL)	Time (min)	Vol. (mL)	Time (min)	Vol. (mL)	Time (min)	Vol. (mL)
1	0	0	0	0	0	0	0	0	0	0
2	1	4	2	4	2	4	1.2	2.4	1	2
3	2	8	4	8	4	8	2.4	4.8	2	4
4	3	12	6	12	6	12	3.6	7.2	3	6
5	4	16	8	16	8	16	4.8	9.6	4	8
6	5	20	10	20	10	20	6	12	5	10
7	5	20	10	20	10	20	6	12	5	10

3.1.3. List of Experiments

Measurements follow a factorial design of experiments methodology summarized in Table 3.4. The factorial design includes 15 experiments that consist of 5 concentrations and 3 stirring speeds using the retreat curve (RC) impeller and impeller dosing. The concentration set for each experiment corresponds to Table 3.2. Stirring speeds low, mid, and high correspond to 200 rpm, 400 rpm, and 600 rpm, respectively. Additional subsurface acid injection experiments were performed using the RC impeller at 400 rpm. A limited set of 5 experiments was also performed with a four bladed pitched blade impeller at 400 rpm with impeller dosing.

Table 3.4: Summary of the full list of experiments.

Run	Concentration Set	Stirring Speed	Feeding Location	Impeller
Run 6	C ₁	mid	impeller	50 mm RC
Run 7	C ₂	mid	impeller	50 mm RC
Run 8	C ₃	mid	impeller	50 mm RC
Run 9	C ₄	mid	impeller	50 mm RC
Run 10	C ₅	mid	impeller	50 mm RC
Run 11	C ₁	low	impeller	50 mm RC
Run 12	C ₂	low	impeller	50 mm RC
Run 13	C ₃	low	impeller	50 mm RC
Run 14	C ₄	low	impeller	50 mm RC
Run 15	C ₅	low	impeller	50 mm RC
Run 16	C ₁	mid	impeller	38 mm PBT
Run 17	C ₂	mid	impeller	38 mm PBT
Run 18	C ₃	mid	impeller	38 mm PBT
Run 19	C ₄	mid	impeller	38 mm PBT
Run 20	C ₅	mid	impeller	38 mm PBT
Run 21	C ₁	mid	Sub-surface	50 mm RC
Run 22	C ₂	mid	Sub-surface	50 mm RC
Run 23	C ₃	mid	Sub-surface	50 mm RC
Run 24	C ₄	mid	Sub-surface	50 mm RC
Run 25	C ₅	mid	Sub-surface	50 mm RC
Run 26	C ₁	high	impeller	50 mm RC
Run 27	C ₂	high	impeller	50 mm RC
Run 28	C ₃	high	impeller	50 mm RC
Run 29	C ₄	high	impeller	50 mm RC
Run 30	C ₅	high	impeller	50 mm RC

Note: Run 6 was performed using a sulfuric acid concentration of 0.05 mol/L.

3.1.4. Experimental Results and Discussion

This section provides a summary of experimental data analysis methods and presents the main experimental results. The experimental results are used for model validation in Chapter 6.

Figure 3.4 shows the relationship between UV spectrum and segregation index for samples taken during acid dosing during a fixed experiment operating at 400 rpm with a retreat curve impeller. Figure 3.4 (left) shows the UV spectrums of the samples drawn for a given sampling time. The signal for triiodide I_3^- at 353 nm increases as acid is being added to the system, indicating the formation of iodine I_2 . Figure 3.4 (right) shows segregation index plotted on top of the peaks given by the UV spectrum. As expected, the selectivity remains

approximately constant over the course of acid dosing. The reported value of segregation index in this thesis was computed by taking the mean value.

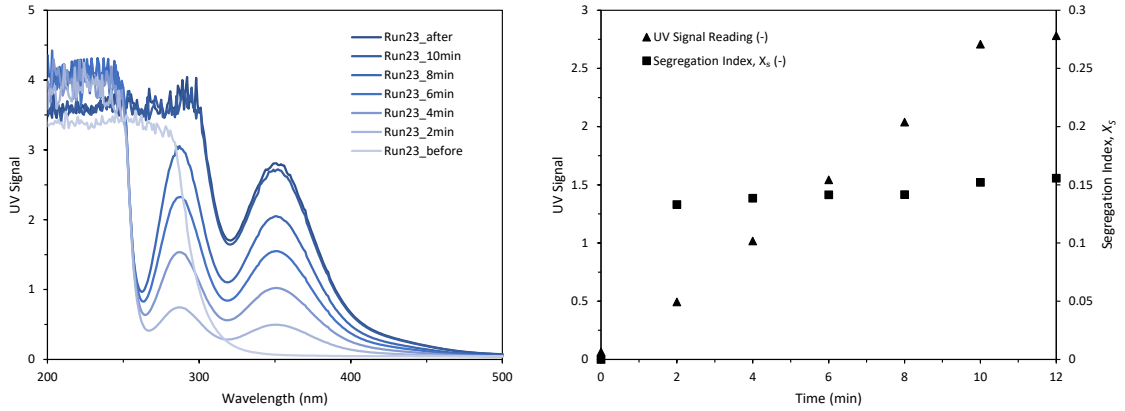


Figure 3.4: Relationship between UV spectrum of the samples drawn from the EasyMax during acid dosing and segregation index. UV spectrum (left) varying with respect to wavelength where triiodide corresponds to 353 nm. Segregation index and UV at 353 (right) as a function of time.

Figure 3.5 shows the relationship between segregation index and concentration of acid being injected. From Figure 3.5, two general trends are observed. First, an increase in concentration leads to higher value of segregation index indicating a lowering of mixing quality. It is important to remember that mixing quality is relative to the rate of the slower reaction. Since increasing the acid concentration increases the rate of the second reaction, the relative mixing quality decreases with acid concentration. Second, an increase in stir speed (i.e., Reynolds number) leads to a decrease in segregation index because mixing quality is increased.

Error bars are not included on Figure 3.5 and Figure 3.6 because replicates were not taken. However, aside from the variability in the sub-surface dosing experiments, which is expected due to interference from the free surface, the trends are smooth. Qualitatively, variance was expected to be highest at the highest Reynolds numbers and feeding at the free surface. At higher Reynolds numbers, the formation of air bubbles was sometimes observed around the impeller and feed location, which could have caused some variability in the results.

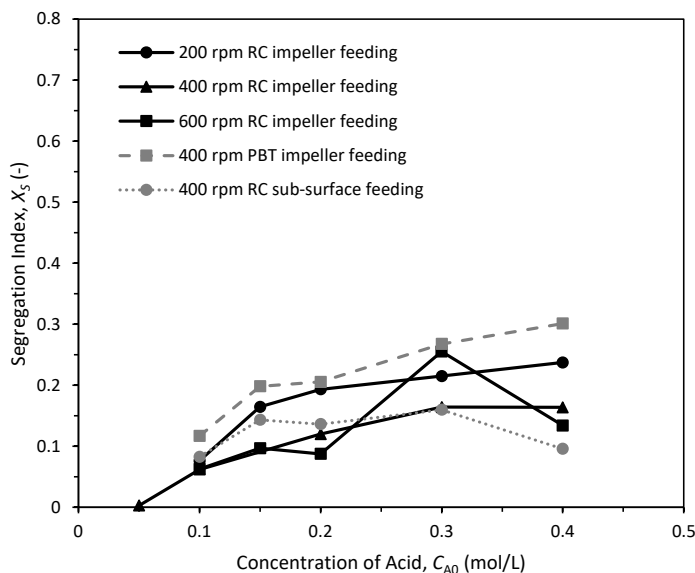


Figure 3.5: Relationship between segregation index X_S and concentration of acid for fixed Reynolds numbers. Solid black lines indicate the main set of experiments performed using the retreat curve impeller and feeding close to the impeller. The grey dotted line indicates the additional set of experiments where subsurface dosing was performed. The grey dashed line indicates the dataset obtained using pitched blade impeller.

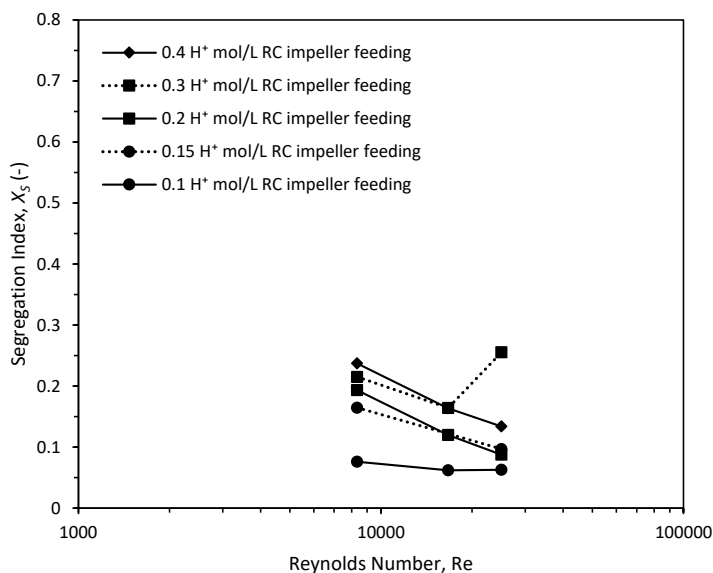


Figure 3.6: Segregation index X_S varying as a function of Reynolds number for fixed concentration of acid.

3.2. Modelling Methodology

3.2.1. Flow Fields and Turbulence Modelling

In this work, flow fields were calculated using the continuity equation and the conservation of linear momentum equation for an incompressible Newtonian fluid. Given that the stirred tank reactors being investigated typically operate in a transitional flow regime at Reynolds numbers of 5 000 or greater, turbulence is subject to non-isotropic conditions that make flow fields challenging to resolve. Although there are some limitations to the method, Reynolds-averaging was implemented to solve the mean velocity and pressure fields to reduce the need for very fine computational meshes. The Reynolds averaging procedure results in additional unknown quantities that require closure. These nonlinear terms introduced are known as the Reynolds stress. In this work, Boussinesq's hypothesis is used to close the Reynolds stress which models this term with respect to a strain tensor and turbulent viscosity. The incompressible Reynolds-averaged Navier-Stokes equations are expressed as follows:

$$\nabla \cdot (\vec{u}) = 0 \quad (3.9)$$

$$\frac{\partial \vec{u}}{\partial t} + \vec{u} \cdot \nabla \vec{u} = -\frac{1}{\rho} \nabla p + \nabla \cdot (v + v_t) [\nabla \vec{u} + (\nabla \vec{u})^T] \quad (3.10)$$

where ρ is the density of the fluid (kg/m³) and is assumed constant for incompressible fluids, \vec{u} is the the mean velocity vector (m/s), ∇p is the mean pressure gradient (Pa), $\nabla \vec{u}$ and $(\nabla \vec{u})^T$ are the mean velocity gradient and its transpose (Hz or s⁻¹), $v = \mu/\rho$ is the molecular kinematic viscosity of the fluid (m²/s), v_t is the turbulent kinematic viscosity of the fluid (m²/s), μ is the molecular dynamic viscosity of the fluid (Pa s), and t is time (s).

The transport equations for the standard k - ε model use the following transport equations for turbulent kinetic energy and turbulent kinetic energy dissipation rate:

$$\frac{\partial k}{\partial t} + \nabla \cdot (\vec{u}k) = \nabla \cdot \left[\left(v + \frac{v_t}{\sigma_k} \right) \nabla k \right] + G_k - \frac{2}{3} k (\nabla \cdot \vec{u}) - \varepsilon \quad (3.11)$$

$$\frac{\partial \varepsilon}{\partial t} + \nabla \cdot (\vec{u}\varepsilon) = \nabla \cdot \left[\left(v + \frac{v_t}{\sigma_\varepsilon} \right) \nabla \varepsilon \right] + C_{1\varepsilon} G_k \frac{\varepsilon}{k} - \frac{2}{3} C_{1\varepsilon} \varepsilon (\nabla \cdot \vec{u}) - C_{2\varepsilon} \frac{\varepsilon^2}{k} \quad (3.12)$$

$$v_t = C_\mu \frac{k^2}{\varepsilon} \quad (3.13)$$

where k is the turbulent kinetic energy of the fluid (m^2/s^2), ν_t is the turbulent viscosity (m^2/s), G_k is the turbulent kinetic energy production rate (m^2/s^3) and ε is the turbulent kinetic energy dissipation rate (m^2/s^3). Standard values are used for model constants: $C_\mu = 0.09$, $\sigma_k = 1.00$, $\sigma_\varepsilon = 1.30$, $C_{1\varepsilon} = 1.44$, and $C_{2\varepsilon} = 1.92$.

Power number was evaluated in two ways according to Coroneo et al. (2011) and Duan et al. (2019). First, power was calculated by summing the torques along the impeller. Second, power was computed by volume integrating the turbulent kinetic energy dissipation rate, which results in the total energy dissipated. Torque based power number was evaluated as the summation of normal pressure forces and viscous forces along the impeller surface. Each pressure contribution is multiplied by the face area and the distance from the origin, which results in a torque:

$$M = \int_V (\nabla \cdot \boldsymbol{\tau}) dV = \int_A (\mathbf{n} \cdot \boldsymbol{\tau}) \times r dA \quad (3.14)$$

where M is the total torque (N m), r is the radial distance from the shaft centreline to a specified face centre (m). Eq. (3.14) results in a tensor with negligible torque in the x and y -directions. Therefore, M is taken as the torque in the z -direction. Torque based power is then expressed as follows:

$$N_{P,M} = \frac{2\pi NM}{\rho N^3 D^5} \quad (3.15)$$

where N is the stir speed (s^{-1}), D is the diameter of the impeller (m), and the numerator represents the power delivered from the impeller to the fluid $P_M = 2\pi NM$ (W). Power number was also evaluated by calculating the total turbulent kinetic energy dissipated. The power dissipated is evaluated using the following expression:

$$P_\varepsilon = \int_V (\rho \varepsilon) dV \quad (3.16)$$

where P_ε is the total power dissipated due to turbulence and is the volume integral of ε (W). Power number based on dissipation is expressed as follows:

$$N_{P,\varepsilon} = \frac{P_\varepsilon}{\rho N^3 D^5} \quad (3.17)$$

where $N_{p,\varepsilon}$ is the dimensionless power number based on dissipation (-). The pressure term in Eq. (3.18) represents the work done by the impeller on the fluid, and is given by the following integral:

$$\int_V (\nabla \cdot p\vec{u})dV \quad (3.18)$$

The volume integral of Eq. (3.16) should match the pressure drop based energy dissipation exactly in a continuous flow case (Plawsky, 2014). Viscous Dissipation represents irreversible heating of the fluid by converting kinetic energy into internal energy through shear and is evaluated as follows:

$$\int_V (\boldsymbol{\tau}:\nabla\vec{u})dV \quad (3.19)$$

In laminar flow conditions, the rule-of-thumb proposed in Paul et al. (2004) is extended to consider mesh resolution by comparing the volume integral of viscous dissipation shown in Eq. (3.19) with the force-based volume integral in Eq. (3.17) or the volume integral in Eq. (3.20). This allows for flexibility as the approach can be adopted for continuous flow cases and non-turbulent flow conditions. The kinetic energy and viscous work terms were used as a check because they should be negligible compared to the pressure term. Therefore, the volume integrals below should be negligible:

$$\int_V p(\nabla \cdot \vec{u})dV \quad (3.20)$$

where Eq. (3.20) represents the reversible conversion of kinetic energy into internal energy that is typical in sudden expansion or compression systems. Work done by viscous force:

$$\int_V \nabla \cdot (\boldsymbol{\tau} \cdot \vec{u})dV \quad (3.21)$$

where τ is the shear-rate tensor (s^{-1}). The convection of kinetic energy:

$$\int_V \left(\nabla \cdot \vec{u} \frac{1}{2} \rho \vec{u}^2 \right) dV \quad (3.22)$$

3.2.2. Competitive-Parallel Reactions

In this thesis, although only the iodide-iodate competitive-parallel reaction scheme was studied experimentally, three schemes were simulated in various geometries to investigate micromixing performance. All three reaction schemes consist of an infinitely fast reaction

coupled with a finite-rate reaction. The first adopted reaction scheme in this thesis consists of an infinitely fast reaction (3.IV) coupled with a second finite-rate reaction (3.V):



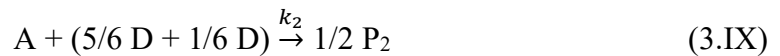
where reactions (3.IV) and (3.V) are described by second-order rate laws. This scheme is representative of the commonly used fourth Bourne reaction, where the slower reaction is catalytic with respect to component A. As in experiments performed by Johnson and Prud'homme and simulation work of Liu and Fox (2006), the rate constant of the slower reaction is given by $k_2 = 0.67313 \text{ mol/m}^3/\text{s}$ at 25 °C and is used for all simulations. Components A, B, and D follow a molar ratio of 1:1.05:1, respectively.

The second adopted reaction scheme in this thesis consists of an infinitely fast reaction (3.VI) coupled with a second finite-rate reaction (3.VII):



where reactions (3.VI) and (3.VII) are described by second-order rate laws. This scheme is representative of the commonly used third Bourne reaction, where the slower reaction is not catalytic with respect to component A. As in experiments performed by Yu and Bourne (1994) and Akiti and Armenante (2004), all simulations use a rate constant of the slower reaction given by $k_2 = 0.0257 \text{ mol/m}^3/\text{s}$ for a temperature of 25 °C.

A third adopted reaction scheme in this thesis consists of an infinitely fast reaction (3.VIII) coupled with a second finite-rate reaction (3.IX):



where reaction (3.VIII) is described by a second-order rate law and reaction (3.IX) follows a fifth-order rate law expressed as Eq. (3.23). This scheme is representative of the commonly used iodide-iodate reaction scheme where component A is hydrogen ions H^+ , component B is borate ions $B(OH)_4^-$, component D represents iodide ions I^- , component E

is iodate ions IO_3^- , and component P_2 is formed iodine I_2 . It is assumed component D and E react together. According to Guichardon and Falk (2000), the rate of the slower reaction is given by the following expression:

$$R_2 = k_2(C_A)^2(C_D)^2(C_E) \quad (3.23)$$

where C_A is the concentration of acid (mol/m^3), C_D is the concentration of iodide ions I^- (mol/m^3), and C_E is the concentration of iodate ions IO_3^- (mol/m^3), I is the ionic strength of solution (mol/m^3), k_2 is the rate constant for the slower reaction and varies with respect to the ionic strength of solution. The original expression for k_2 presented by Guichardon and Falk (2000) is transformed to units of $\text{m}^{12}/\text{mol}^4/\text{s}$ and is shown in Eq. (3.77).

The CFD model for solving mixing-limited reactions was implemented using the two-environment direct quadrature method of moments (DQMOM) model coupled with an interaction-by-exchange-with-the-mean (IEM) model (Liu & Fox, 2006). The DQMOM model solves the composition probability density function (PDF) transport equations. The IEM coupling serves to close the conditional molecular diffusion term. This work uses OpenFOAM to implement the two-environment DQMOM-IEM model based on the computational approach of Liu and Fox (2006). The model requires one conservation equation to track mixing of the two environments:

$$\frac{\partial \alpha_1}{\partial t} + \nabla \cdot (\bar{u} \alpha_1) = \nabla \cdot (D_T \alpha_1) + \nabla \cdot \left(\frac{v_t}{Sc_t} \nabla \alpha_1 \right) \quad (3.24)$$

where α_1 is the volume fraction of the first environment. The second environment is bounded by $\alpha_2 = 1 - \alpha_1$. In this model, two conservation equations are required to track the mixture fraction in the two environments:

$$\frac{\partial \alpha_1 X_1}{\partial t} + \nabla \cdot (\bar{u} \alpha_1 X_1) = \nabla \cdot (D_T \nabla (\alpha_1 X_1)) + \nabla \cdot \left(\frac{v_t}{Sc_t} \nabla (\alpha_1 X_1) \right) + \gamma \alpha_1 \alpha_2 (X_2 - X_1) \quad (3.25)$$

$$\frac{\partial \alpha_2 X_2}{\partial t} + \nabla \cdot (\bar{u} \alpha_2 X_2) = \nabla \cdot (D_T \nabla (\alpha_2 X_2)) + \nabla \cdot \left(\frac{v_t}{Sc_t} \nabla (\alpha_2 X_2) \right) + \gamma \alpha_2 \alpha_1 (X_1 - X_2) \quad (3.26)$$

where X_1 and X_2 are the mixture fractions in environments 1 and 2, respectively. The last terms in these equations, $\gamma \alpha_1 \alpha_2 (X_2 - X_1)$ and $\gamma \alpha_2 \alpha_1 (X_1 - X_2)$, represent the exchange between

the environments due to micromixing. Two final equations are required to track the reaction-progress variable of the second reaction in each environment:

$$\frac{\partial \alpha_1 Y_{21}}{\partial t} + \nabla \cdot (\bar{u} \alpha_1 Y_{21}) = \nabla \cdot (D_T \nabla (\alpha_1 Y_{21})) + \nabla \cdot \left(\frac{v_t}{Sc_t} \nabla (\alpha_1 Y_{21}) \right) + \gamma \alpha_1 \alpha_2 (Y_{22} - Y_{21}) + \alpha_1 S_{2\infty}(X_1, Y_{21}) \quad (3.27)$$

$$\frac{\partial \alpha_2 Y_{22}}{\partial t} + \nabla \cdot (\bar{u} \alpha_2 Y_{22}) = \nabla \cdot (D_T \nabla (\alpha_2 Y_{22})) + \nabla \cdot \left(\frac{v_t}{Sc_t} \nabla (\alpha_2 Y_{22}) \right) + \gamma \alpha_2 \alpha_1 (Y_{22} - Y_{21}) + \alpha_2 S_{2\infty}(a_k, Y_{22}) \quad (3.28)$$

where Y_{21} and Y_{22} are the reaction-progress variables for the second reaction in environments 1 and 2, respectively. The reaction source terms for the first $S_{21\infty}(X_{21}, Y_{21})$ and second $S_{22\infty}(X_{22}, Y_{22})$ environment depend on the implemented chemical reaction rate law scheme. The reaction source term for the fourth Bourne reaction is given by the following equation:

$$S_{2\infty}(a_k, Y_{2k}) = C_{A0} k_2 \left(1 - \frac{X_k}{X_{s1}} \right) \left(\frac{X_k}{X_{s2}} - Y_{2k} \right) \quad \text{if } 0 \leq X_k \leq \frac{X_k}{X_{s1}} \text{ and } 0 \leq Y_{2k} \leq X_k \quad (3.29)$$

where $k = 1$ or 2 represents the mixing environment. Since reaction (I) is considered instantaneous, its progress variable in the two environments can be calculated explicitly for the fourth Bourne reaction from the follow expression:

$$Y_{1k} = \min \left(\frac{X_k}{X_{s1}}, \frac{1-X_k}{1-X_{s1}} \right) \quad (3.30)$$

where the stoichiometric mixture fraction is given by the following equations:

$$X_{s1} = \frac{C_{A0}}{C_{A0} + C_{B0}} \quad (3.31)$$

$$X_{s2} = \frac{C_{A0}}{C_{A0} + C_{D0}} \quad (3.32)$$

and C_{A0} , C_{B0} , and C_{D0} are initial concentrations of components A, B, and D. After obtaining the solution of the mixture fraction and reaction progress variables, the reactant concentrations according to the fourth Bourne reaction scheme in each environment (C_{Ak} , C_{Bk} , and C_{Dk}) can be determined using the following equations:

$$C_A = C_{A0}(1 - X_k - [1 - X_{s1}]Y_{1k}) \quad (3.33)$$

$$C_B = C_{B0}(X_k - X_{s1}Y_{1k}) \quad (3.34)$$

$$C_D = C_{D0}(X_k - X_{s2}Y_{2k}) \quad (3.35)$$

The average concentrations of the reactants (\bar{C}_A , \bar{C}_B , and \bar{C}_D) are then determined from the local concentrations and volume fractions of the two environments using the following expressions:

$$\bar{C}_A = \alpha_1 C_{A1} + \alpha_2 C_{A2} \quad (3.36)$$

$$\bar{C}_B = \alpha_1 C_{B1} + \alpha_2 C_{B2} \quad (3.37)$$

$$\bar{C}_D = \alpha_1 C_{D1} + \alpha_2 C_{D2} \quad (3.38)$$

The conversion of reactant D in the slower finite-rate reaction (X_D) is used as a measure of mixing quality and is calculated as follows:

$$X_D = 1 - \frac{\bar{C}_D}{\bar{a}C_{D0}} \quad (3.39)$$

where \bar{C}_D is the mass-weighted outlet concentration of D, and the global mean mixture fraction \bar{a} is 0.5 for mixing of streams with equal flow rates.

The same conservation equations (Eqs. (3.24)–(3.28)) must be solved to simulate the third Bourne reaction scheme. However, the source terms and reactant concentrations must be calculated differently. The reaction source term for the slower reaction in the third Bourne reaction scheme is given by the following equation:

$$S_{2\infty}(a_k, Y_{2k}) = C_{A0}k_2X_{s2} \left(\frac{X_k - X_{s1}}{X_{s2}(1 - X_{s1})} - Y_{2k} \right) \left(\frac{1 - X_k}{1 - X_{s2}} - Y_{2k} \right)$$

if $X_{s1} + Y_{2k}X_{s2}(1 - X_{s1}) \leq X_k \leq 1 - Y_{2k}(1 - X_{s2})$

$$\text{and } 0 \leq Y_{2k} \leq \frac{1 - X_{s1}}{1 - X_{s2} + X_{s2}(1 - X_{s1})} \quad (3.40)$$

where $k = 1$ or 2 represents the mixing environment. The chemical source terms are scaled by the maximum concentration of product. Since the faster is considered instantaneous, its progress variable in the two environments can be calculated explicitly from the following expression:

$$Y_{1k} = \min \left(\frac{1 - X_k}{1 - X_{s1}}, \frac{X_k}{X_{s1}} - \frac{X_{s2}}{X_{s1}} Y_{2k} \right) \quad (3.41)$$

where the stoichiometric mixture fraction is given by the following equations:

$$X_{S1} = \frac{C_{B0}}{C_{A0} + C_{B0}} \quad (3.42)$$

$$X_{S2} = \frac{C_{D0}}{C_{A0} + C_{D0}} \quad (3.43)$$

and C_{A0} , C_{B0} , and C_{D0} are the initial concentrations of components A, B, and D. After obtaining the mixture fraction and reaction progress variables, the reactant concentrations in each environment (C_{Ak} , C_{Bk} , and C_{Dk}) can be determined using the following equations:

$$C_A = C_{A0}(X_k - X_{S1}Y_{1k} - X_{S2}Y_{2k}) \quad (3.44)$$

$$C_B = C_{B0}(X_k - [1 - X_{S1}]Y_{1k}) \quad (3.45)$$

$$C_D = C_{D0}(X_k - [1 - X_{S2}]Y_{2k}) \quad (3.46)$$

According to Watanabe et al. (2014), the chemical source terms are scaled by the maximum concentration of product. This maximum is evaluated by setting $X_k = X_{S2}$ and C_A or $C_B = 0$ in the reactant concentration equations. The scaling parameter for the second reaction results in $\gamma_2 = C_{A0}C_{D0}/(C_{A0} + C_{D0})$. The average concentrations of the reactants (\bar{C}_A , \bar{C}_B , and \bar{C}_D) are then determined from the local concentrations and volume fractions of the two environments using Eqs. (3.40), (3.41), and (3.42).

The global mean concentration of each component is the volume weighted average over the tank volume:

$$\bar{\bar{C}}_A = \frac{1}{V} \int \bar{C}_A dV = \frac{\Sigma(\bar{C}_A \Delta V)}{\Sigma \Delta V} \quad (3.47)$$

$$\bar{\bar{C}}_B = \frac{1}{V} \int \bar{C}_B dV = \frac{\Sigma(\bar{C}_B \Delta V)}{\Sigma \Delta V} \quad (3.48)$$

$$\bar{\bar{C}}_D = \frac{1}{V} \int \bar{C}_D dV = \frac{\Sigma(\bar{C}_D \Delta V)}{\Sigma \Delta V} \quad (3.49)$$

The yield of product P_2 in the slower reaction (X_{S2}) is used as a measure of mixing quality and is expressed as follows:

$$X_{S2} = \frac{\bar{\bar{C}}_{P2}}{\bar{\bar{C}}_{P1} + \bar{\bar{C}}_{P2}} \quad (3.50)$$

where C_{P2} is the volume integral (i.e., total amount) of product formed due to the slower reaction, taken as the amount of reacted D, and C_{P1} is the volume integral of product formed

due to the infinitely fast reaction, taken as reacted B. If equal amounts of A, B, and D are reacted, the maximum value of X_{S2} is 0.5, which indicates low mixing quality. Perfect mixing results in zero reacted D and gives a value X_{S2} of 0. Values between 0 and 0.5 indicate intermediate levels of mixing quality.

Similar to the third and fourth Bourne reaction schemes, the same conservation equations (Eqs. (3.24)–(3.28)) must be solved to simulate the Villermaux-Dushman reaction scheme. The reaction source term for the slower reaction in the Villermaux-Dushman reaction scheme is given by the following equation:

$$S_{2\infty}(a_k, Y_{2k}) = k_2 C_{A0}^4 X_{S2}^4 \left(\frac{X_k - X_{S1}}{X_{S2}(1 - X_{S1})} - Y_{2k} \right)^2 \left(\frac{1 - X_k}{1 - X_{S2}} - Y_{2k} \right)^3$$

if $X_{S1} + Y_{2k} X_{S2} (1 - X_{S1}) \leq X_k \leq 1 - Y_{2k} (1 - X_{S2})$
and $0 \leq Y_{2k} \leq \frac{1 - X_{S1}}{1 - X_{S2} + X_{S2}(1 - X_{S1})}$ (3.51)

where $k = 1$ or 2 represents the mixing environment. Since the faster reaction is considered instantaneous, its progress variable in the two environments can be calculated explicitly from the follow expression:

$$Y_{1k} = \min \left(\frac{1 - X_k}{1 - X_{S1}}, \frac{X_k}{X_{S1}} - \frac{X_{S2}}{X_{S1}} Y_{2k} \right) \quad (3.52)$$

where the stoichiometric mixture fraction is given by the following equations:

$$X_{S1} = \frac{C_{B0}}{C_{A0} + C_{B0}} \quad (3.53)$$

$$X_{S2} = \frac{C_{D0}}{C_{A0} + C_{D0}} \quad (3.54)$$

and C_{A0} , C_{B0} , and C_{D0} are the initial concentrations of components A, B, and D. After obtaining the solution of the mixture fraction and reaction progress variables, the reactant concentrations in each environment (C_{Ak} , C_{Bk} , and C_{Dk}) can be determined using Eqs. (3.43), (3.44), and (3.45).

Due to the dependence of ionic strength on the rate constant k_2 in the Villermaux-Dushman reactions, an additional reactant representing sulfate ion (SO_4^{2-}) introduced by the sulfuric acid injection is included in the mass balances. Acid is assumed to be completely dissociated. This acts as a non-reacting tracer as follows:

$$C_S = C_{S0}X_k \quad (3.55)$$

The ionic strength is determined using the local concentrations in the first environment as follows:

$$I = \frac{1}{2}(C_{A1} + 4C_{S1} + 2C_{B1} + 2C_{D1}) \quad (3.56)$$

where I has units mol/m³. The rate constant k_2 is now represented as a field that depends on local values of ionic strength. The average concentrations of the reactants (\bar{C}_A , \bar{C}_B , and \bar{C}_D) are then determined from the local concentrations and volume fractions of the two environments using Eqs. (3.40), (3.41), and (3.42).

The global mean concentration of each component is the volume weighted average over the tank volume outlined in Eqs. (3.51), (3.52), and (3.53).

The selectivity of the slower reaction (Y) is used as a measure of mixing quality and is expressed as the ratio of A consumed (or P_2 produced) by the second reaction and A injected:

$$Y = \frac{2V_{tank}\bar{C}_{P2}}{V_{inj}C_{A0}} \quad (3.57)$$

where V_{tank} is the volume of the reactor (m³), V_{inj} is the volume of injected A (m³), C_{P2} is the product formed due to the slower reaction, and C_{A0} is the initial concentration of injected A (mol/m³). The maximum value of Y is given by the following equation:

$$Y_{ST} = \frac{6C_{E0}}{6C_{E0} + C_{B0}} \quad (3.58)$$

where C_{E0} and C_{B0} represent the initial amounts of iodate IO_3^- and borate ions $B(OH)_4^-$, respectively. The segregation index was then computed as follows:

$$X_S = \frac{Y}{Y_{ST}} \quad (3.59)$$

where X_S is zero under conditions of perfect mixing and 1 when mixing quality is poor.

3.2.3. Scales of Mixing and Mixing Times

Additional equations are required to estimate mixing times and to close the source terms in Eqs. (3.24)–(3.28). Equations (3.9) and (3.10) alone with the k - ϵ turbulence model are

solved first. The distribution of micromixing time scales is then determined locally with respect to the mixture fraction (a_1) and its variance (a_2) as follows:

$$\frac{\partial a_1}{\partial t} + \nabla \cdot (\bar{u}a_1) = \nabla \cdot (D_T a_1) + \nabla \cdot \left(\frac{\nu_t}{Sc_t} \nabla a_1 \right) \quad (3.60)$$

$$\frac{\partial a_2}{\partial t} + \nabla \cdot (\bar{u}a_2) = \nabla \cdot (D_T a_2) + \nabla \cdot \left(\frac{\nu_t}{Sc_t} \nabla a_2 \right) + 2 \frac{\nu_t}{Sc_t} |\nabla a_1|^2 - 2\gamma a_2 \quad (3.61)$$

where the term $2\gamma a_2$, is a dissipation term due to micromixing. The turbulent viscosity (ν_t) is computed from the standard k - ε turbulence model.

Liu and Fox (2006) characterized mixing by two types of segregation based on a_1 and a_2 : large-scale segregation (LSS), and small-scale segregation (SSS). LSS is evaluated as deviations of the mixture fraction from the mean:

$$a_3 = (a_1 - \bar{a})^2 \quad (3.62)$$

where \bar{a} is the global mean mixture fraction. Based on Eqs. (3.60) and (3.62), the characteristic time of LSS variance decay (t_{LSS}) is defined as follows:

$$t_{LSS} = \frac{a_3}{2 \left(\frac{\nu_t}{Sc_t} \right) |\nabla a_1|^2} \quad (3.63)$$

The system achieves macromixing when t_{LSS} approaches zero, which leads to the production of SSS. The decay time of SSS (t_{SSS}) is as follows:

$$t_{SSS} = \frac{1}{2\gamma} \quad (3.64)$$

The micromixing time parameter γ (s^{-1}) is modelled as a function of turbulent kinetic energy k (m^2/s^2) and turbulent kinetic energy dissipation rate ε (m^2/s^3):

$$\gamma = \frac{C_\phi \varepsilon}{2 k} \quad (3.65)$$

where C_ϕ is an empirical mixing coefficient that describes the mechanical-to-scalar-time-scale. For fully turbulent, high Reynolds number flow $C_\phi \approx 2.0$. Liu and Fox (2006) provide the following expression to evaluate C_ϕ according to a local Reynolds number (Re_t):

$$C_\phi = 0.4093 + 0.6015(\log_{10} Re_t) + 0.5851(\log_{10} Re_t)^2 + 0.09472(\log_{10} Re_t)^3 - 0.3909(\log_{10} Re_t)^4 + 0.1461(\log_{10} Re_t)^5 - 0.01604(\log_{10} Re_t)^6 \quad (3.66)$$

where

$$Re_t = \frac{k}{(\varepsilon\nu)^{1/2}} \quad (3.67)$$

and $Sc_t = 0.7$ has been assumed. The distribution of t_{SSS} throughout a given flow system was used to determine a mean characteristic mixing time.

3.2.4. Engulfment Model

The approach described in sections 3.2.2 and 3.2.3 provides a CFD framework to simulate competitive-parallel reactions. Alternatively, as described in Chapter 2, many previous studies have used reduced-order models, such as the E-model, to analyze micromixing. An alternative strategy to the models presented in sections 3.2.2 and 3.2.3, proposed by Duan et al. (2016), is to couple the E-model to the CFD predictions. This approach is a compromise between using the E-model globally and applying a full CFD model.

In the present work, coupling of the E-model to CFD is explored as an alternative to the models in sections 3.2.2 and 3.2.3. To implement this approach, reaction zones can be determined by first solving Eq. (3.9) and Eq. (3.10), along with the standard k - ε turbulence model for steady-state flow fields and turbulence parameters (Eqs. (3.12) and (3.13)). The distribution of turbulent kinetic energy and dissipation can then be evaluated locally using Eqs. (3.78)–(3.83) and leads to an arbitrary reaction zone.

The average values of turbulent kinetic energy k_R (m^2/s^2) and turbulent kinetic energy dissipation rate ε_R (m^2/s^3) in the reaction zone for the E-model and are evaluated according to Duan et al. (2016) as the mixture fraction variance weighted average:

$$\varepsilon_R = \frac{\sum(a_2\varepsilon)}{\sum(a_2)} \quad (3.68)$$

$$k_R = \frac{\sum(a_2k)}{\sum(a_2)} \quad (3.69)$$

In theory, weighting the turbulence parameters based on a_2 , leads to values of zero through most of the system and therefore k_R and ε_R are most impacted by regions of inadequate mixing (i.e., close to the feeding zone or impinging zone). The segregation index for each reaction scheme is evaluated through the E-model with self-engulfment and represents the mass balance equations for each reactant in the growing reaction zone.

$$\frac{dV}{dt} = EV \left(1 - \frac{V e^{-t/\tau_s}}{V_{A0}/\sigma} \right) \quad (3.70)$$

$$\frac{dC_i}{dt} = E(C_{i,\infty} - C_i) \left(1 - \frac{V e^{-t/\tau_s}}{V_{A0}/\sigma} \right) + R_i \quad (3.71)$$

where C_i is the concentration of component i in the growing reaction zone (mol/m^3), $C_{i,\infty}$ is the surroundings concentration of component i (mol/m^3), V_0 is the initial concentration of the growing reaction zone (m^3), and R_i is the reaction rate (mol/s). The feed is discretized into σ parts j . During the integration of Eqs. (3.92) and (3.93), $C_{i,\infty}$ is constant; however, the surrounding environment concentration is updated by a mass balance.

$$\frac{dC_i}{dt} = E(C_{i,\infty} - C_i) \left(1 - \frac{V e^{-t/\tau_s}}{V_{A0}/\sigma} \right) + R_i \quad (3.72)$$

The parameter τ_s is related to the bulk blending time and is commonly referred to as the time for dissipation of segregation in the inertial-convective sub-range (Vicium et al., 2004; Vicium & Mazzotti, 2007). It is calculated as follows:

$$\tau_s = k_R / (2\varepsilon_R) \quad (3.73)$$

The engulfment rate parameter is determined as follows:

$$E = 0.058(\varepsilon_R/\nu)^{1/2} \quad (3.74)$$

where E is the engulfment rate (s^{-1}). The E-model describes micromixing by the reacting volume V_A engulfing a portion of V at a rate proportional to the engulfment rate parameter.

All simulations are performed without self engulfment unless otherwise stated. Without self-engulfment, Eqs. (3.92) and (3.93) are written as follows:

$$\frac{dV}{dt} = EV \quad (3.75)$$

$$\frac{dC_i}{dt} = E(C_{i,\infty} - C_i) + R_i \quad (3.76)$$

3.3. Simulation Sequence

All CFD simulations were completed using OpenFOAM. All simulations used the kinematic viscosity and density of water at 25 °C ($8.9 \times 10^{-7} \text{ m}^2/\text{s}$ and 997 kg/m^3). The molecular diffusion coefficient was specified to be $1.0 \times 10^{-9} \text{ m}^2/\text{s}$, but this value should

not be critical because turbulent diffusion was dominant in all cases, and the turbulent Schmidt number was specified to be 0.7 in all simulations.

3.3.1. Steady-State Flow Field

The steady-state incompressible flow field variables were solved using OpenFOAM's simpleFOAM solver, which implements the semi-implicit method for pressure linked equations (SIMPLE) algorithm to iteratively solve for the pressure and velocity fields. Equation (3.10) is discretized and rearranged for velocity, then combined with the continuity equation shown in Eq. 3.9. The simpleFoam solver, in combination with the standard k - ε turbulence model, yields the steady-state mean values of pressure, velocity, turbulent kinetic energy, and turbulent kinetic energy dissipation rate.

3.3.2. Power Number

Power number was evaluated using the quasi-steady-state velocity and turbulence fields by solving Eqs. (3.16) and (3.18). The former integrates the product of pressure and radial distance along the shaft and impeller boundaries, which results in a torque and subsequently power. The latter integrates turbulent energy dissipation rate over the volume and represents the energy that is dissipated due to turbulence.

Mesh quality was assessed through successive refinement. Additionally, as explained in Chapter 2, the torque-based power number converges more quickly than the dissipation-based power number upon mesh refinement. Therefore, the ratio of these two power numbers was monitored to further analyze mesh convergence.

3.3.3. Competitive-Parallel Reactions

Competitive-parallel reaction simulations were performed using a two-step procedure. First, the steady-state incompressible velocity and turbulence variable fields were initialized by solving Eqs. (3.9) and (3.10) along with the k - ε turbulence model (Eqs. (3.11) and (3.12)). This was done using the simpleFOAM solver. Second, the reactant concentration fields and either conversion or yield were computed with respect to the reaction scheme being implemented. Each scheme requires solution of Eqs. (3.22)–(3.26), with the key difference being in the source term tracking the reaction progress variable in Eqs. (3.25) and (3.26).

Reactant concentration fields and conversion of D in the fourth Bourne reaction were computed using the source term closure relationships in Eqs. (3.27)–(3.37) and auxiliary relationships in Eqs. (3.74)–(3.76). Reactant concentration fields and yield of P₂ in the third Bourne reaction were computed using the source term closure relationships in Eqs. (3.38)–(3.51) and auxiliary relationships in Eqs. (3.75)–(3.77). Reactant concentration fields and segregation index in the Villermaux-Dushman reaction were computed using the source term closure relationships in Eqs. (3.52)–(3.71) and auxiliary relationships in Eqs. (3.75)–(3.77).

In the continuous flow confined impinging jet reactor simulations, fluid streams containing A ($\alpha_1 = 1, X_1 = 0, X_2 = 0, Y_{21} = 0, Y_{22} = 0$) and B + D ($\alpha_1 = 0, X_1 = 0, X_2 = 1, Y_{21} = 0, Y_{22} = 0$) were introduced at opposite ends of the CIJR. In the simulations involving stirred tank reactors, fluid streams containing A ($\alpha_1 = 0, X_1 = 0, X_2 = 0, Y_{21} = 0, Y_{22} = 0$) and B + D ($\alpha_1 = 0, X_1 = 0, X_2 = 0, Y_{21} = 0, Y_{22} = 0$) were introduced by applying source terms to α_1 and X_1 to allow for injection of these variables. The reactor domain is initially filled with the second environment. Reactive mixing simulations that use the fourth and third Bourne reactions only require the initial inlet concentrations C_{A0} , C_{B0} , and C_{D0} and a finite reaction rate constant, k_2 . Villermaux-Dushman reactions require concentrations C_{A0} , C_{S0} , C_{B0} , and C_{D0} and the rate constant is computed in accordance with ionic strength. The kinetics of Guichardon and Falk (2000) have been transformed into units of mol/m³ and are evaluated given by the following equation:

$$k_2 = 10^{\left((9.28105 - 12) - \frac{3.664}{\sqrt{1000}} \sqrt{I} \right)} \text{ if } I < 166 \text{ mol/m}^3$$

$$k_2 = 10^{\left((8.383 - 12) - \frac{1.5112}{\sqrt{1000}} \sqrt{I} + \frac{0.23689}{1000} I \right)} \text{ if } I > 166 \text{ mol/m}^3 \quad (3.77)$$

where k_2 has units m¹²/mol⁴/s.

3.3.4. Numerical Solvers and Schemes

Steady-state pressure and velocity fields were solved using the geometric-algebraic multi-grid (GAMG) and the stabilized preconditioned biconjugate gradient (PBiCGStab) solvers, respectively. The PBiCGStab solver was also used to determine mixture fraction and reaction progress fields. Turbulence model transport variables (k , ε , ν_t , Re_t) as well as

volume fraction of environment 1 were calculated using Eqs. (3.11), (3.12), (3.13), and (3.67). An under-relaxation factor of 0.3 was used for pressure and 0.7 was used for all other variables to limit oscillations between iterations. Unless otherwise noted in Chapter 4 and Chapter 5, the residuals for pressure, velocity, and turbulence variables were converged to at least 10^{-4} . Changes in the pressure and velocity fields were also monitored to ensure convergence was achieved. Residuals for mixture fraction and reaction progress were converged to at least 10^{-4} . Due to the long acid injection times, as long as 20 minutes in the stirred tank reactors, convergence was also assessed by monitoring changes with respect to the selectivity of the slower reaction. A time step of 1×10^{-4} s was used for reactive simulations. This results in a maximum Courant number of 0.50 for all simulations performed. Boundary conditions are summarised in Chapters 4–6 for the various simulation cases.

3.4. Summary

A DQMOM-IEM model was implemented in OpenFOAM to predict the reactive mixing for three competitive-parallel reaction schemes. In Chapters 4–6, the solver is used to model various reactors using the fourth Bourne reaction, third Bourne reaction and Villiermaux-Dushman reaction in both continuous flow and batch systems. The steady-state flow model used simpleFoam with modification to the pressure equation to account for the presence of mass source injection. Turbulence parameters were determined using the standard $k-\varepsilon$ turbulence model.

Experiments were performed to measure the segregation index of Villiermaux-Dushman competitive-parallel reactions in small-scale stirred tank crystallization reactors. Micromixing experiments were performed in the EasyMax402 reactor operating with various feed locations, feed concentrations, and stirring speeds. Acid was either fed at the free surface or at the impeller blade tip. Feed concentration was 0.05–0.4 mol/L. Impeller stir speeds ranged were 200–600 rpm, which corresponds to Reynolds numbers of 8 333–25 000 using the retreat curve impeller. The downward pumping pitch blade impeller used a stir speed set to 400 rpm, resulting in a Reynolds number of 9 600. The purpose for performing these in-house experiments was two-fold. First, the experimental measurements were used to validate the DQMOM-IEM implementation (Chapter 6) for a

commonly used crystallization reactor. Second, the data provide measurements in the range where the reactor is influenced by both micromixing and reaction kinetics.

CHAPTER 4: MODELLING FLUID DYNAMICS IN STIRRED TANKS

4.1. Introduction

The purpose of this chapter is to investigate and validate the modelling approach used for hydrodynamics and power predictions for the types of stirred tank reactors studied in this work. The selected validation cases are based on experimental studies of Blais et al. (2016) and Chapple et al. (2002). The goal of these case studies is to investigate hydrodynamics and power number predictions over various impeller types, flow conditions, and meshing strategies for the rotating zone.

4.2. Blais Case

Blais (2016) experimentally measured torque on the shaft and used the results to plot power number (N_p) against Reynolds number (Re). These experiments used a fully baffled tank (four evenly spaced full height baffles) and downward pumping pitched blade impeller (PBTD) for Reynolds numbers of $Re = 1-2100$. Blais et al. (2016) extended their work by comparing measured torque values with simulation predictions using a transient sliding mesh technique with large eddy simulation (LES) for turbulence modelling. In the present work, simulations were performed using both a pseudo-steady-state multiple reference frame (MRF) technique as well as a transient sliding mesh method, and the results were compared to the experimental and simulation data of Blais et al. (2016). The $k-\varepsilon$ model, which is based on the Reynolds-Averaged Navier-Stokes (RANS) technique, was used for turbulence modelling. This case study was specifically chosen because the selected Reynolds numbers capture both laminar and transitional flow conditions and because of the availability of both experimental data and simulation results for comparison. Furthermore, Blais et al. (2016) considered a pitched blade turbine, which is a commonly used impeller type in crystallization processes.

4.2.1. Geometry

Blais et al. (2016) performed experiments and simulations for a small-scale tank having a 0.365 m diameter ($T = 0.365$ m) with a 0.12167 m diameter ($D = 0.12167$ m) pitched blade

turbine. The impeller off bottom clearance was $C = T/4$ and baffle widths were $B = T/10$. Liquid height was maintained at the tank diameter ($H = T$). A sketch of the geometry and dimensions used for the Blais case study simulations are shown in Figure 4.1, and important geometric values summarized in Table 4.1.

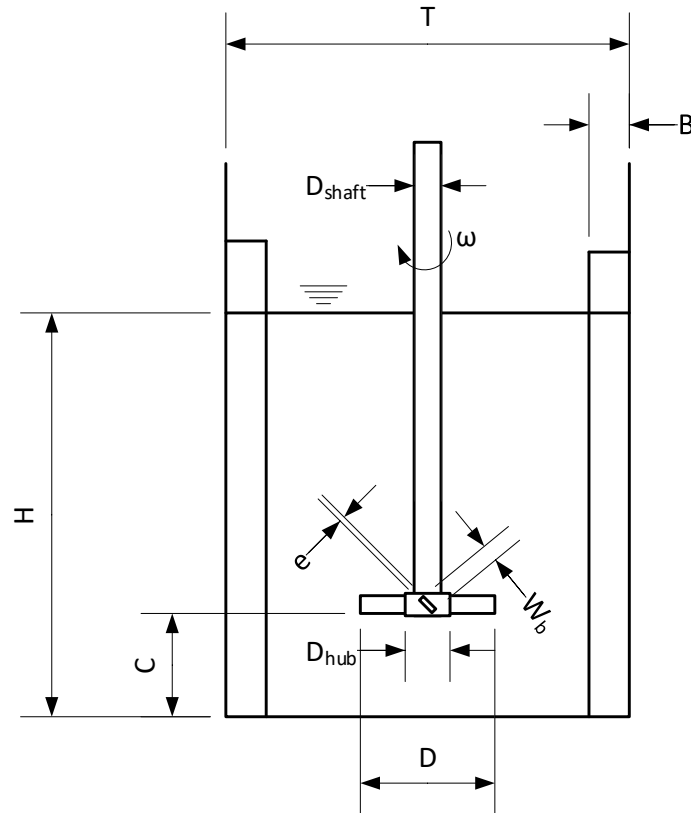


Figure 4.1: Geometry used in the Blais case study.

Table 4.1: Dimensions used in the Blais case study.

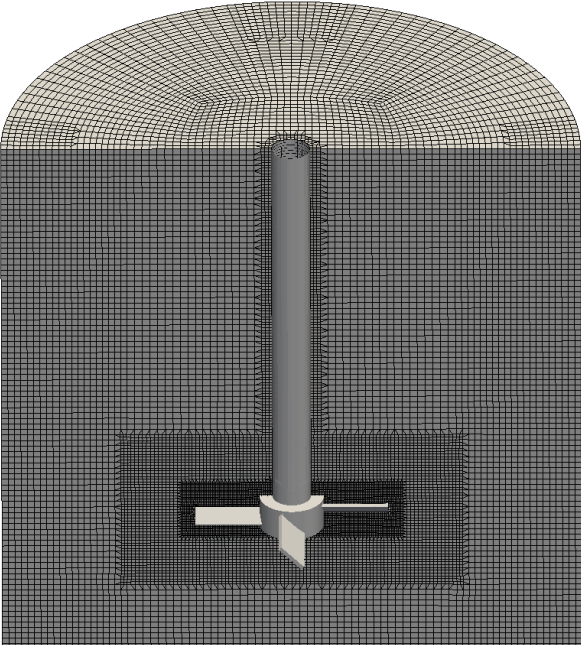
Name and Symbol	Dimension (m)
Tank diameter, T	0.365
Impeller diameter, $D = T/3$	0.12167
Liquid level, $H = T$	0.365
Off-bottom clearance, $C = T/4$	0.09125
Baffle width, $B = T/10$	0.0365
Blade width, $W_b = D/5$	0.0243
Shaft diameter, D_{shaft}	0.0243
Hub diameter, D_{hub}	0.2231
Blade thickness, $e = W_b/10$	0.0024

4.2.2. Case Setup and Meshing

The tank and impeller geometries were modelled using the SALOME pre-processing platform (Salome Platform, n.d.). Meshing was performed using a combination of tools available in SALOME and OpenFOAM. A structured background mesh was created for the tank without the impeller using SALOME. Subsequently, the OpenFOAM utility `snappyHexMesh` was used to cut out and conform the mesh to the impeller, which results in a hexahedral-dominant unstructured mesh. As shown in Table 4.2, one level of local mesh refinement was added for the rotating zone and around the impeller shaft using the mesh cell splitting technique available in `snappyHexMesh`. Two local levels of mesh refinement were applied in the vicinity of the impeller. No mesh dependence study was completed for this case, but the mesh resolution was specified to be close to the recommendation of Blais et al. (2016). This mesh resolution is also similar to the resolution used for the pitched blade impeller case study detailed in section 4.3, for which a mesh dependence study is provided.

The size of the rotating zone is somewhat arbitrary, but its dimensions should not impact the results. In this case, the size of rotating domain was chosen such that its boundary is halfway between the impeller tip and the baffles in the radial direction and two blade widths above and below in the axial direction. This resulted in a diameter of 0.207 m and a height of 0.0972 m for the zone. For MRF simulations, the rotating zone was defined as a `cellZone`, and an appropriate volumetric force was applied to represent the rotation of the impeller. For sliding mesh simulations, the computational grid was split into two regions, one for the rotating impeller and the other for the stationary domain. This splitting allows application of a cyclic arbitrary mesh interface (AMI) boundary condition to couple the mesh interface between rotating and stationary zones. The splitting was done by using the OpenFOAM utility `topoSet` to select the faces on the boundary. The `createBaffles` and `mergeOrSplitBaffles` utilities were then used to create the AMI boundary. The OpenFOAM utilities `topoSet` and `createBaffles` were used to add four infinitely-thin baffles. Baffle thickness was not considered to minimize complexity of the mesh. This approach is commonly used in the literature and should not significantly impact the results (Gao et al., 2016; Li et al., 2017; Coroneo et al., 2011).

Table 4.2: Computational mesh used in the Blais pitched blade impeller case study.

Blais PBT Case	
Mesh	
Number of 3D cells	1 153 998
Number of 3D hexahedral cells	1 125 311
Maximum aspect ratio	3.17
Average non-orthogonality	7.88
Maximum skewness	1.68
Minimum cell volume	$2.50 \times 10^{-10} \text{ m}^3$
Maximum cell volume	$1.67 \times 10^{-7} \text{ m}^3$
Total volume	0.0380203 m^3
Rotating zone diameter	0.207 m
Rotating zone height	0.097 m

Boundary conditions that were applied to each case are summarized in Table 4.3. The “Walls” column refers to all tank wall boundaries including baffles and side walls of the tank. The impeller is located at the center of the cylindrical rotating zone. For sliding mesh simulations, the cyclic AMI boundary condition is used to couple mesh interface between rotating and stationary zones. Figure 4.2 provides a visual description of the boundary conditions that were applied. Turbulence variables k and ε were modelled using the standard scalable wall functions `kLowReWallFunction` and `epsilonWallFunction`.

Table 4.3: Boundary conditions used in Blais stirred tank validation cases.

Variable	Shaft	Impeller	Walls	Top
Velocity, U (m/s)	rotatingWall Velocity	movingWall Velocity	noSlip	slip
Pressure, p (Pa)	zeroGradient	zeroGradient	zeroGradient	zeroGradient
Turbulent kinematic viscosity, ν_t (m ² /s)	nutkWall Function	nutkWall Function	nutkWall Function	calculated
Turbulent kinetic energy, k (m ² /s)	kLowReWall Function	kLowReWall Function	kLowReWall Function	zeroGradient
Turbulent energy dissipation rate, ε (m ² /s ³)	epsilonWall Function	epsilonWall Function	epsilonWall Function	zeroGradient

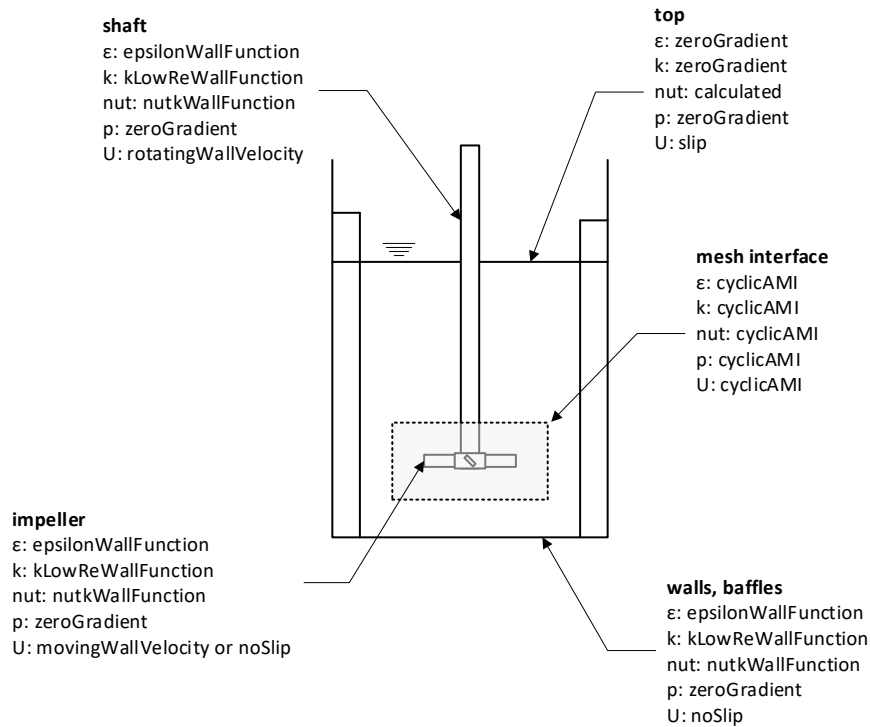


Figure 4.2: Visual description of boundary conditions and mesh interface between rotating and stationary domains. The size of rotating domain was chosen such that its boundary is halfway between the impeller tip in the radial direction and two blade widths above and below in the axial direction.

Table 4.4 summarizes the fluid properties that were used for the case study. The initial conditions used for the Blais stirred tank simulations are summarized in Table 4.5.

Table 4.4: Fluid properties used in the Blais case study.

Property	Value
Density, ρ (kg/m ³)	1520
Dynamic viscosity, μ (Pa s)	0.5
Kinematic viscosity, $\nu = \mu/\rho$ (m ² /s)	3.29×10^{-6}

Table 4.5: Initial conditions used in the Blais case study.

Reynolds number, $(\rho ND^2/\mu)$	Impeller speed, N (1/s)	Turbulent kinematic viscosity, ν_t (m ² /s)	Turbulent kinetic energy, k (m ² /s)	Turbulent energy dissipation rate, ε (m ² /s ³)
*0.75	0.0167	-	-	-
*1.5	0.0333	-	-	-
*3.8	0.0844	-	-	-
*7.5	0.1667	-	-	-
*19	0.4222	-	-	-
*38	0.8444	-	-	-
*75	1.6667	-	-	-
*113	2.5111	-	-	-
*150	3.3333	-	-	-
*188	4.1777	-	-	-
*225	5.0000	1.0×10^{-11}	3.62×10^{-3}	2.36×10^{-2}
1 600	35.555	1.0×10^{-11}	1.12×10^{-1}	4.07×10^0
12 500	277.76	1.0×10^{-11}	4.09×10^0	8.98×10^2

*Simulations for Reynolds numbers below 225 were completed without a turbulence model.

4.3. Chapple Case

Chapple et al. (2002) measured torque over a range of Reynolds numbers using radial flow Rushton turbines with different blade thicknesses and an axial flow PBTD. Chapple et al. (2002) presents local fluid velocity data obtained using laser Doppler velocimetry (LDV) and computational fluid dynamics (CFD). In the present work, CFD simulations were performed using the pseudo-steady-state MRF technique and the k - ε model was used for turbulence modelling. These simulations were used to provide further validation of the modelling techniques for a broader range of tank and impeller geometries.

4.3.1. Geometry

Three validation cases from Chapple et al. (2002) were used to test solver hydrodynamics predictions. The first case involved variation of power number with Reynolds number for

a downward pumping four bladed 45° pitched blade impeller. This case was considered to verify model predictions for the transitional and fully turbulent range of Reynolds numbers. Furthermore, Chapple et al. (2002) give velocity profile data at the blade tip for this impeller geometry, which was compared with local velocity predictions. The second and third validation cases investigate sensitivity of power number predictions to changes in blade thickness for a Rushton turbine. All experiments performed by Chapple et al. (2002) used a 0.240 m diameter tank ($T = 0.240$ m). The geometric configurations are shown in Figure 4.3 and important dimensions are summarized in Table 4.6.

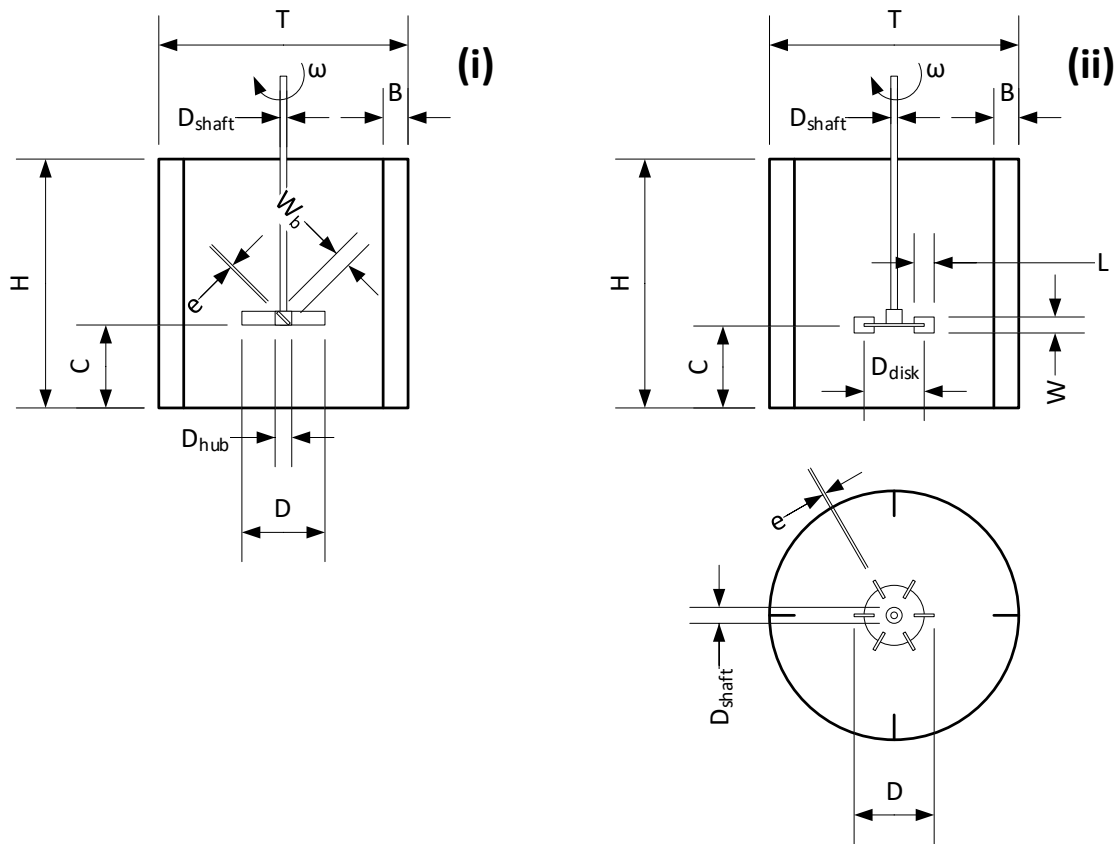


Figure 4.3: Geometries used in the Chapple case study: (i) side view of the pitched blade impeller case, (ii) side and top views of Rushton turbine cases where impeller blade thickness was varied ($e = 0.00089$ m and 0.00259 m).

Table 4.6: Dimensions for the pitched blade impeller and Rushton turbine Chapple case study.

Name and Symbol	PBT (m)	RT (m)	RT (m)
Tank diameter, T	0.240	0.240	0.240
Impeller diameter, $D = T/3$	0.00795	0.0808	0.0771
Liquid level, $H = T$	0.240	0.240	0.240
Off-bottom clearance, $C = T/3$	0.080	0.080	0.080
Baffle width, $B = T/10$	0.0240	0.024	0.024
Blade width, W_b	0.0159	0.0162	0.0154
Hub diameter, D_{hub}	0.0159	0.0128	0.0154
Hub height, H_{hub}	0.0121	0.0143	0.0150
Shaft diameter, D_{shaft}	0.0064	0.0064	0.0064
Blade thickness, e	0.00272	0.00089	0.00259
Blade length, L	-	0.0201	0.0193
Disk diameter, D_{disk}	-	0.0536	0.0579
Disk thickness	-	0.00142	0.00262

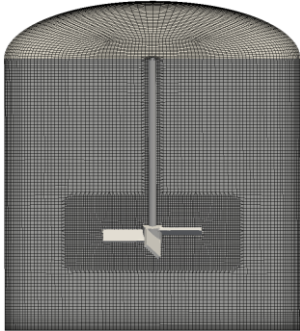
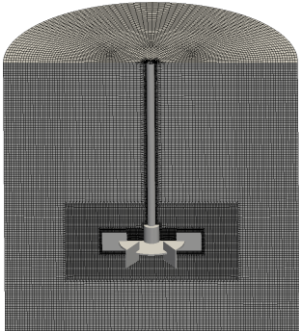
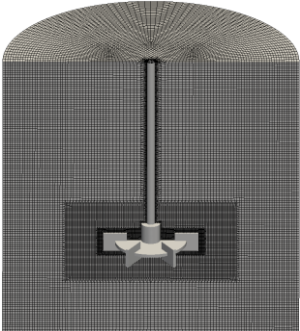
4.3.2. Case Setup and Meshing

The tank and impeller geometries were modelled using the SALOME pre-processing platform (Salome Platform, n.d.). Meshing was performed using a combination of tools available in SALOME and OpenFOAM. A structured background mesh was created for the tank without the impeller using SALOME. Subsequently, the OpenFOAM utility snappyHexMesh was used to cut out and conform the mesh to the impeller, which results in a hexahedral-dominant unstructured mesh. As shown in Table 4.7, for the PBT case, one level of local mesh refinement was added for the rotating zone and around the impeller and impeller shaft using the mesh cell splitting technique available in snappyHexMesh. Conversely, for the RT cases, one level of local mesh refinement was added for the rotating zone and two local levels of mesh refinement were applied around the impeller and impeller shaft. For the two Rushton turbine cases considered, two refinement levels were used in order to better resolve the blades and ensure consistency between cases. Figure 4.4 shows the generated meshes for both impellers.

As for the Blais case described in section 4.2, the size of the rotating zone is somewhat arbitrary, but its dimensions should not impact the results. The size of rotating domain was chosen such that its boundary is halfway between the impeller tip and the baffles in the radial direction and two blade widths above and below in the axial direction. This resulted

in a diameter of 0.136 m and a height of 0.064 m for the zone. Only MRF simulations were performed for the Chapple cases. The rotating zone was therefore defined as a cellZone, and an appropriate volumetric force was applied to represent the rotation of the impeller. The OpenFOAM utilities topoSet and createBaffles were used to add four infinitely-thin baffles. Baffle thickness was not considered to minimize complexity of the mesh. This approach is commonly used in the literature and should not significantly impact the results.

Table 4.7: Computational meshes used in the Chapple pitched blade impeller and Ruston turbine cases.

	*Chapple PBT	Chapple 0.89 mm	Chapple 2.59 mm
Mesh			
Number of 3D cells	1 357 144	2 412 516	2 367 102
Number of 3D hexahedral cells	1 342 994	2 372 682	2 326 774
Maximum aspect ratio	14.9	3.62	5.53
Average non-orthogonality	5.73	9.09	8.98
Maximum skewness	2.65	3.35	2.60
Minimum cell volume	$2.86 \times 10^{-10} \text{ m}^3$	$2.59 \times 10^{-11} \text{ m}^3$	$3.22 \times 10^{-11} \text{ m}^3$
Maximum cell volume	$2.38 \times 10^{-8} \text{ m}^3$	$2.09 \times 10^{-8} \text{ m}^3$	$2.08 \times 10^{-8} \text{ m}^3$
Total volume	$1.08 \times 10^{-2} \text{ m}^3$	$1.08 \times 10^{-2} \text{ m}^3$	$1.08 \times 10^{-2} \text{ m}^3$
Rotating zone diameter	0.136 m	0.136 m	0.136 m
Rotating zone height	0.060 m	0.064 m	0.065 m

*This Chapple PBT case is also referred to as “Mid Mesh” in this work.

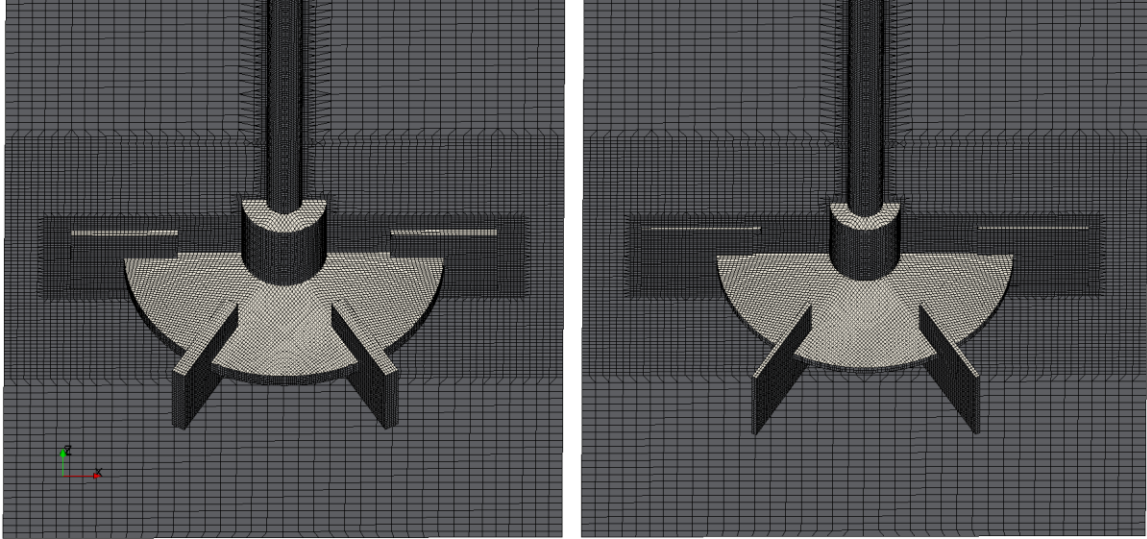
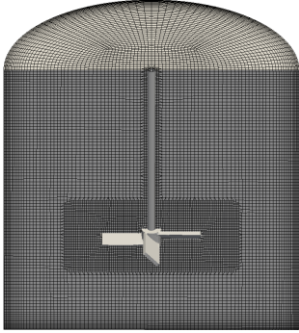
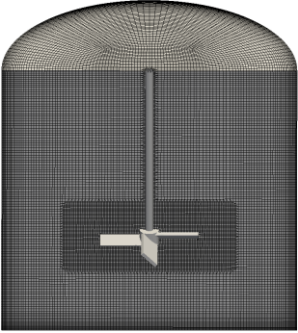
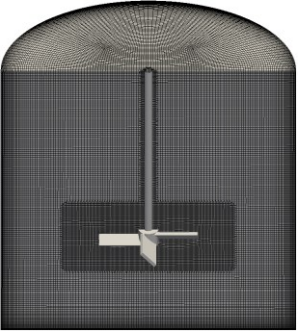


Figure 4.4: Meshes used in the Chapple Rushton turbine cases showing $e/D = 0.034$ (left) and $e/D = 0.011$ (right).


A mesh dependence study was completed for the PBT case. No mesh dependence study was completed for the RT cases. However, a mesh dependence study was completed for a similar RT case in section 5.3, and a similar mesh resolution was used for the studies in this section. The three computational meshes considered for the PBT mesh dependence study are summarized in Table 4.8. The meshes were generated by building a background mesh of 842 520 cells for the Mid Mesh, a background mesh having 25% less for the Coarse Mesh, and a background mesh having 25% more cells for the Fine Mesh. The one level of local refinement in the rotating zone was applied by cell splitting of the background mesh.

Table 4.8: Mesh dependence study for the Chapple case using pitched blade turbine.

	Coarse Mesh	Mid Mesh	Fine Mesh
Mesh			
Number of 3D cells	728 152	1 357 144	2 458 868
Number of 3D hexahedral cells	719 222	1 342 994	2 438 952
Maximum aspect ratio	14.8	14.9	14.8
Average non-orthogonality	5.95	5.73	5.60
Maximum skewness	3.00	2.65	2.89
Minimum cell volume	$5.78 \times 10^{-10} \text{ m}^3$	$2.86 \times 10^{-10} \text{ m}^3$	$1.85 \times 10^{-10} \text{ m}^3$
Maximum cell volume	$4.54 \times 10^{-8} \text{ m}^3$	$2.38 \times 10^{-8} \text{ m}^3$	$1.28 \times 10^{-8} \text{ m}^3$
Total volume	$1.08 \times 10^{-2} \text{ m}^3$	$1.08 \times 10^{-2} \text{ m}^3$	$1.08 \times 10^{-2} \text{ m}^3$
Rotating zone diameter	0.136 m	0.136 m	0.136 m
Rotating zone height	0.060 m	0.060 m	0.060 m

In addition to the meshes summarized in Table 4.8, an additional very fine grid was included in the mesh independence study. The Very Fine Mesh is summarized in Table 4.9. This mesh was generated by building a background mesh of 842 520 cells and applying one level of global refinement to the full domain by cell splitting of the background mesh. One level of local surface refinement along the impeller was applied by extruding outward 0.010 m as shown in Table 4.9.

Table 4.9: Mesh dependence study for Very Fine Mesh Chapple case using pitched blade turbine.

Very Fine Mesh	
Mesh	
Number of 3D cells	13 851 818
Number of 3D hexahedral cells	13 629 974
Maximum aspect ratio	13.8
Average non-orthogonality	4.10
Maximum skewness	3.89
Minimum cell volume	$1.45 \times 10^{-11} \text{ m}^3$
Maximum cell volume	$1.61 \times 10^{-9} \text{ m}^3$
Total volume	$1.08 \times 10^{-2} \text{ m}^3$
Rotating zone diameter	0.136 m
Rotating zone height	0.060 m

The fluid properties used in the Chapple case studies are summarized in Table 4.10. The initial conditions for the Chapple Rushton turbine case studies are summarized in Table 4.11 and the initial conditions used in the Chapple PBT case studies are listed in Table 4.12. The initial velocity and pressure fields were set to 0.

Table 4.10: Fluid properties used in the Chapple cases.

Property	Value
Density, ρ (kg/m ³)	998.2
Dynamic viscosity, μ (Pa s)	1×10^{-3}
Kinematic viscosity, $\nu = \mu/\rho$ (m ² /s)	1×10^{-6}

Table 4.11: Initial conditions used in the Chapple Rushton turbine cases.

Reynolds number, $(\rho ND^2/\mu)$	Impeller speed, N (1/s)	Turbulent kinematic viscosity, ν_t (m^2/s)	Turbulent kinetic energy, k (m^2/s^2)	Turbulent energy dissipation, ε (m^2/s^3)
300	0.046	1.0×10^{-11}	1.26×10^{-6}	7.27×10^{-9}
2 000	0.306	1.0×10^{-11}	3.47×10^{-5}	1.06×10^{-6}
9 000	1.379	1.0×10^{-11}	4.83×10^{-4}	5.48×10^{-5}
30 000	4.595	1.0×10^{-11}	3.97×10^{-3}	1.29×10^{-3}
90 000	13.785	1.0×10^{-11}	2.71×10^{-2}	2.31×10^{-2}

Table 4.12: Initial conditions used in the Chapple pitched blade turbine cases.

Reynolds number, $(\rho ND^2/\mu)$	Impeller speed, N (1/s)	Turbulent kinematic viscosity, ν_t (m^2/s)	Turbulent kinetic energy, k (m^2/s^2)	Turbulent energy dissipation, ε (m^2/s^3)
1 000	0.15625	1.0×10^{-11}	1.05×10^{-5}	1.79×10^{-7}
4 000	0.625	1.0×10^{-11}	1.19×10^{-4}	6.79×10^{-6}
20 000	3.125	1.0×10^{-11}	1.99×10^{-3}	4.64×10^{-4}
60 000	9.375	1.0×10^{-11}	1.36×10^{-2}	8.30×10^{-3}
100 000	15.625	1.0×10^{-11}	3.33×10^{-2}	3.17×10^{-2}

4.4. Results and Discussion

The MRF simulation results presented in this section were performed using the steady-state incompressible flow solver simpleFoam with the k - ε turbulence model, as described in Chapter 3. The sliding mesh simulations were performed using the transient incompressible flow solver pimpleFoam with the k - ε turbulence model. As previously described, a mesh dependence study was performed for the pitched blade impeller case of Chapple et al. (2002). A further mesh dependence study for a Rushton turbine impeller is provided in section 5.3. Simulations were performed for a range of tank geometries, impeller geometries, and flow regimes to develop an understanding of these changes on hydrodynamic predictions and mixing power. Additionally, both transient sliding mesh simulations and pseudo-stead-state MRF simulations were conducted to validate the accuracy of the MRF approach. Furthermore, MRF simulations were performed for different baffle locations relative to the impeller to assess changes in power number predictions.

4.4.1. Mesh Refinement Study

A mesh dependence study was performed for the four meshes described in Table 4.8 and Table 4.9 for the pitched blade turbine impeller case of Chapple et al. (2002). Two stirring speeds were tested to analyze the interaction between stirring speed and mesh resolution on the predictions. Figure 4.5 shows the predicted power number varying with the number of mesh cells. The power number trends obtained for both high and low Reynolds numbers are similar. The torque-based power number predictions tend to show better agreement with the experimental data than energy dissipation rate based values. Although the torque-based power numbers tend to stay relatively constant at increasing mesh resolution, there is some deviation between meshes. Energy dissipation rate based power numbers underpredict the experimental results for both Reynolds numbers and follow a similar increasing trend with increased grid size. It is well known in the literature that energy dissipation rate based power numbers tend to underpredict experimental results except at very high mesh resolutions (Gao et al., 2016; Maluta et al., 2021; Rave et al., 2021; Singh et al., 2011) and that they show greater underpredictions at low Reynolds numbers due to limitations of the turbulence modelling approach.

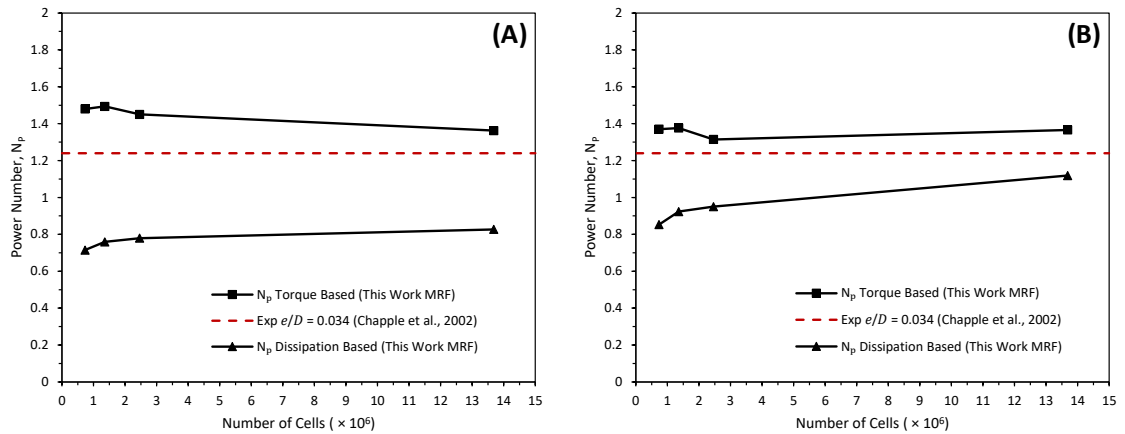


Figure 4.5: Effect of the number of computational mesh cells on predicted power number with $Re = 1\ 000$ (A) and $Re = 60\ 000$ (B).

The spatial distribution of turbulent energy dissipation rate affects micromixing rates and therefore partially controls predicted reaction rates for mixing-limited reactions. Thus, the distribution of turbulent energy dissipation rate was plotted for the Coarse Mesh (length

scale 0.0025 m), Mid Mesh (length scale 0.0020 m), Fine Mesh (length scale 0.0016 m), and Very Fine Mesh (0.0009 m) simulations. These distributions are shown below in Figure 4.7. Similar to the trend observed for the energy dissipation rate based power number in Figure 4.5, the Mid Mesh, Fine Mesh, and Very Fine Mesh provide similar predictions in distribution shape and average value, with differences observed for the Coarse Mesh in Figure 4.6(A). This suggests that the Mid Mesh, Fine Mesh, and Very Fine Mesh should provide relatively similar mixing predictions for mixing-limited reaction simulations. It also suggests that the Mid Mesh is sufficiently resolved to provide converged power number predictions. Therefore, although there are observed minor mesh dependent effects, further pitched blade impeller simulations will use mesh resolutions similar to the Mid Mesh.

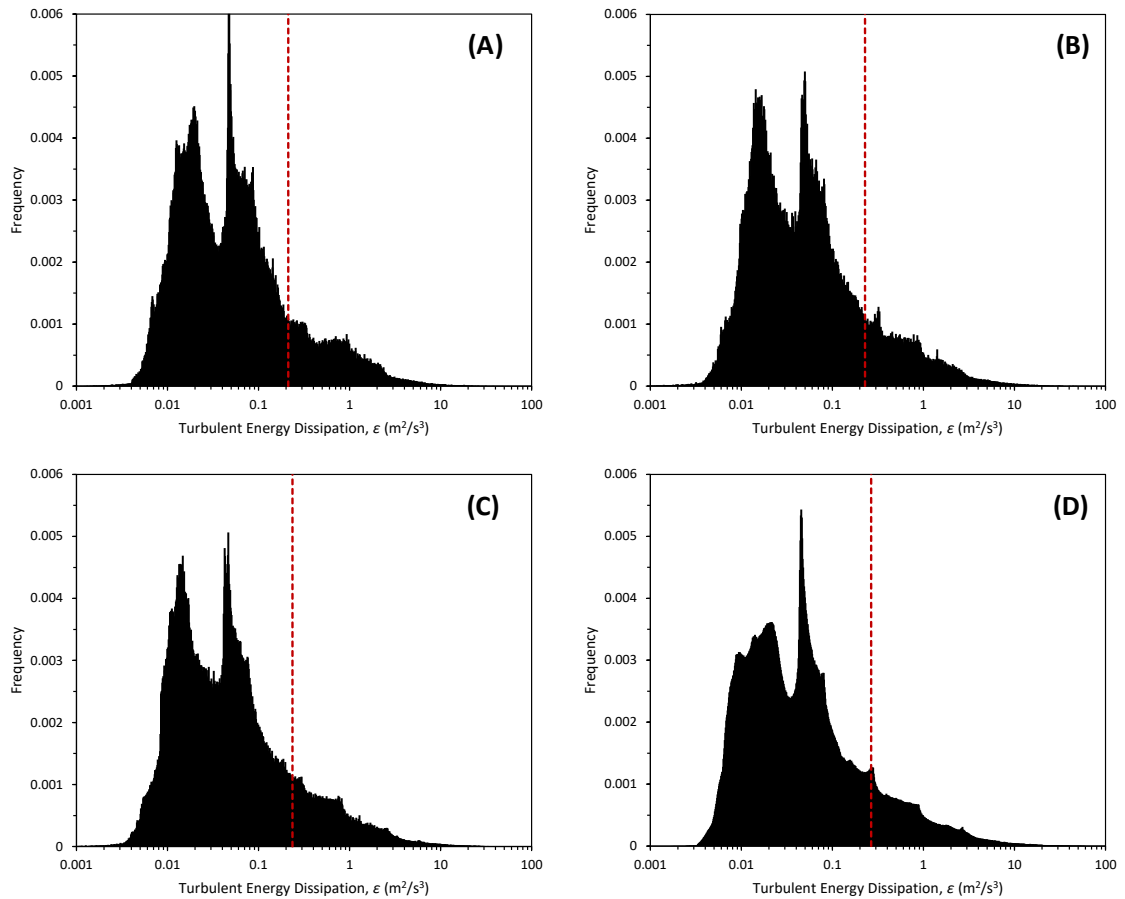


Figure 4.6: Distributions of turbulent energy dissipation rate in the Chapple pitched blade impeller case at Reynolds number of 60 000. Mesh length scale of 0.0025 m (A), 0.002 m (B), 0.0016 m (C), and 0.0009 m (D).

The axial and radial velocity profiles 2 mm above the blade tip for the Coarse Mesh, Mid Mesh, Fine Mesh, and Very Fine Mesh simulations are shown in Figure 4.7. All meshes predict similar results. The axial velocity is underpredicted compared to experimental data at the blade tip, where the velocity is the highest. However, overall the predicted profiles match the measurements closely. In the experiments of Chapple et al. (2002), the velocity profiles were measured using LDV. However, the authors did not state the accuracy of the velocity profile measurements or the Reynolds number for which these data were obtained. Plots were therefore created using Reynolds numbers of 60 000 and 100 000 to confirm that the results are relatively independent of Reynolds number.

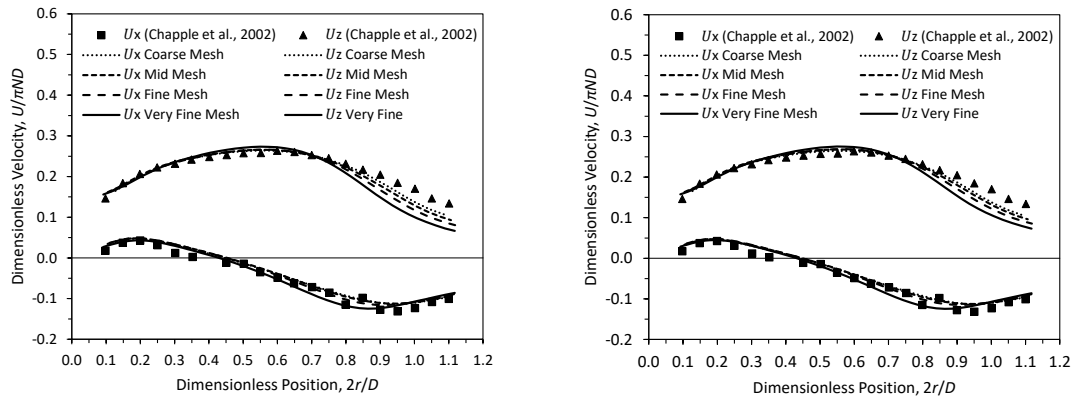


Figure 4.7: Effect of computational mesh on predicted velocity profiles with $Re = 60\,000$ (left) and predicted velocity profiles for $Re = 100\,000$ (right).

4.4.2. Relative Baffle Position

The MRF technique uses a fixed position of the impeller and applies a source term within the impeller region to effectively rotate the fluid around the impeller. When simulating a baffled tank, it is therefore necessary to select an impeller orientation relative to the baffles. The assumed orientations relative to the baffles are illustrated for each case in the presented schematic drawings. However, simulations were performed for the Chapple PBT case with various angles between the baffles and impeller blades to ensure that the results are relatively insensitive to this orientation. The results presented in Figure 4.8 and Figure 4.9 confirm that both the power number and velocity profile predictions are not sensitive to the orientation of the impeller relative to the baffles.

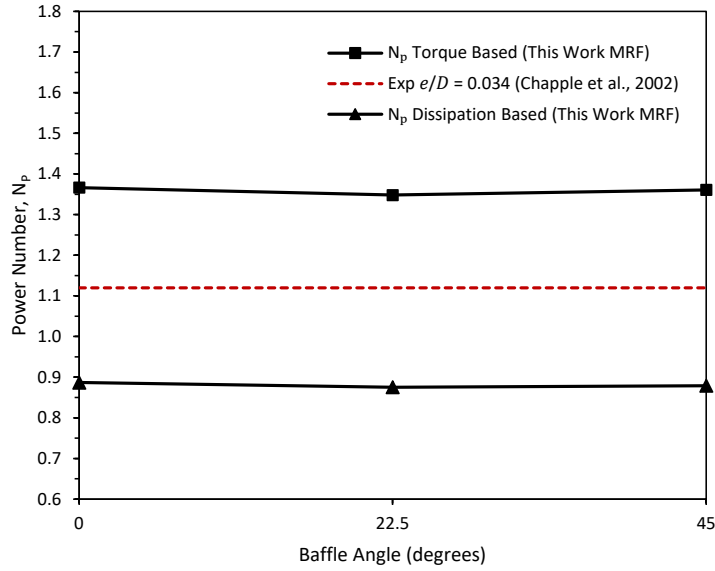


Figure 4.8: Effect of the baffle position relative to impeller on predicted power number for the Chapple PBT case with $Re = 4\,000$.

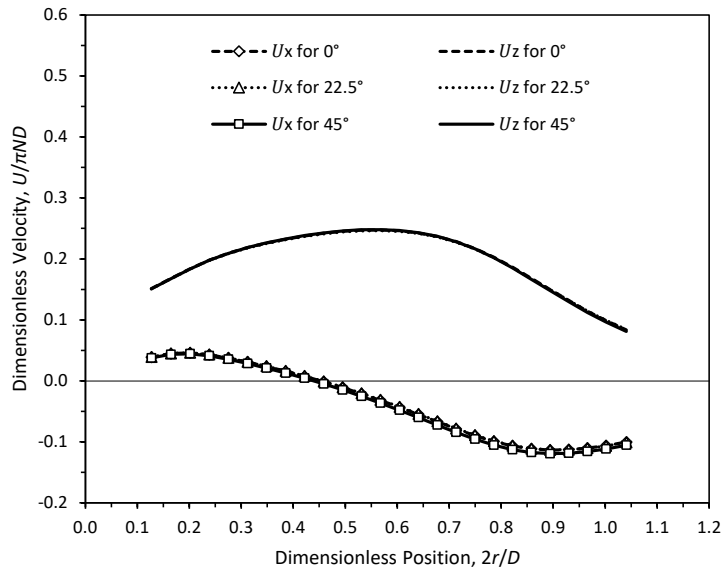


Figure 4.9: Effect of baffle position on predicted velocity profiles for the Chapple PBT case with $Re = 4\,000$.

4.4.3. Power Number Predictions

Power number varying with respect to Reynolds number is given in Figure 4.10 for the Blais case. Below a Reynolds number of 112, the simulation results are in good agreement

with experimental and simulation data from Blais et al. (2016). Under conditions of fully laminar flow, power number is expected to decrease directly proportional to Reynolds number (i.e., $N_p = -1/Re$). This was used as an additional check by fitting a power law equation to the simulation results for power number values at Reynolds numbers below 10. The regression resulted in a slope of -0.974 and $R^2 = 0.9999$, which confirms appropriate predictions at low Re.

Two strategies for handling the impeller motion were used to study the impact on power number prediction. The multiple reference frame technique (MRF) is limited to steady-state simulations due to the steady flow assumption at the rotating-stationary interface (Luo et al., 1994). Figure 4.10 shows good agreement between power number predictions made using both MRF and sliding mesh simulations in both laminar and turbulent flow regimes. The sliding mesh technique was found to increase computation time by approximately 10 times relative to the time required for MRF simulations. Therefore, the MRF technique was chosen for the remaining flow and reactive mixing simulations. Simulation results for the MRF and sliding mesh show some deviation from the Blais et al. (2016) experimental and simulation data for Reynolds numbers between 112 and 300. However, these differences are relatively small.

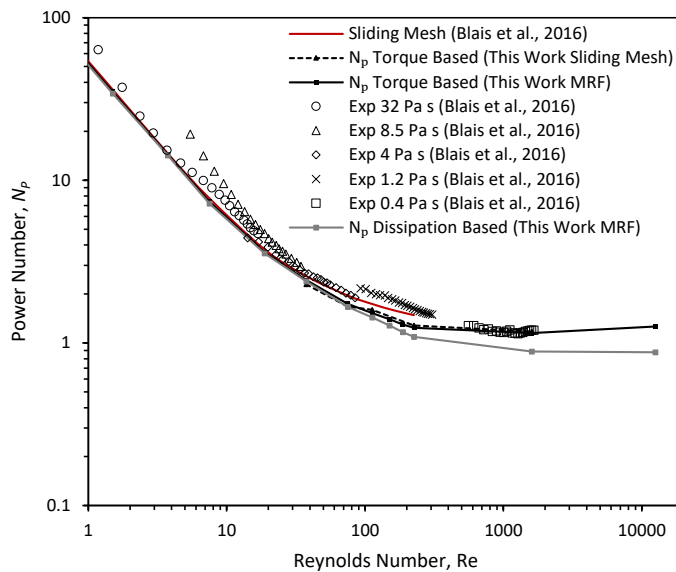


Figure 4.10: Power number curve for the pitched blade turbine Blais case.

In addition to the range of data provided by Blais et al. (2016), Figure 4.10 also shows results of power number predictions in a more turbulent flow regime at $Re = 12\,500$. For a similar four bladed pitched blade impeller, following grid independence test procedure by Coroneo et al. (2005), Duan et al. (2019) evaluated predicted power number in two ways: surface integration of pressure forces along the impeller ($N_{P,M}$) and volume integration of the turbulent energy dissipation rate ($N_{P,\varepsilon}$). Paul et al. (2004) suggest a rule-of-thumb that the ratio of power numbers should be around 0.90 for high mesh quality. In this work, predictions at $Re = 12\,500$ resulted in $N_{P,M} = 1.26$ and $N_{P,\varepsilon} = 0.88$, which gives a ratio of $N_{P,\varepsilon}/N_{P,M} = 0.70$. For all computational meshes reported by Duan et al. (2019), this ratio was 0.43–0.58. These results are summarized in Table 4.13.

Table 4.13: Ratio of power number predictions determined by impeller torque or volume integration of the turbulent energy dissipation rate.

Reynolds number, $(\rho ND^2/\mu)$	Length scale (m)	$N_{P,M}$	$N_{P,\varepsilon}$	$N_{P,\varepsilon}/N_{P,M}$	Case
12 500	6.91×10^{-3}	1.26	0.88	0.70	Blais (this work)
12 500	1.38×10^{-3}	0.43	0.18	0.42	Duan et al. (2019)
12 500	1.07×10^{-3}	0.49	0.26	0.53	Duan et al. (2019)
12 500	8.97×10^{-4}	0.50	0.27	0.54	Duan et al. (2019)
12 500	8.25×10^{-4}	0.50	0.28	0.56	Duan et al. (2019)

The grid independence procedure proposed by Coroneo et al. (2005) is well suited for turbulent flow simulations due to the direct volume integration of the turbulent energy dissipation rate that is subsequently used to evaluate power number ($N_{P,\varepsilon}$). In this work, the approach of Coroneo et al. (2005) is modified to laminar flow for qualitatively assessing mesh quality by integration of the viscous dissipation rate outlined in Eq. (3.18). In this work, predictions ranging from $Re = 0.75$ –300 result in a $N_{P,\varepsilon}/N_{P,M}$ ratio of 0.97–0.88.

Figure 4.11 shows a comparison of power number predictions with experimental data from Chapple et al. (2002) for the four bladed pitched blade turbine impeller. Based on the mesh dependence study, simulations used the Mid Mesh. Power number predictions follow similar trends to experimental data. The power number obtained from the energy dissipation rate underpredicts the experimental results for all Reynolds numbers.

Conversely, torque-based power number overpredicts the experimental data in the low Reynolds number range but shows but shows generally good agreement with the experimental results. Experiments from Chapple et al. (2002) used three working fluids of different viscosity and density to aid power number measurements over a range of flow conditions. Although the authors do not report experimental error for the data, power number measurements are expected to be most variable in the tail end for each working fluid. TriEthylene Glycol was used as the working fluid over the range of $Re = 1\,000$ – $4\,000$.

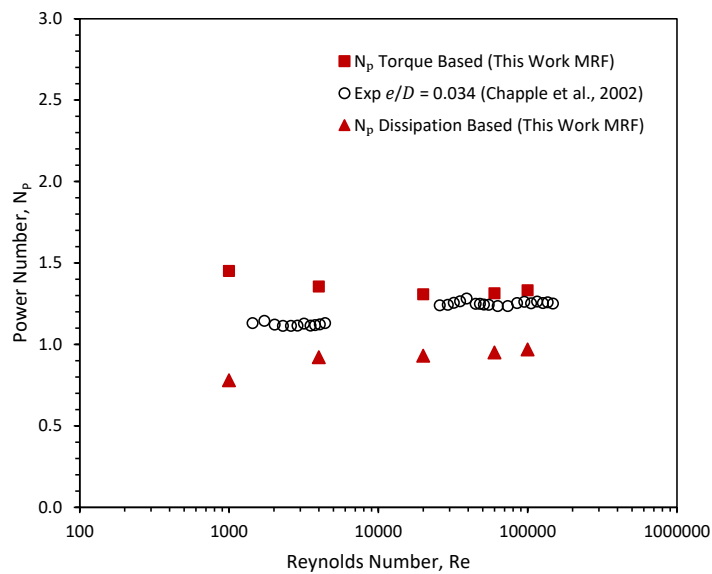


Figure 4.11: Comparison of power number predictions with experimental data from Chapple et al. (2002) for a pitched bladed turbine impeller. Simulations were performed using the Mid Mesh.

Figure 4.12 shows a comparison of power number predictions for two impeller blade thicknesses with experimental data from Chapple et al. (2002) for Rushton turbine impellers. The results indicate that simulations for both blade thickness agree well with the experimental data. As mentioned previously, the authors did not report estimates of experimental error for power number or impeller torque.

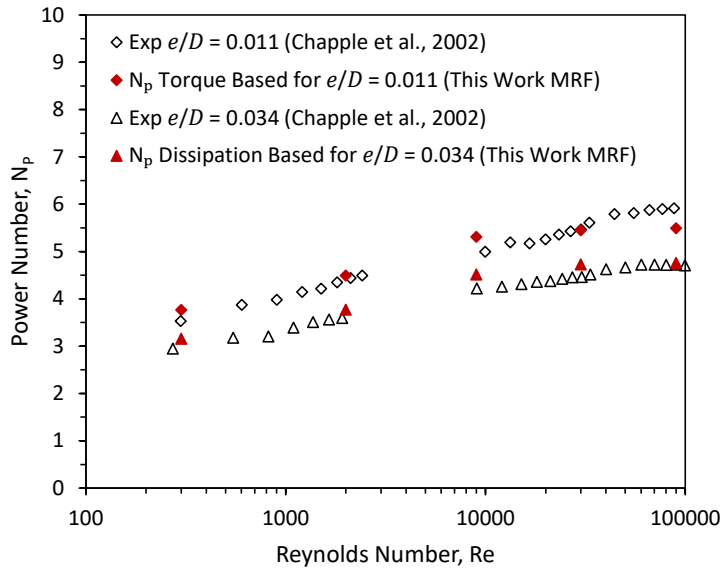


Figure 4.12: Power number curve for both Rushton turbine Chapple cases with varying blade thicknesses. Triangles: $e/D = 0.034$ (2.59 mm). Diamonds: $e/D = 0.011$ (0.89 mm).

4.5. Summary

The purpose of the validation cases presented in this chapter was to investigate hydrodynamic mixing power predictions of stirred tank reactors with various impeller geometries. The validation cases included power number measurements taken from literature investigations of Chapple et al. (2002) and Blais et al. (2016) and velocity profiles measurements from Chapple et al. (2002). The simulation results were used ensure accuracy of the MRF approach relative to the more rigorous but computationally demanding sliding mesh approach. The MRF approach was determined to be sufficiently accurate for both power number and velocity profile predictions for the types of geometries and flow regimes considered in this work. The case studies were also used to validate meshing procedures and to identify appropriate mesh resolutions.

CHAPTER 5: VALIDATION OF THE REACTIVE MIXING SOLVER

5.1. Introduction

The purpose of this chapter is to investigate and validate the modelling approach used for simulating reactive mixing. Validation cases include a confined impinging-jet reactor (CIJR) because the same model has often been used for these systems and it is relatively simple as well as stirred tank reactors for which experimental data was available in the literature. The selected CIJR validation case is based on experimental studies of Johnson and Prud'homme (2003), and the stirred tank cases are from Akiti and Armenante (2004) and Assirelli et al. (2002). For comparison, experimental results from Johnson and Prud'homme (2003) fourth Bourne reaction experiments in a continuous flow CIJR are presented alongside simulation data from Liu and Fox (2006). Villermaux-Dushman segregation index measurements performed in a stirred tank reactor by Assirelli et al. (2002) is selected to compare simulation predictions. Third Bourne reaction conversion measurements in a stirred tank reactor are from Akiti and Armenante (2004). The selected stirred tank reactor validation cases are convenient comparisons due to available simulation studies by Duan et al. (2016). The goal of these validation case studies is to verify accurate estimates of reaction yield in mixing sensitive reactions over various reactor types and flow conditions. In Chapter 6, the implemented model is used to provide a comparison between results from Villermaux-Dushman experiments performed in this work.

5.2. Liu and Fox Case

Liu and Fox (2006) simulated a CIJR based on experimental data of Johnson and Prud'homme (2003). The modelling approach is based on solving the two-environment DQMOM model coupled with an IEM model to account for sub-grid scale mass transport. The purpose of including this case in the present work is to validate reaction conversion predictions of mixing sensitive competitive-parallel reactions in a continuous flow setup. The reaction scheme implemented is the commonly used fourth Bourne reaction proposed by Baldyga et al. (1998), which consists of an infinitely fast reaction (3.IV) coupled with a second finite-rate reaction (3.V).

5.2.1. Geometry

A sketch of the geometry for the Liu and Fox (2006) case is summarized in Figure 5.1. The geometry used in this work is the same as the one used by Liu and Fox (2006) and Johnson and Prud'homme (2003). The diameter of the impinging jets is 0.5 mm ($d = 0.5$ mm) and the chamber diameter is 2.38 mm ($D/d = 4.76$). Chamber height is 1.904 mm ($H = 0.8D$), chamber length is 2.856 mm ($Z = 1.2D$), and the outlet diameter is 1 mm ($\delta = 2d$). The length of the impinging jets are 10 mm.

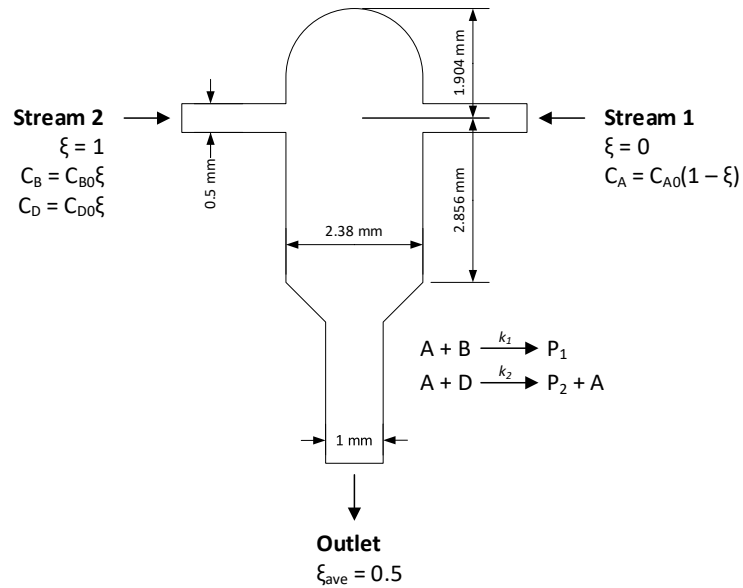


Figure 5.1: Geometry used for Liu and Fox (2006) confined impinging jet reactor case using the fourth Bourne reaction scheme.

5.2.2. Case Setup and Meshing

Four fully hexahedral cell 3D meshes were considered for this validation case to investigate the impact of model predictions on mesh refinement. The CIJR was modelled using SALOME pre-processing platform. Meshing was performed using a combination of tools available in SALOME and OpenFOAM. A structured background mesh was created for the CIJR chamber and outlet pipe. The chamber walls were then extruded in the direction of the impinging inlet jets. SnappyHexMesh was used to cut out and conform the mesh to the impinging jet surface mesh, which results in a fully hexahedral unstructured mesh. Table 5.1 summarizes the coarse, intermediate, and fine mesh used in this work. The very fine mesh is shown in Table 5.2.

Table 5.1: Meshes used for the Liu and Fox case.

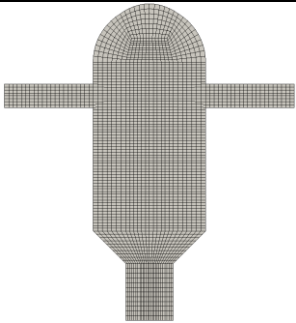
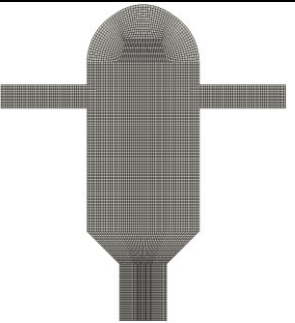
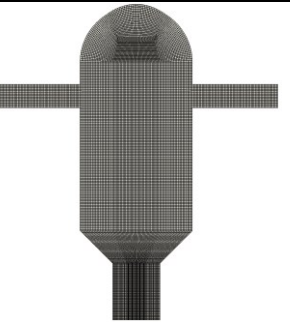
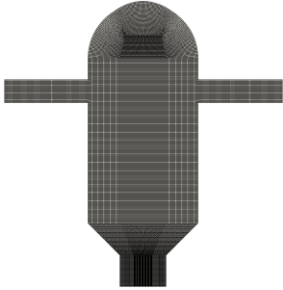
	Coarse Mesh	Mid Mesh	Fine Mesh
Mesh			
Number of 3D cells	102 618	743 374	1 741 894
Number of 3D hexahedral cells	102 618	743 374	1 741 894
Maximum aspect ratio	7.88	8.15	6.93
Average non-orthogonality	8.40	8.62	9.01
Maximum Skewness	3.61	3.13	2.75
Minimum cell volume	$4.20 \times 10^{-14} \text{ m}^3$	$5.00 \times 10^{-15} \text{ m}^3$	$2.13 \times 10^{-15} \text{ m}^3$
Maximum cell volume	$1.77 \times 10^{-12} \text{ m}^3$	$2.33 \times 10^{-13} \text{ m}^3$	$7.02 \times 10^{-14} \text{ m}^3$
Total Volume	$2.04 \times 10^{-8} \text{ m}^3$	$2.04 \times 10^{-8} \text{ m}^3$	$2.04 \times 10^{-8} \text{ m}^3$

Table 5.2: Very fine mesh used for the Liu and Fox case.

Very Fine Mesh	
Mesh	
Number of 3D cells	4 133 670
Number of 3D hexahedral cells	4 133 670
Maximum aspect ratio	6.93
Average non-orthogonality	9.00
Maximum Skewness	2.76
Minimum cell volume	$9.00 \times 10^{-16} \text{ m}^3$
Maximum cell volume	$2.96 \times 10^{-14} \text{ m}^3$
Total Volume	$2.04 \times 10^{-8} \text{ m}^3$

Fluid properties used in the Liu and Fox case studies are summarized in Table 5.6. The initial conditions for the Liu and Fox incompressible flow case are listed in Table 5.3 and the initial conditions for the Liu and Fox reactive mixing case studies are listed in Table 5.5. The initial velocity fields and pressure fields were set to 0. The inlet velocity patches were set to the fixed values summarized in Table 5.4. Standard low Reynolds number wall functions were used for k and ε . For each Reynolds number, two characteristic reaction times (i.e., inlet concentration) were simulated $t_r = 317 \text{ ms}$ ($C_{A0} = 4.69 \text{ mol/m}^3$, $C_{B0} = 4.92 \text{ mol/m}^3$, $C_{D0} = 4.69 \text{ mol/m}^3$) and $t_r = 181 \text{ ms}$ ($C_{A0} = 8.21 \text{ mol/m}^3$, $C_{B0} = 8.62 \text{ mol/m}^3$, $C_{D0} = 8.21 \text{ mol/m}^3$). The characteristic reaction times were evaluated using the expression $t_r = 1/(k_2 C_{A0})$. The initial mixture fraction and reaction progress variable fields were set to 0. The molar ratio of reagents is 1:1.05:1. Each simulation used a rate constant of $k_2 = 0.67313 \text{ mol/m}^3/\text{s}$.

Table 5.3: Boundary conditions used for the Liu and Fox steady-state flow cases.

Variable	Inlets	Outlet	Walls	Symmetry
Velocity, U (m/s)	fixedValue See Table 5.4	zeroGradient	noSlip	symmetry
Pressure, P (Pa)	zeroGradient	fixedValue = 0	zeroGradient	symmetry
Turbulent kinematic viscosity, ν_t (m ² /s)	calculated	calculated	nutkWall Function	symmetry
Turbulent kinetic energy, k (m ² /s)	fixedValue	zeroGradient	kLowReWall Function	symmetry
Turbulent energy dissipation, ε (m ² /s ³)	fixedValue	zeroGradient	epsilonWall Function	symmetry

Table 5.4: Summary of Conditions for the Simulated Cases from Liu and Fox

Jet Reynolds Number, $Re_j = \rho U d / \mu$	Inlet Velocity, U (m/s)
100	0.145
200	0.83
400	1.66
500	2.10
600	2.49
800	3.32
1 000	4.15
2 000	8.30

Table 5.5: Boundary conditions used for the Liu and Fox cases.

Variable	Inlet 1	Inlet 2	Walls	Outlet
Mixture fraction, α_1 (-)	fixedValue = 1	fixedValue = 0	zeroGradient	zeroGradient
Mixture fraction in environment 1, X_1 (-)	fixedValue = 0	fixedValue = 0	zeroGradient	zeroGradient
Mixture fraction in environment 2, X_2 (-)	fixedValue = 0	fixedValue = 1	zeroGradient	zeroGradient
Reaction progress in environment 1, Y_1 (-)	fixedValue = 0	fixedValue = 0	zeroGradient	zeroGradient
Reaction progress in environment 2, Y_2 (-)	fixedValue = 0	fixedValue = 0	zeroGradient	zeroGradient

Table 5.6: Liquid properties used for the Liu and Fox cases.

Property	Value
Density, ρ (kg/m ³)	962.5
Dynamic viscosity, μ (Pa s)	1.995×10^{-3}
Turbulent Schmidt number, Sc_t	0.7
*Molecular diffusion coefficient, D_T (m ² /s)	1.0×10^{-9}

*Assumed value negligible compared to turbulent diffusion.

5.3. Assirelli Case

The first stirred tank reactor validation case was based on experiments of Assirelli et al. (2002). Duan et al. (2016) used measured X_S data of Assirelli et al. (2002) to compare reactive mixing simulation predictions using a coupled CFD E-model approach. The purpose of this case was to validate the solver for batch systems by allowing for feed injections represented as additional source terms. This investigation studied power number and reaction yield predictions of the Villermaux-Dushman competitive-parallel reaction scheme for a stirred tank reactor. These case studies compare reaction yield predictions with experimental data and investigates the impact of mesh resolution.

5.3.1. Geometry

A sketch of the geometry for the Assirelli et al. (2002) experiments is shown in Figure 5.2. The stirred tank reactor had inner diameter of $T = 0.29$ m and height $H = 1.3T$ and was equipped with a standard six-blade Rushton turbine with diameter $D = T/3$. Table 5.7 gives a summary of dimensions used in this case. In the experiments, sulfuric acid H_2SO_4 was injected at a height H_F and radial distance r_F . The inner diameter of the injection feed pipe was 0.75–1 mm, where acid was injected at a volumetric flow rate of 2 mL/min. All the dimensions are summarized in Table 5.7.

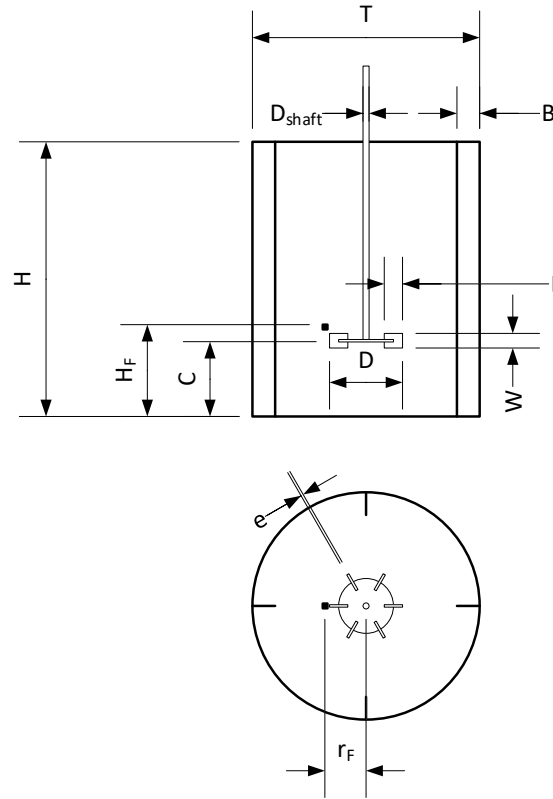


Figure 5.2: Geometry used for the Assirelli et al. (2002) stirred tank reactor simulations.

Table 5.7: Dimensions used in the Assirelli et al. Rushton turbine case.

Name and Symbol	Dimension (m)
Tank diameter, T	0.29
Impeller diameter, $D = T/3$	0.0967
Liquid level, $H = 1.3T$	0.377
Off-bottom clearance, $C = T/4$	0.0725
Baffle width, $B = T/10$	0.029
Blade width, $W_b = D/5$	0.0193
Blade length, $L = D/4$	0.0242
Shaft diameter, D_{shaft}	0.0193
Hub diameter, $D_{disk} = 3D/4$	0.0725
Blade thickness, $e = 0.034D$	0.0033
Radial feed position, r_F	0.0493
Axial feed position, H_F	0.08294

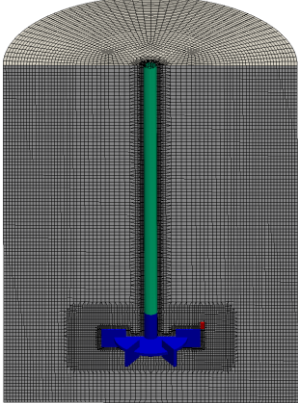
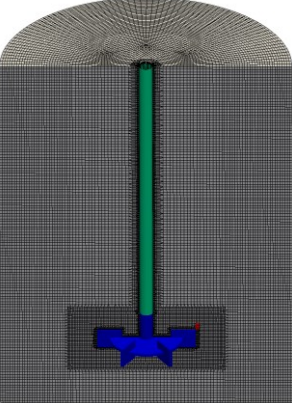
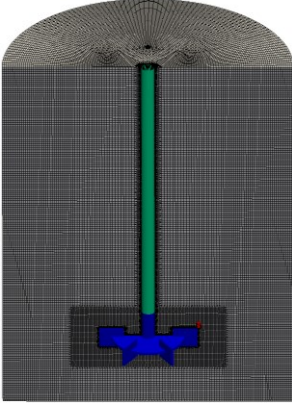
5.3.2. Case Setup and Meshing

As outlined for the Chapple case in section 4.3.2, the tank and impeller geometries were modelled using the SALOME pre-processing platform (Salome Platform, n.d.). Meshing was performed using a combination of tools available in SALOME and OpenFOAM. A structured background mesh was created for the tank without the impeller using SALOME. Subsequently, the OpenFOAM utility snappyHexMesh was used to cut out and conform the mesh to the impeller, which results in a hexahedral-dominant unstructured mesh.

As for the Blais case described in section 4.2.2, the size of the rotating zone is somewhat arbitrary, but its dimensions should not impact the results. The size of the rotating domain was chosen such that its boundary is halfway between the impeller tip and baffle walls in the radial direction and one blade widths above and below in the axial direction. This resulted in a diameter of 0.146 m and a height of 0.058 m for the zone. Only MRF simulations are performed for the Assirelli cases. The rotating zone was therefore defined as a cellZone, and an appropriate volumetric force was applied to represent the rotation of the impeller. The OpenFOAM utility topoSet was used to add four evenly spaced infinitely thin baffles. Additionally, topoSet was used to add the feed as a cellZone, and a corresponding mass and momentum source of $3.33 \times 10^{-8} \text{ m}^3/\text{s}$ (2 mL/min) was applied to represent the injection of reactants.

A mesh dependence study was performed for the Assirelli case with the goal of investigating model prediction sensitivity to grid size. The three computational meshes considered are summarized in Table 5.8. As for the Blais and Chapple cases in section 4.2.2 and 4.3.2, the meshes were generated by building a background mesh of 816 480 hexahedral cells for the intermediate mesh (Mid Mesh), a background mesh having 25% less cells for the Coarse Mesh, and a background mesh having 25% more cells for the Fine Mesh. As shown in Table 5.8, one level of local refinement was added for the rotating zone, two levels were added around the impeller and shaft, and one level for the feed addition point. This was accomplished using the mesh cell splitting technique available in snappyHexMesh.

Table 5.8: Computational meshes used in the Assirelli case.

	Coarse Mesh	Mid Mesh	Fine Mesh
Mesh			
Number of 3D cells	679 066	1 473 154	2 719 425
Number of 3D hexahedral cells	650 518	1 427 375	2 647 758
Maximum aspect ratio	3.44	3.89	5.00
Average non-orthogonality	10.20	9.32	8.74
Maximum Skewness	2.86	1.85	3.37
Minimum cell volume	$2.21 \times 10^{-10} \text{ m}^3$	$8.92 \times 10^{-11} \text{ m}^3$	$2.13 \times 10^{-11} \text{ m}^3$
Maximum cell volume	$1.06 \times 10^{-7} \text{ m}^3$	$4.65 \times 10^{-8} \text{ m}^3$	$2.36 \times 10^{-8} \text{ m}^3$
Total Volume	$24.8 \times 10^{-3} \text{ m}^3$	$24.8 \times 10^{-3} \text{ m}^3$	$24.8 \times 10^{-3} \text{ m}^3$
Rotating zone diameter	0.146 m	0.146 m	0.146 m
Rotating zone height	0.058 m	0.058 m	0.058 m
Average Courant Number	0.019	0.025	0.031
Maximum Courant Number	0.780	0.766	1.42

Fluid properties used for the Assirelli case are summarized in Table 5.9. The initial conditions for the impeller and turbulence fields are shown in Table 5.10. The initial velocity fields and pressure fields were set to 0. Standard low Reynolds number wall functions were used for k and ε . Mass injection was accomplished by a modified

simpleFoam solver to include an additional source term. The initial flow rate is shown in Table 5.13.

The initial conditions for the reactive mixing simulations are summarized in Table 5.12. The initial mixture fraction and reaction progress variable fields were set to 0. For each Reynolds number flow simulation, one reactive mixing simulation was performed using concentrations outlined in Table 5.13. Additionally, Table 5.13 outlines source terms applied to the mixture fraction variables corresponding to the feed injection. Reported values of X_S were taken after a time when its rate of change was less 1×10^{-6} .

Table 5.9: Liquid properties used for the Assirelli case.

Property	Value
Density, ρ (kg/m ³)	997
Dynamic viscosity, μ (Pa s)	0.89×10^{-3}
Turbulent Schmidt number, Sc_t	0.7
*Molecular diffusion coefficient, D_T (m ² /s)	1.0×10^{-9}

*Assumed value negligible compared to turbulent diffusion.

Table 5.10: Initial conditions for the incompressible turbulent flow simulations in the Assirelli Rushton turbine cases.

Reynolds number, $(\rho ND^2/\mu)$	Impeller speed, N (1/s)	Turbulent kinematic viscosity, ν_t (m ² /s)	Turbulent kinetic energy, k (m ² /s)	Turbulent energy dissipation, ϵ (m ² /s ³)
46 744	5	1.0×10^{-11}	6.02×10^{-4}	2.02×10^{-3}
65 411	7	1.0×10^{-11}	1.09×10^{-3}	4.88×10^{-3}
81 296	8.7	1.0×10^{-11}	1.59×10^{-3}	8.64×10^{-3}
85 968	9.2	1.0×10^{-11}	1.75×10^{-3}	1.00×10^{-2}

Table 5.11: Boundary and initial conditions used for the Assirelli steady-state incompressible turbulent flow simulations.

Variable	Shaft	Impeller	Walls	Top
Velocity, U (m/s)	RotatingWall Velocity	MovingWall Velocity	noSlip	slip
Pressure, P (Pa)	zeroGradient	zeroGradient	zeroGradient	zeroGradient
Turbulent kinematic viscosity, ν_t (m ² /s)	nutkWall Function	nutkWall Function	nutkWall Function	calculated
Turbulent kinetic energy, k (m ² /s)	kLowReWall Function	kLowReWall Function	kLowReWall Function	zeroGradient
Turbulent energy dissipation, ε (m ² /s ³)	epsilonWall Function	epsilonWall Function	epsilonWall Function	zeroGradient

Table 5.12: Boundary and initial conditions used for the Assirelli reactive mixing simulations.

Variable	Internal Field	Impeller	Shaft	Walls
Mixture fraction, α_1 (-)	uniformValue = 0	zeroGradient	zeroGradient	zeroGradient
Mixture fraction in environment 1, X_1 (-)	uniformValue = 0	zeroGradient	zeroGradient	zeroGradient
Mixture fraction in environment 2, X_2 (-)	uniformValue = 0	zeroGradient	zeroGradient	zeroGradient
Reaction progress in environment 1, Y_1 (-)	uniformValue = 0	zeroGradient	zeroGradient	zeroGradient
Reaction progress in environment 2, Y_2 (-)	uniformValue = 0	zeroGradient	zeroGradient	zeroGradient

Table 5.13: Initial concentrations and volumetric flow rate used in the Assirelli cases.

Variable	Value
*Concentration of injected acid, A_0 (H_2SO_4 mol/m ³)	1000
Concentration of borate ion, B_0 (H_2BO_3^- mol/m ³)	90.9
Concentration of iodine ions, D_0 (mol/m ³)	14.03
Concentration of sulfate ion, S_0 (mol/m ³)	500
**Momentum source for U_z (m ² /s ²)	-1.42×10^{-9}
Mass source injection p , α_1 , and X_1 (m ³ /s)	3.33×10^{-8}

*Rate constant k_2 (m¹²/mol⁴/s) is evaluated using local values. **Negative indicates downward injection.

5.4. Akiti Case

The second stirred tank reactor validation case was based on the experimental setup of Akiti and Armenante (2004). The purpose of this case was to validate power number and reaction yield predictions for the third Bourne competitive-parallel reaction scheme for the case of a stirred tank reactor equipped with a six-blade downward pumping pitched blade impeller. The objectives of this case were to compare reaction yield predictions both experimental data and simulation results of Duan et al. (2016). The impact of mesh resolution was also evaluated for this alternative mixing sensitive reaction scheme.

In the experiments described by Akiti and Armenante (2004), hydrochloric acid (HCl) and ethyl monochloroacetate ($\text{CH}_2\text{ClCOOC}_2\text{H}_5$) were initially premixed in the reactor at concentrations of 18 mol/m³ in a 19.5 L volume. The limiting reagent, sodium hydroxide (NaOH), was injected at a concentration of 900 mol/m³ through a 3 mm inner diameter feed pipe for 60 minutes. The total volume injected was 1/50 the tank volume which gives 391 mL NaOH. The fast neutralization and slower hydrolysis reactions compete for NaOH and therefore the product distribution (X_{S2}) can be represented as the yield of slower reaction relative to limiting reagent, $X_{S2} = P_2/A_0$.

5.4.1. Geometry and Mesh

Figure 5.3 shows the geometry used for the Akiti reactive mixing case. The stirred tank has an inner diameter $T = 0.292$ m with a liquid height of $H = T$. The tank wall has four baffles with a width of $B = T/10$. The reactor uses a six-blade downward-pumping 45°

pitched blade turbine with a diameter of $D = 0.102$ mm and blade width $W_b = 0.017$ mm positioned $C = T/3$ from the bottom wall. All dimensions are summarized in Table 5.14.

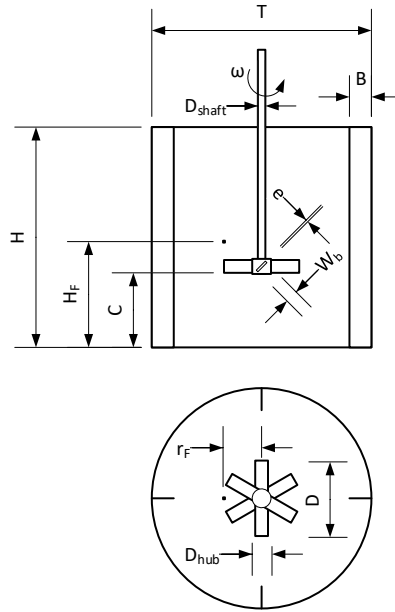


Figure 5.3: Geometry of the six-blade downward-pumping 45° pitched blade turbine of the Akiti and Armenante (2004) case.

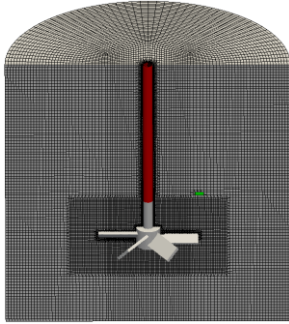
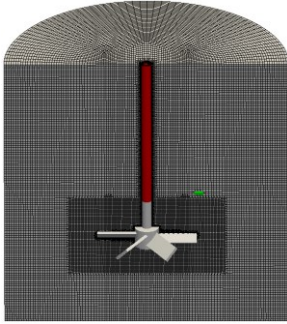
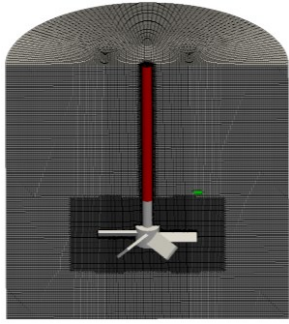
Table 5.14: Dimensions used in the Akiti case.

Name and Symbol	Dimension (m)
Tank diameter, T	0.292
Impeller diameter, D	0.102
Liquid level, $H = T$	0.292
Off-bottom clearance, $C = T/3$	0.0973
Baffle width, $B = T/10$	0.0292
Blade width, W_b	0.017
*Shaft diameter, D_{shaft}	0.01
*Hub height, H_{hub}	0.02
*Hub diameter, D_{hub}	0.025
*Blade thickness, e	0.003
Radial feed position, r_F	0.0502
Axial feed position, H_F	0.1402

*Estimated dimensions based on images of Duan et al. (2016) and Akiti (2000).

Three grids were considered in the Akiti case with the goal of studying the impact of mesh resolution on predicted reaction yields. The three chosen meshes are shown in Table 5.15.

Table 5.15: Computational meshes used for the Akiti case.

	Coarse Mesh	Mid Mesh	Fine Mesh
Mesh			
Number of 3D cells	830 323	1 314 295	4 277 423
Number of 3D hexahedral cells	800 495	1 277 339	4 194 291
Maximum aspect ratio	4.68	3.98	6.66
Average non-orthogonality	9.84	9.50	9.12
Maximum Skewness	3.99	3.26	3.62
Minimum cell volume	$8.95 \times 10^{-11} \text{ m}^3$	$4.53 \times 10^{-11} \text{ m}^3$	$1.25 \times 10^{-11} \text{ m}^3$
Maximum cell volume	$2.72 \times 10^{-5} \text{ m}^3$	$4.63 \times 10^{-8} \text{ m}^3$	$1.38 \times 10^{-8} \text{ m}^3$
Total Volume	$19.51 \times 10^{-3} \text{ m}^3$	$19.51 \times 10^{-3} \text{ m}^3$	$19.51 \times 10^{-3} \text{ m}^3$
Rotating zone diameter	0.155 m	0.155 m	0.155 m
Rotating zone height	0.080 m	0.080 m	0.080 m

5.4.2. Case Setup

The boundary conditions, initial conditions, and liquid properties for flow and reactive mixing simulations follow section 5.3.2 for the Assirelli et al. (2002) case and are summarized in Table 5.16, Table 5.17, Table 5.18, and Table 5.19. Geometry generation, meshing procedures, and boundary conditions for flow simulations follow that of cases presented in section 4.3.2 for Blais (2016) and Chapple et al. (2002) using the MRF meshing technique. The acid injection was accomplished via mass and momentum volumetric injection source terms.

Table 5.16: Boundary conditions used for the Akiti cases.

Variable	Shaft	Impeller	Walls	Top
Velocity, U (m/s)	RotatingWall Velocity	MovingWall Velocity	noSlip	slip
Pressure, P (Pa)	zeroGradient	zeroGradient	zeroGradient	zeroGradient
Turbulent kinematic viscosity, ν_t (m^2/s)	nutkWall Function	nutkWall Function	nutkWall Function	calculated
Turbulent kinetic energy, k (m^2/s)	kLowReWall Function	kLowReWall Function	kLowReWall Function	zeroGradient
Turbulent energy dissipation, ε (m^2/s^3)	epsilonWall Function	epsilonWall Function	epsilonWall Function	zeroGradient

Table 5.17: Boundary and initial conditions used for the reactive mixing Akiti case.

Variable	Internal Field	Impeller	Shaft	Walls
Mixture fraction, α_1 (-)	uniformValue = 0	zeroGradient	zeroGradient	zeroGradient
Mixture fraction in environment 1, X_1 (-)	uniformValue = 0	zeroGradient	zeroGradient	zeroGradient
Mixture fraction in environment 2, X_2 (-)	uniformValue = 0	zeroGradient	zeroGradient	zeroGradient
Reaction progress in environment 1, Y_1 (-)	uniformValue = 0	zeroGradient	zeroGradient	zeroGradient
Reaction progress in environment 2, Y_2 (-)	uniformValue = 0	zeroGradient	zeroGradient	zeroGradient

Table 5.18: Initial conditions used in the Akiti case.

Reynolds number, ($\rho ND^2/\mu$)	Impeller speed, N (1/s)	Turbulent kinematic viscosity, ν_t (m^2/s)	Turbulent kinetic energy, k (m^2/s)	Turbulent energy dissipation, ε (m^2/s^3)
17 340	1.67	1.0×10^{-11}	9.54×10^{-5}	1.21×10^{-4}
34 680	3.33	1.0×10^{-11}	3.21×10^{-4}	7.44×10^{-4}
52 020	5.00	1.0×10^{-11}	6.53×10^{-4}	2.16×10^{-3}
69 360	6.67	1.0×10^{-11}	1.08×10^{-3}	4.59×10^{-3}

Table 5.19: Liquid properties used for the Akiti case.

Property	Value
Density, ρ (kg/m ³)	997
Dynamic viscosity, μ (Pa s)	0.89×10^{-3}
Turbulent Schmidt number, Sc_t	0.7
*Molecular diffusion coefficient, D_T (m ² /s)	1.0×10^{-9}

*Assumed value negligible compared to turbulent diffusion.

Table 5.20: Initial concentrations, volumetric flow rate, and reaction rate constant used for the Akiti cases.

Variable	Value
Concentration of injected sodium hydroxide, A_0 (NaOH mol/m ³)	900
Concentration of hydrochloric acid, B_0 (HCl mol/m ³)	18
Concentration of ethyl chloroacetate, D_0 (mol/m ³)	18
Reaction rate constant, k_2 (m ³ /mol/s)	0.0257
**Momentum source for U_z (m ² /s ²)	-5.13×10^{-10}
Mass source injection p, α_1 and X_1 (m ³ /s)	1.085×10^{-7}

**Negative indicates downward injection.

5.5. Results and Discussion

5.5.1. Conversion in CIJR

Figure 5.4 shows the predicted conversion of DMP (X_D) with comparison to both experimental data collected by Johnson and Prud'homme (2003) and CFD simulations performed by Liu and Fox (2006). The simulations were performed for a jet Reynolds number (Re_j) that ranges from 100 to 2 000 for two fixed initial concentrations of A of 9.373 mol/m³ and 8.212 mol/m³ (i.e., characteristic reaction times of $t_r = 317$ ms and $t_r = 181$ ms). Over the range of Re_j , the predictions are in good agreement with experimental and simulation data.

Figure 5.4 displays the expected trend of conversion decreasing with increasing Re_j . An increase in inlet flow rate, and effectively turbulent kinetic energy of the reactant inlet streams, determines a decrease in X_D . Qualitatively, this indicates that poor mixing leads to a favoured selectivity for the second slow reaction and a push towards kinetic limitations. At the lower end of Re_j , small changes in Re_j appear to lead to large changes in X_D , whereas

at the upper end, changes in X_D begin to slow with respect to Re_j . Values of Re_j smaller than approximately 400–500 strongly influenced conversion, whereas Re_j greater than 400–500 show a weak effect on conversion. This indicates the model is able to accurately estimate reaction yield when the system is said to be controlled by mixing limitations at low Re_j , controlled by intrinsic reaction kinetics at high Re_j , and influenced by both mixing and kinetics in between. It should be noted that simulation results from the present work and those of Liu and Fox (2006) are somewhat different, despite the models being almost identical. The differences are likely the result of higher mesh resolutions being used in the present work.

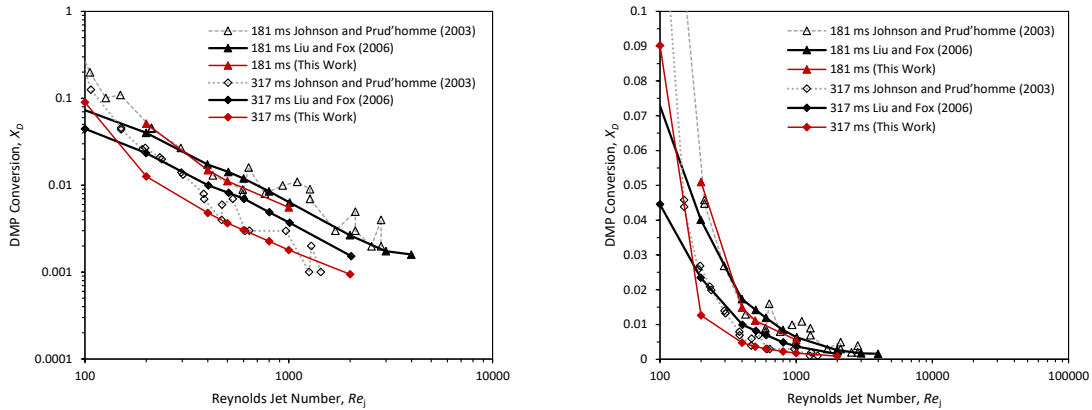


Figure 5.4: Impact of characteristic reaction time on the conversion of reactant D in the competitive-parallel reactions varying with respect to jet Reynolds number: logarithmic vertical scale (left) and linear vertical scale (right).

To better understand the mixing dynamics and how it relates to the reaction zone, this section follows the analysis performed by Liu and Fox (2006), where the flow fields and reaction zone is split into three limiting mechanisms: large-scale segregation controlling zones (LSS), small-scale segregation controlling zones (SSS), and zones controlled by both large and small-scale segregation (LSS & SSS). Liu and Fox (2006) determined the segregation zones using the LSS variance and SSS variance. The LSS zone, where mixing and reactions are said to be controlled by large motions of flow, was determined using the following expression:

$$a_3 > \sigma^2 \text{ and } a_2 < \sigma^2 \quad (5.1)$$

The reactions are controlled by SSS according to the following equation:

$$a_3 < \sigma^2 \text{ and } a_2 \geq \sigma^2 \quad (5.2)$$

The reactions are controlled by both LSS & SSS under the following conditions:

$$a_3 \geq \sigma^2 \text{ and } a_2 \geq \sigma^2 \quad (5.3)$$

The cut-off standard deviation (σ) used to define reacting regions is somewhat arbitrary. Liu and Fox (2006) define it as the distance in mixture fraction space from the end of reactions, the stoichiometric value X_{S1} , to complete mixing where both inlet streams are homogeneous, $\bar{a} = 0.5$.

$$\sigma = \bar{a} - X_{S2} = 0.0122 \quad (5.4)$$

The distributions of each segregation zone for $Re_j = 400$ and $Re_j = 1\ 000$ is shown in Figure 5.5. In the early part of the mixing domain, where mixture fraction variance a_2 is still high and close to the maximum value of 0.25, the system is blending-limiting, or commonly referred to as macromixing limited, or limited by LSS. This is illustrated in Figure 5.5 as the green inlet pipe sections. As the two fluids come into contact, gradients in mean mixture fraction (a_1) cause generation of mixture fraction variance (a_2) which is eventually dissipated to zero by local turbulence and a_1 approaches 0.5. During this process, the mixture fraction and its variance move towards their mean value, LSS has less influence than SSS, and the system is said to be micromixing-limited. This region is shown by the red region in Figure 5.5. Between these two limiting processes, the system is limited by both LSS & SSS, as shown in blue in Figure 5.5. From the distributions of various reaction and mixing zones for $Re_j = 400$ and $Re_j = 1\ 000$ in Figure 5.5, it is clear that the volume of the reaction zone decreases with increased Re_j . This is due to a higher mixing rate at the higher inlet flows.

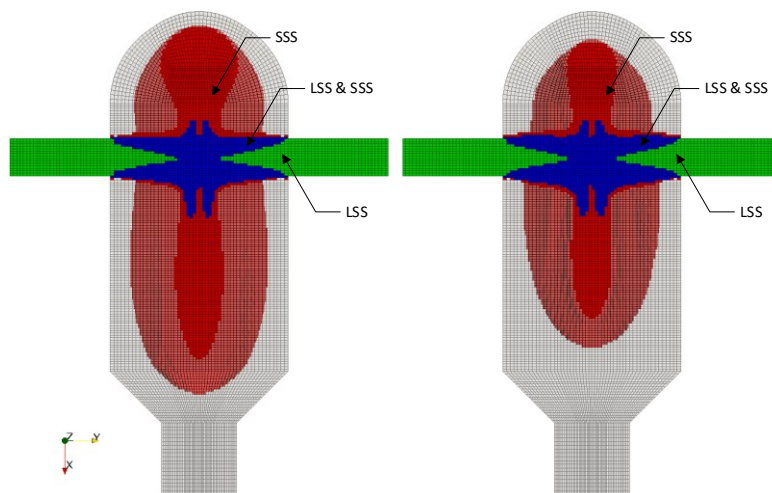


Figure 5.5: Distribution of segregation zones for $Re_j = 400$ (left) and $Re_j = 1\,000$ (right). Both use $\sigma = 0.0112$, intermediate mesh, and $t_r = 317$ ms.

To better understand and interpret these zones, the present work extends the analysis performed by Liu and Fox (2006) to include the mean turbulent energy dissipation rate ε (m^2/s^3) of each region and attempts to relate these mean values to conversion of the second reaction. Figure 5.6 (top row) shows the distribution of ε in the segregation regions for $Re_j = 400$ and $Re_j = 1\,000$. Figure 5.6 (bottom row) shows the distribution of ε on the symmetry plane for $Re_j = 400$ and $Re_j = 1\,000$.

From Figure 5.6, the average energy dissipation was computed as a volume-weighted mean. They were then analyzed with respect to the global average, LSS average, LLS & SSS average, and SSS average ε of each segregation zone and plotted against X_D , as shown in Figure 5.7. Energy dissipation is closely related to conversion as seen in Figure 5.7. The averaging of ε makes it challenging to evaluate the impact of each zone on reaction conversion and in determining which mechanism is controlling. It is possible that there is a shift from SSS to LSS at around $Re_j = 400\text{--}500$ (Liu & Fox, 2006). It is also possible that all limiting mechanisms are having a significant impact. The analysis was extended again to include distributions of ε , shown in Figure 5.8. The average distribution of ε roughly resembles a log normal distribution that spans 3–4 orders of magnitude. In general, although the average dissipation increases with increasing flow rate, the distributions also all tend to taper at higher flow rates. This could be due to the lower bound being more extreme at the lower flows. It is clear from Figure 5.8 that decreasing Re_j tends to broaden

the distribution of ε for the global average and also the ε distribution in the SSS region. This is likely a result of a more non-uniform mixing rate.

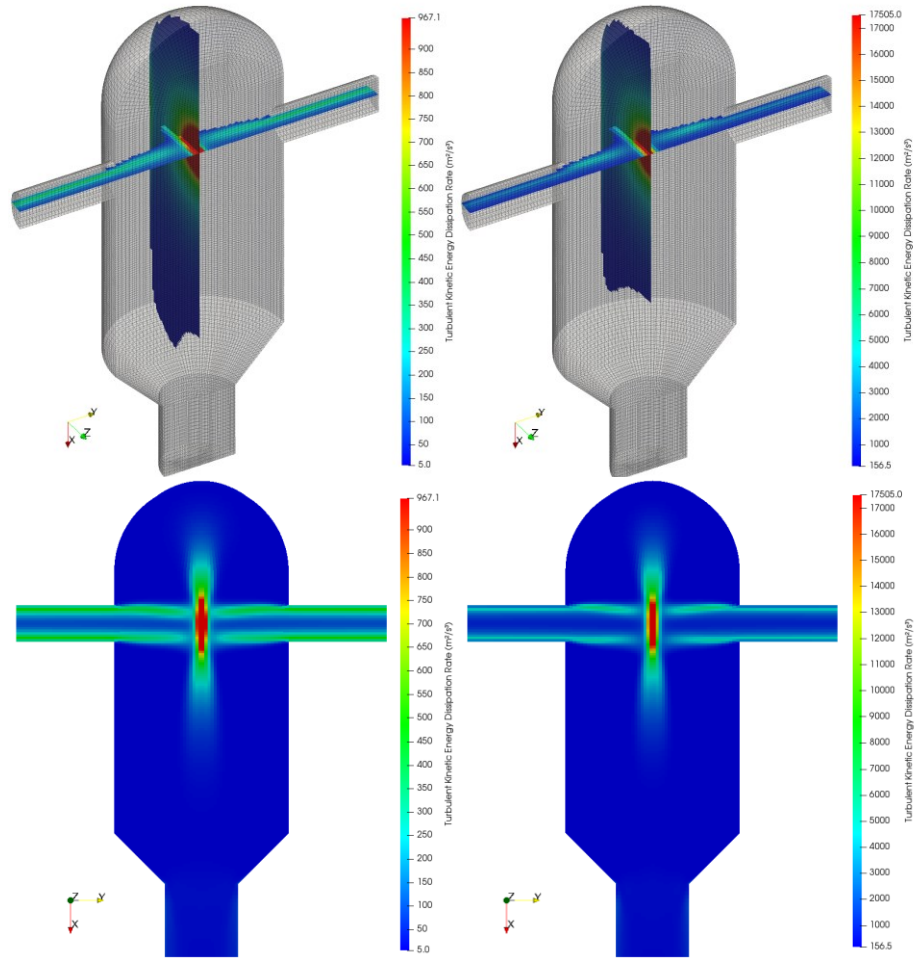


Figure 5.6: Distribution of segregation zones for (left to right) $Re_j = 400$ and $Re_j = 1\ 000$. Distribution of turbulent kinetic energy dissipation rate in the segregation zones (top row) and distribution of turbulent kinetic energy dissipation rate on the symmetry plane (bottom row). Segregation zones use $\sigma = 0.0112$. Intermediate mesh was used in the analysis.

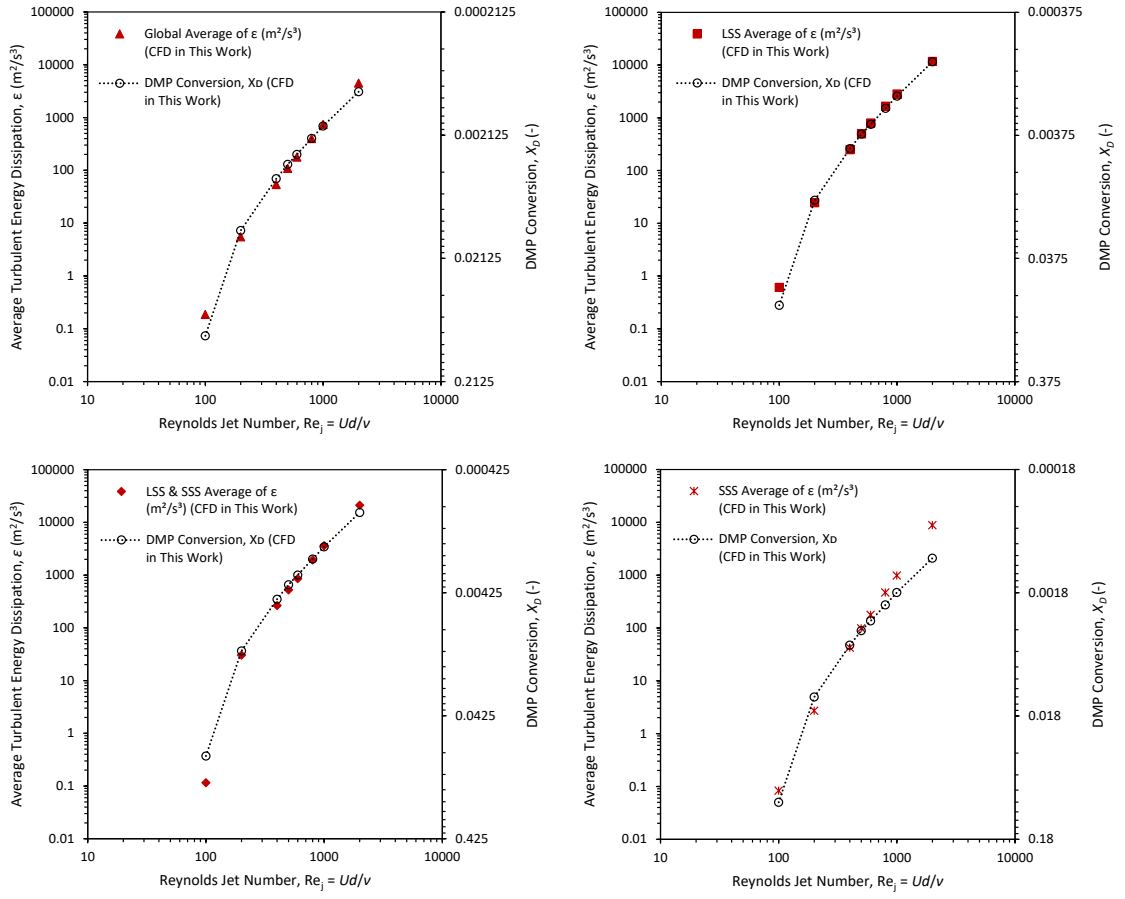


Figure 5.7: CFD predictions of the mean energy dissipation and DMP conversion varying with respect to jet Reynolds number.

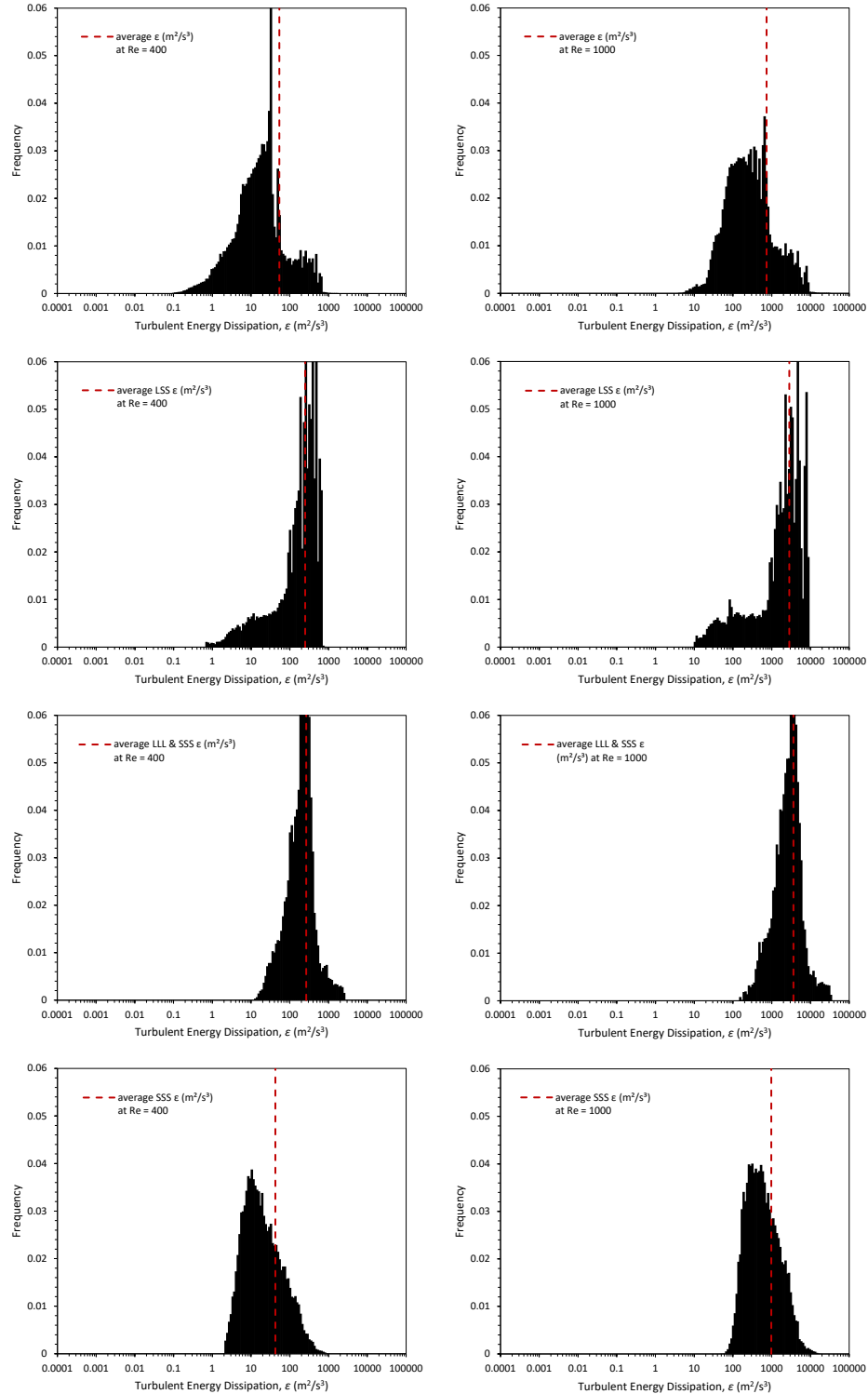


Figure 5.8: Turbulent energy dissipation rate distribution for (left column) intermediate mesh at a fixed $Re_j = 400$ and $t_r = 317$ ms and (right column) intermediate mesh at $Re_j = 1000$, $t_r = 317$ ms. All use $\sigma = 0.0112$. Mean values of ϵ are shown as red dashed lines.

5.5.2. Mesh Dependence Study in CIJR

A mesh dependence study was conducted for the four meshes described in Table 5.1 for the case of Liu and Fox (2006). One characteristic reaction time was studied ($t_r = 317$ ms) for a high $Re_j = 1\,000$. Figure 5.9 shows the predicted X_D varying with the number of mesh cells. Liu and Fox (2006) performed simulations with what they describe as at least 20 880 hexahedral cells. The authors mention more cells were required for mesh independent results at higher Re_j . Unfortunately, they do not expand on the number of cells used for these simulations, how the refinement was performed, or sensitivity on results. The coarse mesh used in this work was able to replicate simulation X_D results from Liu and Fox (2006). Figure 5.9 shows that, with increasing grid resolution, X_D decreases and eventually reaches a limiting value that closely represents the experimental data. The better agreement with experimental data seen in Figure 5.9 at the low Re_j range compared to Liu and Fox (2006) is likely attributed to the higher cell count used in this work. Richardson extrapolation was not performed due to the 4 million cell case deviating from the linear change. The intermediate mesh was adopted for all other simulations.

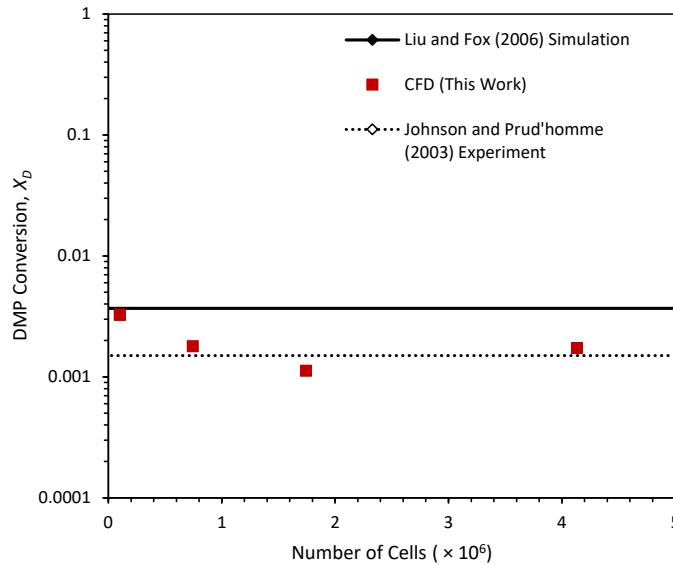


Figure 5.9: DMP conversion (X_D) varying with number of cells for coarse mesh, intermediate mesh, fine mesh, and ultra fine mesh at $Re_j = 1\,000$ and $t_r = 317$ ms.

Figure 5.10 shows the impact of mesh cell count on each LSS, LSS & SSS, and SSS segregation zones. For increased resolution, the reacting volume remains relatively unchanged for the intermediate and fine meshes. However, these results can be difficult to interpret due to limited information regarding flow fields and turbulence variables. The analysis was extended to include ε distributions for the coarse, intermediate, fine, and very fine meshes in Figure 5.11. In general, the distributions converge on range and shape at the intermediate mesh.

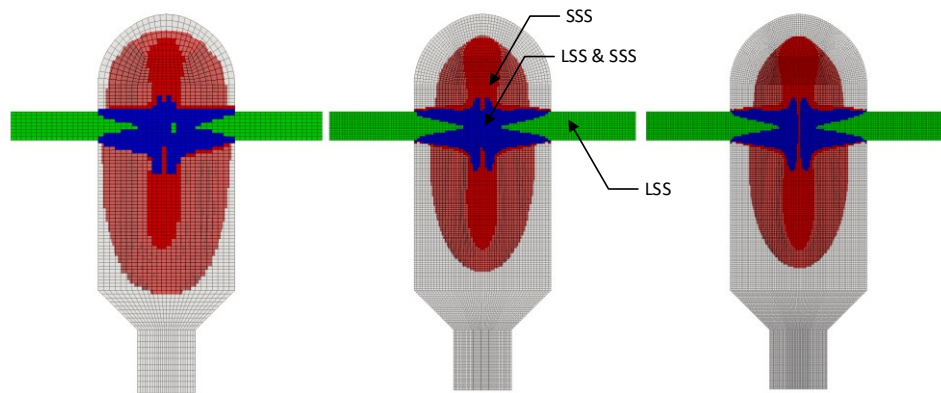


Figure 5.10: Distribution of the reaction and segregation zones for $Re_j = 1\,000$ and $t_r = 317$ ms for coarse mesh (left), intermediate mesh (middle), and fine mesh (right).

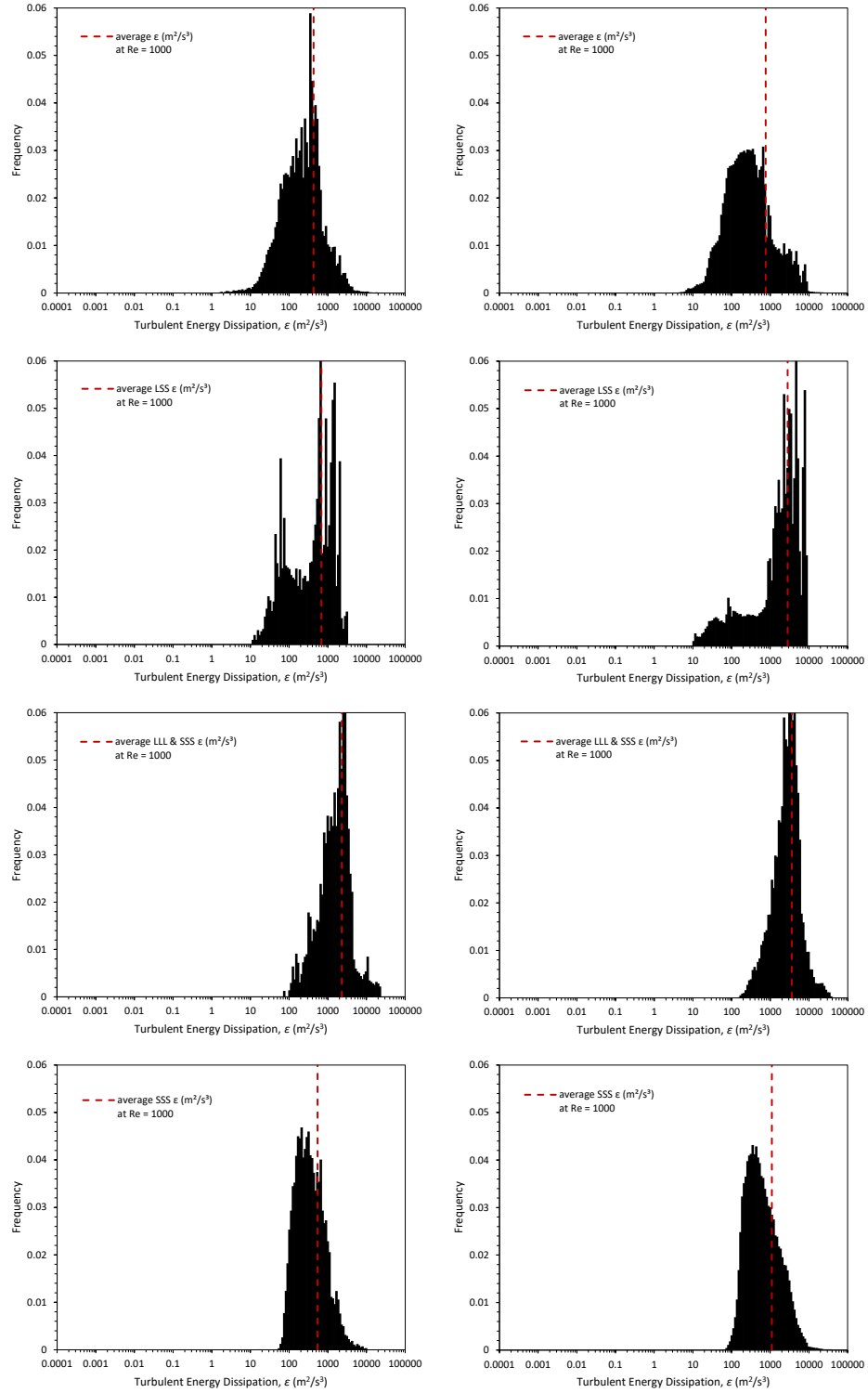


Figure 5.11: Turbulent energy dissipation rate distribution for (left column) coarse mesh and (right column) fine mesh at a fixed $Re_j = 1\,000$ and $t_r = 317$ ms. Mean of ϵ is shown as red dashed lines.

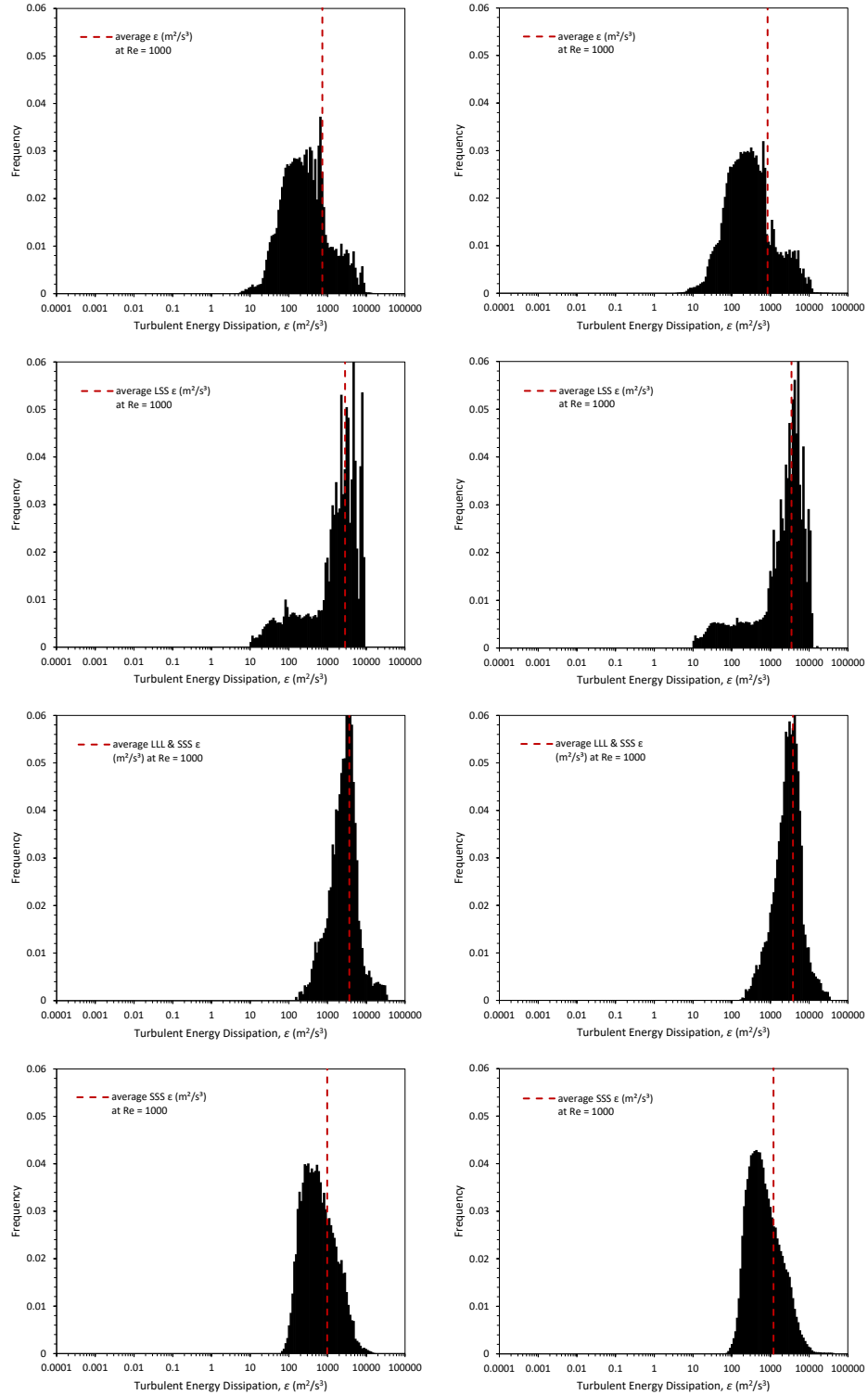


Figure 5.12: Turbulent energy dissipation rate distribution for (left column) intermediate mesh and (right column) very fine mesh at a given $Re_j = 1\,000$ and $t_r = 317$ ms. Mean of ϵ is shown as red dashed lines.

5.5.3. Reaction Zone Sensitivity in CIJR

The purpose of this section is to compare two methods for evaluating reaction zone size and shape. The first method follows the work of Fox and colleagues by selecting an arbitrary cut-off value for the mixture fraction variance (Liu and Fox., 2006). The second uses a mixture fraction variance weighted average of the turbulent energy dissipation rate (Duan et al., 2016). The former is non-symmetric whereas the latter is symmetric. The way in which reaction zones are defined directly impacts the size, shape, and location of where the reactions take place, and changes the average turbulent dissipation within the reacting region.

Figure 5.13 shows the impact of different cut-off standard deviation at $\sigma = 0.0976$, 0.0112 , and 0.01525 for representing the LSS and SSS zones. The range of values was chosen to be 25% lower and higher from the baseline value 0.0112 . This baseline value was selected following Fox and colleagues, as it has been used in CIJRs and MIVRs. From Figure 5.13, as the cut-off value σ increases, the volume of LSS increases, and at the same time, the volume of SSS decreases. The mean values of turbulent dissipation for LSS and LSS & SSS effectively do not change with different cut-off values, as seen in Table 5.21. In general, the average dissipation rate in the SSS zone increases as σ is increased. An increase/decrease of 2.5 times from baseline results in a 30–45% percent change. As seen in Figure 5.14 and Figure 5.15, this shift in average dissipation in the SSS region can be attributed to changes in the tail ends, spanning 2–3 orders of magnitude for the lowest σ and 1–2 orders of magnitude at the highest σ . The distribution of energy dissipation rate in LSS region generally spans 3 orders of magnitude and the shape is largely unaffected by increasing or decreasing σ . The region containing both LSS and SSS shows the highest broadening as σ is decreased, which seems to be in-line with changes in SSS.

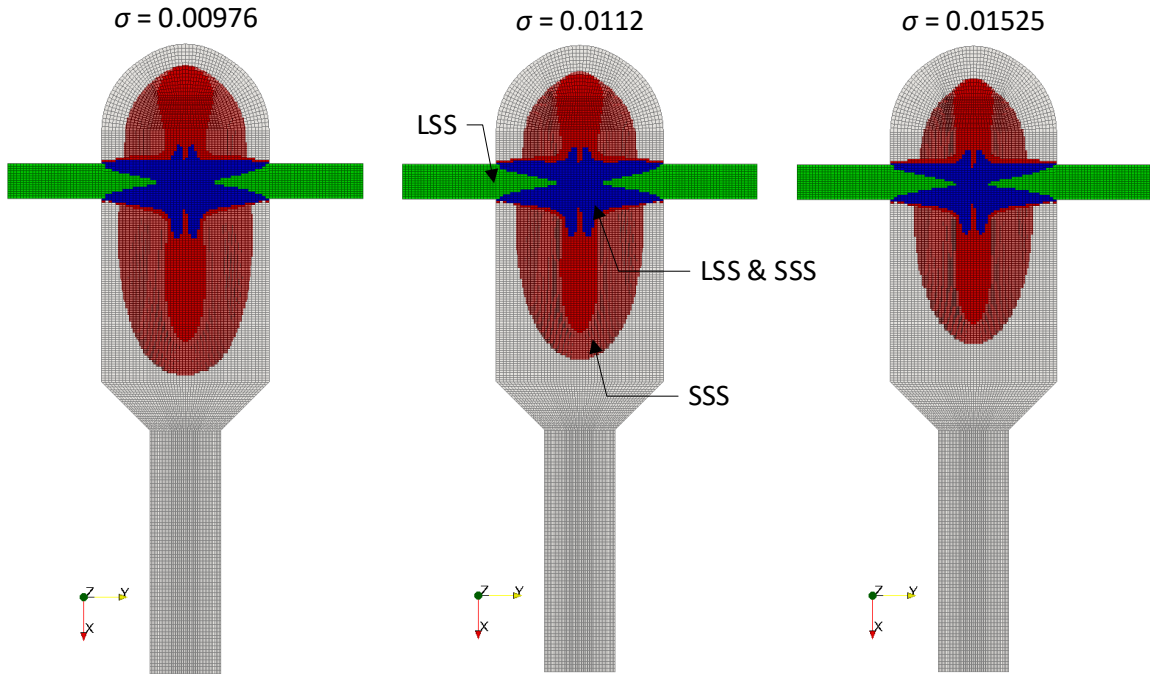


Figure 5.13: Distribution of the reaction and segregation zones for $Re_j = 1\,000$ and $t_r = 317$ ms using the intermediate mesh for $\sigma = 0.00976$ (left), $\sigma = 0.0112$ (middle), and $\sigma = 0.01525$ (right).

Table 5.21: Segregation zone impact on mean energy dissipation rate for $Re = 1\,000$ and $t_r = 317$ ms.

Cut-off Standard Deviation σ	Average Energy Dissipation in LSS Zone (m^2/s^3)	Average Energy Dissipation in LSS & SSS Zone (m^2/s^3)	Average Energy Dissipation in SSS Zone (m^2/s^3)
0.00488	2 835	3 016	512
0.00976	2 832	3 566	820
0.0112 (baseline)	2 829	3 640	976
0.01525	2 827	3 730	1 209
0.0305	2 820	3 624	2 270

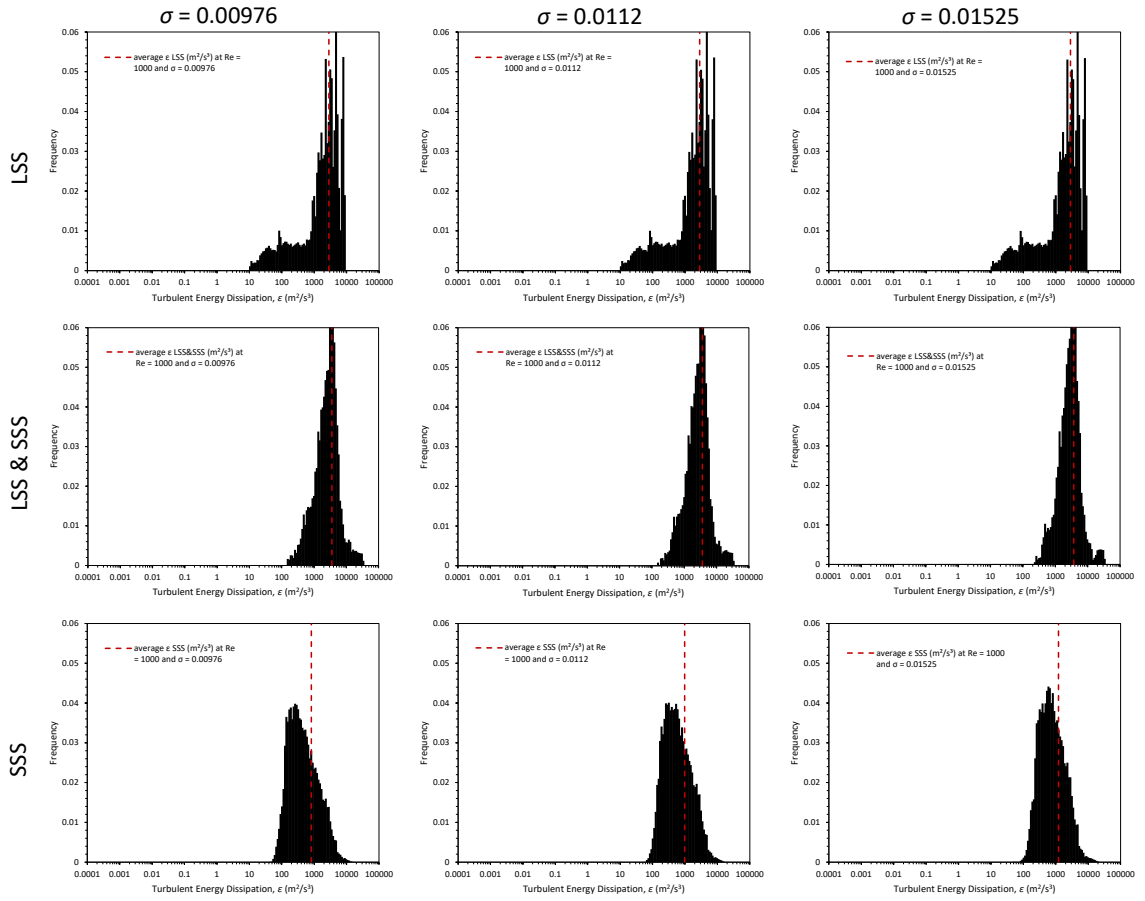


Figure 5.14: Sensitivity of distribution of the turbulent energy dissipation rate in each segregation zone for $Re_j = 1\ 000$ and $t_r = 317$ ms for $\sigma = 0.00976$ (left column), $\sigma = 0.0112$ (middle column), and $\sigma = 0.01525$ (right column).

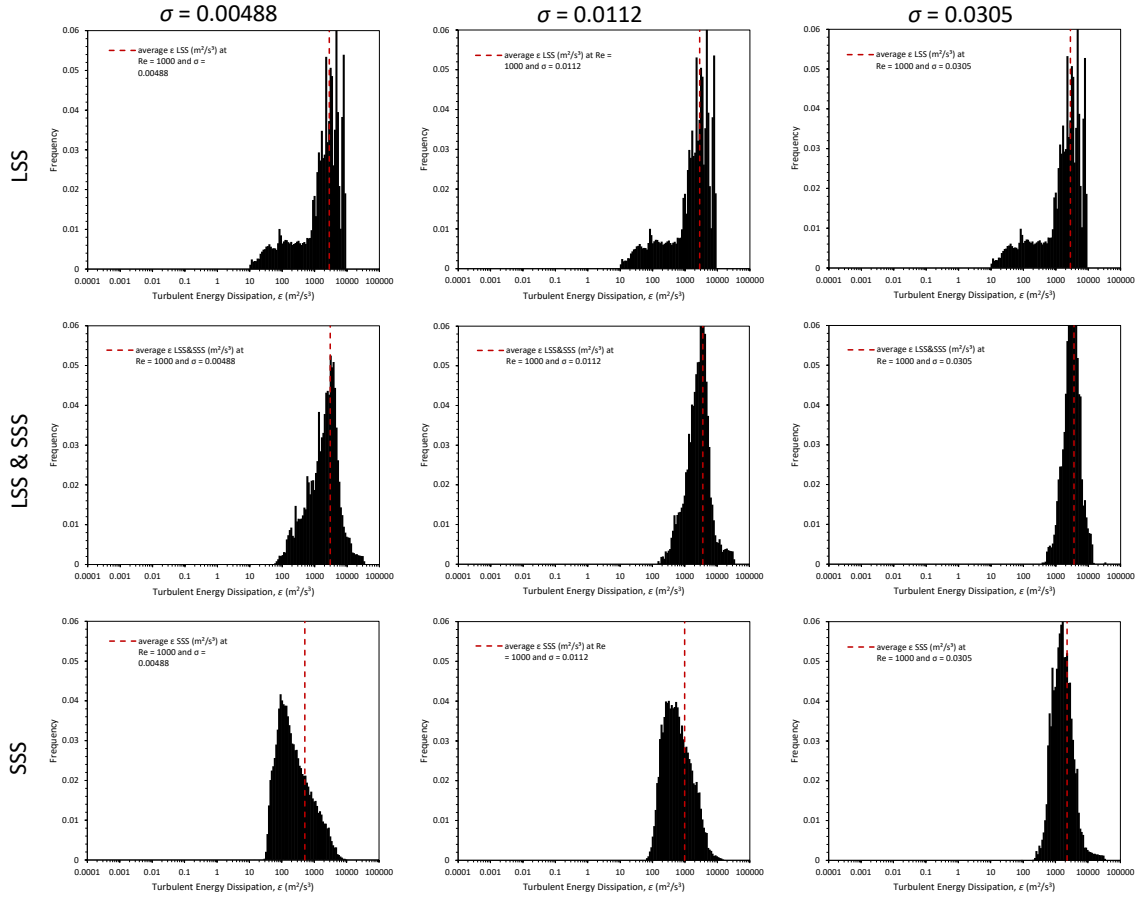


Figure 5.15: Sensitivity of distribution of the turbulent energy dissipation rate in each segregation zone for $Re_j = 1\,000$ and $t_r = 317$ ms for $\sigma = 0.00488$ (left column), $\sigma = 0.0112$ (middle column), and $\sigma = 0.0305$ (right column).

An alternative reaction zone averaging scheme is also considered for comparison. The analysis follows Duan et al. (2016), where the authors define a cut-off point as the ratio of mixture fraction variance to the maximum mixture fraction variance ($a_2/a_{2,max} \geq 0.1-0.001$). Figure 5.16 shows the distribution of ε generated according to the range of $a_2/a_{2,max}$ values. A graphical representation of the regions that define these distributions is presented in Figure 5.17 for $a_2/a_{2,max} \geq 0.01$ at two Reynolds numbers ($Re = 400$ and $1\,000$). As expected, each segregation zone has a different distribution of ε due to the defined threshold changing the size of the reacting volume. Similar to the definition of Liu and Fox (2006), the reacting region decreases in size with increasing flow rate. The advantage of the Duan et al. (2016) averaging method based on mixture fraction variance is that it leads to symmetric regions. The average values for each cut-off ratio, along with the average

variance weighted ε outlined previously in section 3.2.4, are summarized in Table 5.22. For a given flow scenario, average ε can vary up to one order of magnitude. The inconsistent definition of σ and/or $a_2/a_{2,max}$ displayed in Figure 5.16 and Table 5.22 make it challenging to evaluate the true average ε in the reaction zone. This means that it is difficult to evaluate a true mixing time using either method, but it is possible to obtain mixing time trends.

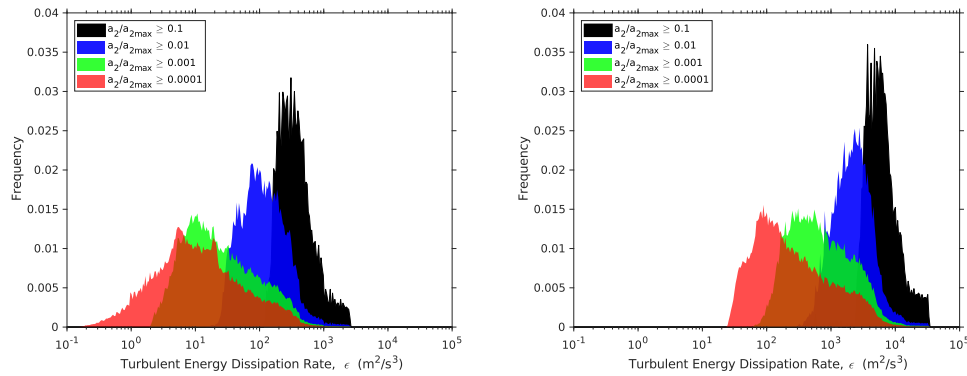


Figure 5.16: Distribution of turbulent energy dissipation rate for $Re_j = 400$ (left) and $Re_j = 1\ 000$ (right) and $t_r = 317$ ms.

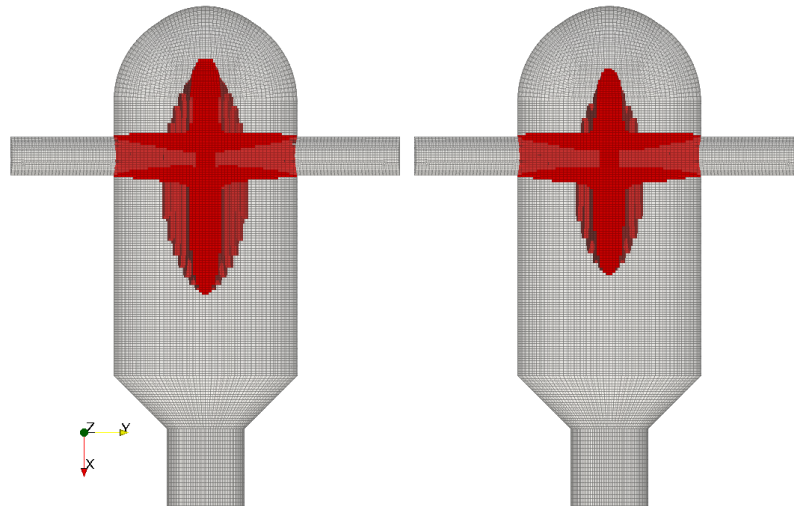


Figure 5.17: Distribution of segregation zones for $Re_j = 400$ (left) and $Re_j = 1\ 000$ (right) and $t_r = 317$ ms and $a_2/a_{2,max} \geq 0.01$.

Table 5.22: Segregation zone impact on mean energy dissipation rate for $Re = 400$ and $1\ 000$ for $t_r = 317$ ms using a cut-off variance ratio.

Reynolds Number, Re	Average Energy Dissipation using $a_2/a_{2,max} \geq 0.1$ (m^2/s^3)	Average Energy Dissipation using $a_2/a_{2,max} \geq 0.01$ (m^2/s^3)	Average Energy Dissipation using $a_2/a_{2,max} \geq 0.001$ (m^2/s^3)	Average Energy Dissipation using $a_2/a_{2,max} \geq 0.0001$ (m^2/s^3)	Variance-Weighted Average Energy Dissipation (m^2/s^3)
400	457.5	161.2	60.7	38.7	478.95
1000	7433	2847	1280	701.6	7786.9

The DMP conversion data shown in Figure 5.18 for variance-weighted, LSS & SSS, LSS, and SSS averaging of ε is in good agreement with published reduced-order models for characterizing micromixing. For the variance weighted and LSS & SSS datasets, the slope resembles that of the engulfment model. However, when LSS and SSS are considered separately, the curves deviate on the high and low ends of dissipation rate. Liu and Fox (2006) interpret this as a shift from SSS controlling to LSS controlling mechanisms around $Re = 500$. In reality, reaction yield is likely governed by both LSS and SSS. In Chapter 6, the variance weighed averaging of ε is used to evaluate the E parameter and subsequently carry out a comparison study between E-model and DQMOM-IEM predictions of X_S . Due to symmetric reaction zones and no reliance on cut-off values, this averaging provides a convenient basis for comparison.

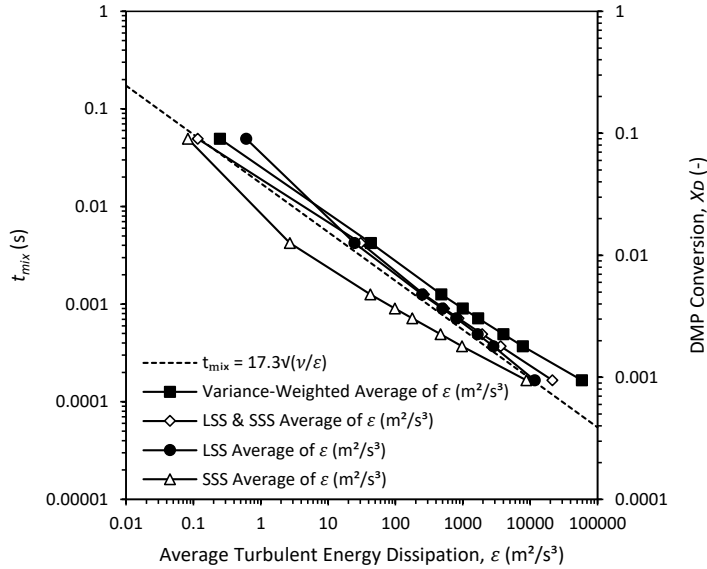


Figure 5.18: Average turbulent energy dissipation rate of different zones as a function of mixing time (left axis) and conversion (right axis). Simulations used the intermediate mesh with $t_r = 317$ ms.

5.5.4. Mixing Power in Stirred Tank Reactors

Figure 5.19 (left) shows the impact of Reynolds number on power number predictions for the Assirelli et al. (2002) simulation case using the intermediate mesh detailed in Table 5.8. Increasing Reynolds number generally does not influence power number, as is expected in the turbulent regime (Paul et al., 2003). Assirelli et al. (2002) report a power number of 4.33. Unfortunately, the authors do not comment on the Reynolds number or the accuracy of the measurement, but they operated in the turbulent regime. Generally, the simulation predictions are in good agreement with experimental data.

Figure 5.19 (right) shows the impact of grid size on power number predictions using the three meshes outlined in Table 5.8. These simulations were performed using the highest Reynolds number at 85 970 (552 rpm) to ensure all other stir speeds were resolved. Power number computed from the integrated rate of turbulent energy dissipation shows the expected trend of increasing with increased mesh resolution. Torque based power number stays constant and seems to be generally less sensitive to changes in grid size. As noted in Section 4.4, these data show that torque based power number converges faster than

dissipation rate based power number. Based on these results, all simulations used the intermediate mesh.

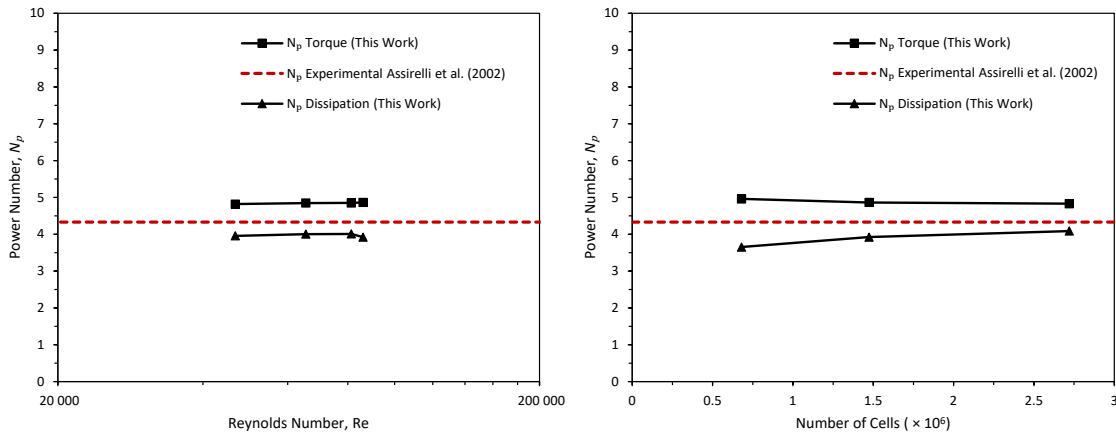


Figure 5.19: Comparisons between the experimental and simulated power number values for the Assirelli et al. case with varying Reynolds number (left) and varying with grid size (right) for the coarse mesh, intermediate mesh, and fine mesh for $N = 552$ rpm ($Re = 85\,970$).

Figure 5.20 (left) shows power number predictions and a comparison between both measured power number and computed power number for the Akiti and Armenante (2004) case. Although the experiments show some variability, the authors did not comment on these data. Predicted power number based on the energy dissipation agrees well with the experimental data. Akiti and Armenante (2004) and performed CFD simulations and calculated power number based on energy dissipation rate. Akiti (2000) provides additional power number results varying with Reynolds number. Figure 5.20 (right) gives power number predictions varying with grid size at the highest Reynolds number of 69 360 (400 rpm). Again, the torque based power number shows less sensitivity to mesh resolution and the prediction is relatively close to the experimental measurement.

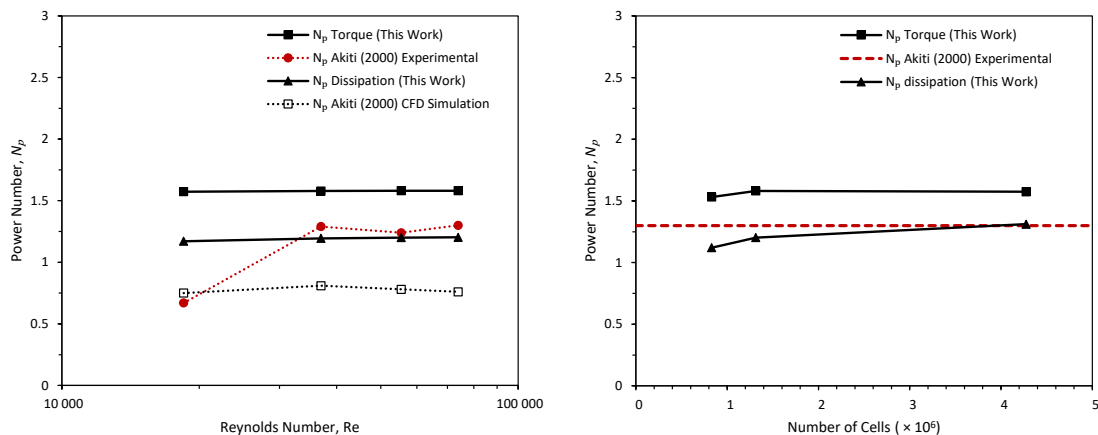


Figure 5.20: Comparisons between the experimental and simulated power number values for the Akiti case varying with Reynolds Number (left) and varying with the number of cells (right) for a fixed Reynolds number ($Re = 69\,360$).

5.5.5. Conversion of Mixing Sensitive Reactions in Stirred Tank Reactors

Figure 5.21 (left) shows the predicted segregation index as a function of Reynolds number for the Assirelli et al. (2002) case where the Villermaux-Dushman reaction scheme was used. These simulations were performed using the intermediate mesh summarized in Table 5.8. The simulation predictions show reasonable agreement with experimental trends, but the results are different than the simulations by Duan et al. (2016). Model predictions are approximately 50% higher than results from Duan et al. (2016). Unfortunately, Duan et al. (2016) do not report variance weighted turbulence parameters obtained from their model implementation, which makes it challenging to investigate the cause of the mismatch between predictions. The E-model was implemented to better understand the mismatch between predictions. Although reaction yields are over predicted, the E-model implemented in this work leads to reaction times very close to Duan et al. (2016), as illustrated in Figure 5.23. These findings likely suggest the engulfment parameter E evaluated from Eq. (3.68) and (3.69) is close to that of Duan et al. (2016). At the lowest Reynolds number simulated, E would have to increase by approximately 2.5 times to see similar X_S values to Duan et al. (2016). Figure 5.21 (right) displays the sensitivity of segregation index to changes in grid size, and as expected, segregation index approaches the limiting experimental value with increased cell number.

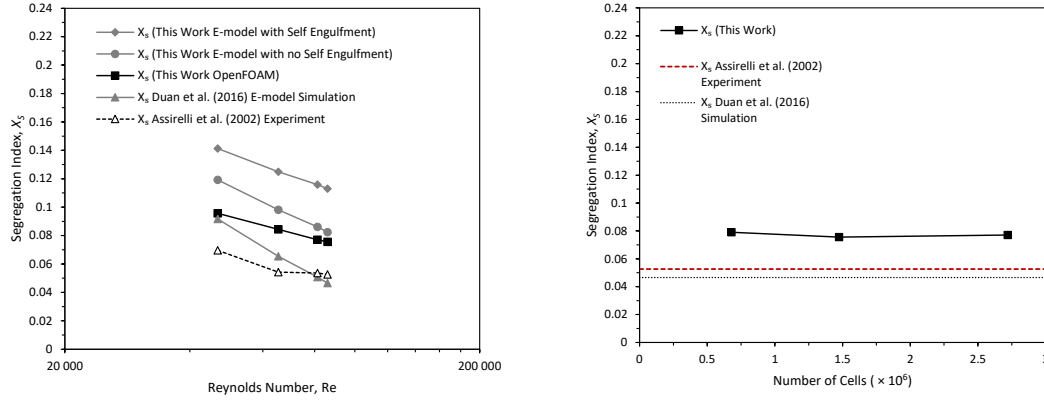


Figure 5.21: Comparisons between the experimental and simulated segregation index (X_S) for the Assirelli case varying Re ($N = 300, 420, 522, 552$ rpm) (left) and varying with grid size for the coarse mesh, intermediate mesh, and fine mesh (right) at a fixed $Re = 85\,970$ ($N = 552$ rpm).

The distributions of turbulent energy dissipation rate are plotted for the Assirelli case and displayed in Figure 5.22 for 300 (left) and 552 rpm (right) using the intermediate mesh summarized in Table 5.8. The solid black line shows the distribution of turbulent energy dissipation rate for the entire domain which covers a broad range of energies spanning 5 orders of magnitude. It is clear that taking the energy distribution in the reaction zone, defined as a range of mixture fraction variance values (Duan et al., 2019), separates the peaks and the distribution. Using the tail end values of energy dissipation as input to the E-model leads to more comparable predicted X_S with experimental measurements. For $Re = 85\,969$, using a dissipation rate of $100\text{ m}^2/\text{s}^3$ results in $X_S = 0.061$ (0.053 exp).

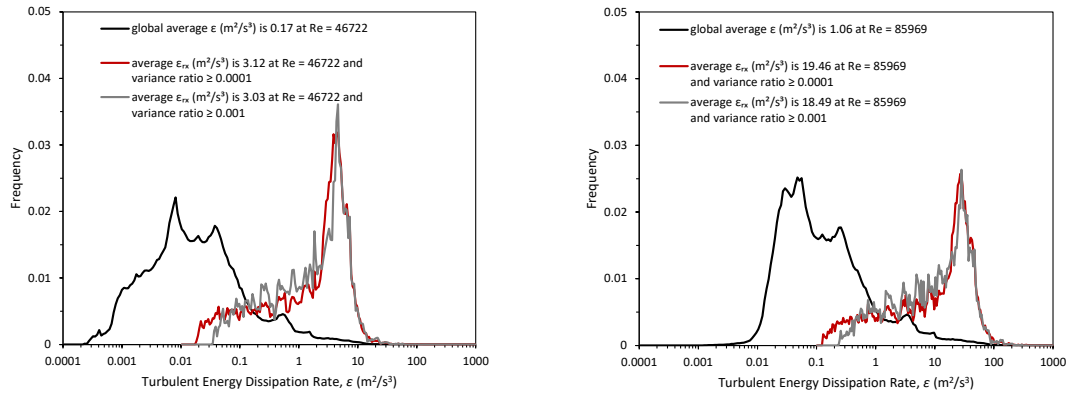


Figure 5.22: Distribution of turbulent kinetic energy dissipation rate for the Assirelli case with $Re = 46\,722$ (left) and $Re = 85\,969$ (right).

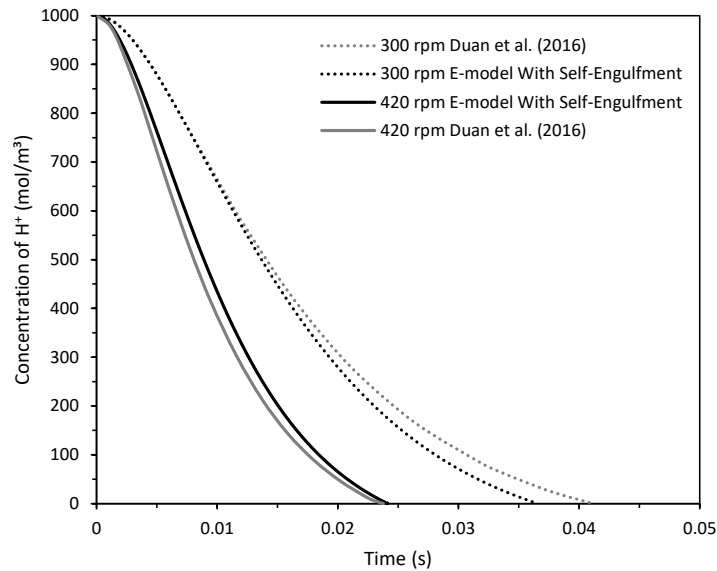


Figure 5.23: Comparison of E-model implementation with simulation results from Duan et al. (2016) showing depletion of component A during the first addition of feed element for fixed Re ($N = 300$ and 420 rpm) for the Assirelli case.

Figure 5.24 (left) shows reaction conversion predictions at varying stir speeds for the Akiti and Armenante (2004) case. The trend in segregation index agrees well with the experimental data. However, the model underestimates the conversion. Chapter 6 of this thesis will investigate the effect of varying micromixing parameter C_ϕ . Unlike the Assirelli

case, the E-model implementation showed a very weak effect of the self-engulfment term on reaction yield.

Mesh dependence was performed on the highest Reynolds number and outlined in Figure 5.24 (right). The plots shows very little dependence of the predictions on mesh resolution.

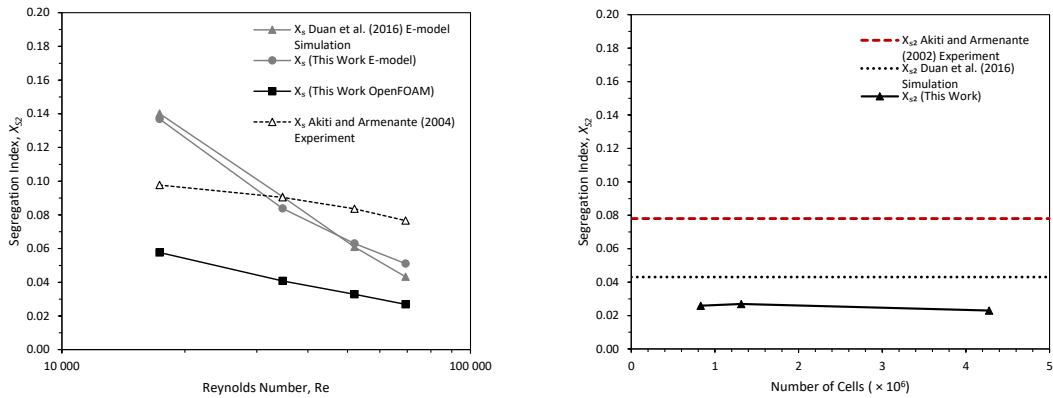


Figure 5.24: Comparisons between the experimental and simulated X_{S2} for the Akiti case varying with Re ($N = 100, 200, 300, 400$ rpm) (left) and varying with grid size for coarse mesh, intermediate mesh, and fine mesh (right) at a fixed $Re = 69\,360$ ($N = 400$ rpm).

Figure 5.25 (left) shows a comparison between E-model simulations of Duan (2016) and the implemented E-model of this work with sensitivity analysis of including self-engulfment with reactor volume and without reactor volume changes. Figure 5.25 (right) displays E-model predictions without the use of a self-engulfment term and shows sensitivity to constant versus fixed reactor volume. At lower Reynolds number flows, there is deviation between the two model predictions with and without volume change for both self-engulfment and non self-engulfment predictions. As Reynolds number increases, this deviation decreases. The self-engulfment term seems to cause a vertical shift in segregation index, indicating that blending is having an impact on mixing performance.

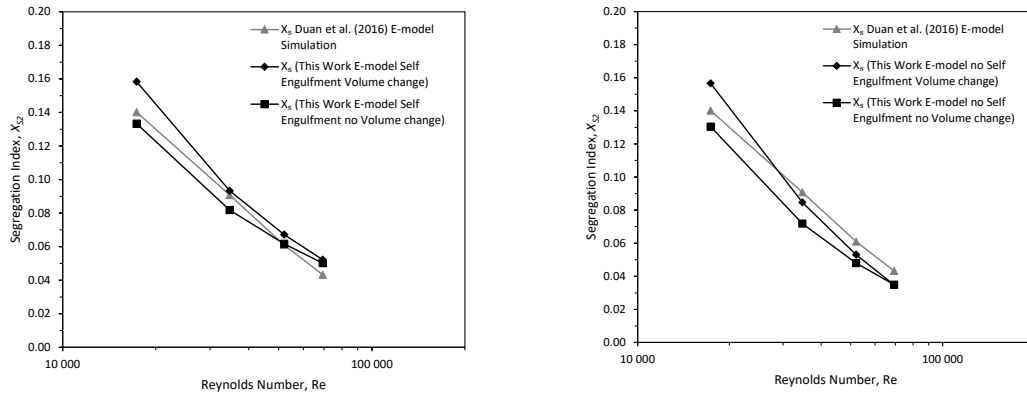


Figure 5.25: Comparisons between the simulated Duan et al. (2016) data and simulated E-model X_S for the Akiti case sensitivity to environment volume changes with self-engulfment (left) and sensitivity to environment volume changes without self-engulfment (right).

5.6. Summary

This chapter summarized validation studies for the DQMOM-IEM modelling approach for various reaction schemes: third Bourne reactions, fourth Bourne reactions, and Villermaux-Dushman reactions. Model predicted trends show good agreement with experimental trends. Results from E-model predictions were used to explain some of the differences between predictions and measurements. Mesh dependence studies were performed to ensure numerical accuracy of the results. Chapter 6 will investigate the impact of sub-grid scale model parameters on predicted reaction yield, which could explain some of the differences between predictions and experimental data seen in stirred tank reactor cases. Chapter 6 will use the mixture fraction variance weighted averages for turbulence parameters as input to the E-model.

CHAPTER 6: MODELLING OF COMPETITIVE-PARALLEL REACTIONS IN SMALL-SCALE CRYSTALLIZATION REACTORS

6.1. Introduction

The goal of this chapter is to investigate yield of the Villermaux-Dushman reaction over various reactant concentrations and flow conditions for a common small-scale crystallization reactor. Simulations presented in this section are compared with the experimental data. Chapter 3 provides an overview of the experimental methodology used to measure yield for the Villermaux-Dushman reaction scheme. The case study uses the EasyMax 402 stirred tank reactor. The stirred tank reactor has a liquid volume of 300 mL and is significantly smaller than the Assirelli et al. (2002) and Akiti and Armenante (2004) cases presented in Chapter 5 and therefore offers a good validation case at a smaller scale. The EasyMax402 stirred tank reactor was operated with a retreat curve impeller at Reynolds number of 8333–25000 (200–600 rpm). These conditions were selected to best resemble those commonly used in bench-scale laboratory experiments. This chapter extends the analysis presented in Chapter 5 by applying the methodology to a reactor more commonly used for crystallization.

6.1.1. Geometry

A sketch of the EasyMax 402 stirred tank reactor is shown in Figure 6.1. The tank vessel has diameter of $T = 0.101$ m. The impeller is a three bladed retreat curve impeller with a diameter of $D = 0.050$ m. The inner diameter of the injection feed pipe is 0.81 mm and it was placed horizontally halfway between the impeller tip and vessel wall at a height of 0.0288 m. All other dimensions are summarized in Table 6.1.

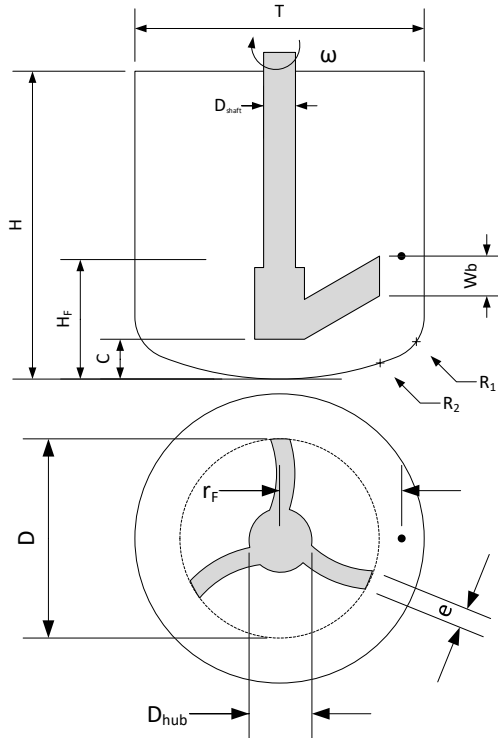


Figure 6.1: Geometry of the EasyMax402 reactor with the retreat curve impeller used in experiments for this work.

Table 6.1: Dimensions used in the stirred tank crystallization reactor.

Name and Symbol	Dimension (m)
Tank diameter, T	0.0726
Impeller diameter, D	0.050
Liquid level, H	0.077275
Off-bottom clearance, C	0.010
Blade width, W_b	0.010
Tank radius, R_1	0.010
Tank radius, R_2	0.080
Shaft diameter, D_{shaft}	0.008
Hub height, H_{hub}	0.020
Hub diameter, D_{hub}	0.012
Blade thickness, e	0.004
Radial feed position, r_F	0.0307
Axial feed position, H_F	0.028875

6.1.2. Case Setup and Meshing

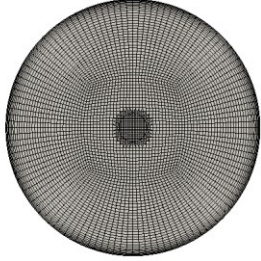
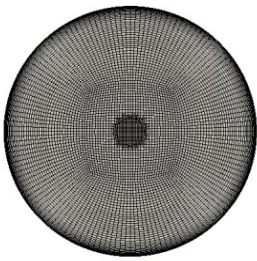
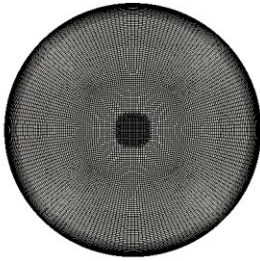
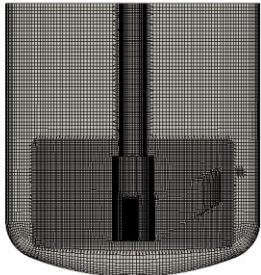


As outlined for the Chapple case in section 4.3.2, the tank and impeller geometries were modelled using the SALOME pre-processing platform (Salome Platform, n.d.). Meshing

was performed using a combination of tools available in SALOME and OpenFOAM. A structured background mesh was created for the tank without the impeller using SALOME. Subsequently, the OpenFOAM utility snappyHexMesh was used to cut out and conform the mesh to the impeller, which results in a hexahedral-dominant unstructured mesh.

As previously mentioned, the size of the rotating zone is somewhat arbitrary, but its dimensions should not impact the results. The size of rotating domain was chosen such that its boundary is halfway between the impeller tip and tank walls in the radial direction and at least 0.010 m above and below the impeller in the axial direction. This resulted in a diameter of 0.056 m and a height of 0.029 m for the zone. Only MRF simulations were performed for the stirred tank crystallization reactor cases. The rotating zone was therefore defined as a cellZone, and an appropriate volumetric force was applied to represent the rotation of the impeller. The OpenFOAM utility topoSet was used to add the feed as a cellZone, and corresponding mass and momentum sources were applied to represent the injection of reactants.

A mesh dependence study was performed for the stirred tank crystallization reactor case. The three computational meshes considered are summarized in Table 6.2. As for the Blais and Chapple cases in section 4.2.2 and 4.3.2, respectively, the meshes were generated by building a background mesh of 670 320 hexahedral cells for the Mid Mesh, a background mesh having 25% less for the Coarse Mesh, and a background mesh having 25% more cells for the Fine Mesh. As shown in Table 6.2, one level of local refinement was added for the rotating zone, around the impeller and shaft, and the feed addition point using the mesh cell splitting technique available in snappyHexMesh.

Table 6.2: Mesh quality for the stirred tank crystallization reactor case.

	Coarse Mesh	Mid Mesh	Fine Mesh
Mesh			
			
Number of 3D cells	1 038 169	1 724 661	3 578 480
Number of 3D hexahedral cells	1 026 217	1 708 077	3 551 889
Maximum aspect ratio	8.51435	10.4465	11.5738
Average non-orthogonality	7.22676	7.0898	6.88994
Maximum skewness	2.85	3.99	2.78
Minimum cell volume	$1.11 \times 10^{-11} \text{ m}^3$	$6.59 \times 10^{-12} \text{ m}^3$	$2.56 \times 10^{-12} \text{ m}^3$
Maximum cell volume	$1.28 \times 10^{-9} \text{ m}^3$	$7.26 \times 10^{-10} \text{ m}^3$	$3.63 \times 10^{-10} \text{ m}^3$
Total Volume	$292.95 \times 10^{-6} \text{ m}^3$	$292.99 \times 10^{-6} \text{ m}^3$	$293.03 \times 10^{-6} \text{ m}^3$
Rotating zone diameter	0.056 m	0.056 m	0.056 m
Rotating zone height	0.029 m	0.029 m	0.029 m
Average Courant Number	0.080	0.032	0.119
Maximum Courant Number	0.59	0.22	1.35

6.1.3. Case Setup

Boundary conditions for the flow simulations in the stirred tank crystallization reactor case are identical to those presented in Section 5.3.2 for the Assirelli et al. (2002) case and are summarized in Table 6.3. Initial conditions for reactive mixing solver are summarized in Table 6.4. Table 6.5 summarizes the initial values for the turbulence variable fields for each Reynolds number. Table 6.6 shows the liquid properties used for each simulation. Table 6.7 and Table 6.8 give the initial concentrations in the EasyMax reactor and injected acid with its corresponding reaction rate constant.

Table 6.3: Boundary conditions used for the steady-state incompressible flow cases.

Variable	Shaft	Impeller	Walls	Top
Velocity, U (m/s)	RotatingWall Velocity	MovingWall Velocity	noSlip	slip
Pressure, P (Pa)	zeroGradient	zeroGradient	zeroGradient	zeroGradient
Turbulent kinematic viscosity, ν_t (m ² /s)	nutkWall Function	nutkWall Function	nutkWall Function	calculated
Turbulent kinetic energy, k (m ² /s)	kLowReWall Function	kLowReWall Function	kLowReWall Function	zeroGradient
Turbulent energy dissipation, ε (m ² /s ³)	epsilonWall Function	epsilonWall Function	epsilonWall Function	zeroGradient

Table 6.4: Boundary and initial conditions used for the stirred tank crystallization reactor case.

Variable	Internal Field	impeller	shaft	Walls
Mixture fraction, α_1 (-)	uniformValue = 0	zeroGradient	zeroGradient	zeroGradient
Mixture fraction in environment 1, X_1 (-)	uniformValue = 0	zeroGradient	zeroGradient	zeroGradient
Mixture fraction in environment 2, X_2 (-)	uniformValue = 0	zeroGradient	zeroGradient	zeroGradient
Reaction progress in environment 1, Y_1 (-)	uniformValue = 0	zeroGradient	zeroGradient	zeroGradient
Reaction progress in environment 2, Y_2 (-)	uniformValue = 0	zeroGradient	zeroGradient	zeroGradient

Table 6.5: Initial field conditions specified for the stirred tank crystallization reactor case.

Reynolds number, $(\rho ND^2/\mu)$	Impeller speed, N (1/s)	Turbulent kinetic energy, k (m^2/s^2)	Turbulent energy dissipation, ε (m^2/s^3)
8 333	3.33	1.10×10^{-4}	3.05×10^{-4}
16 667	6.67	3.71×10^{-4}	1.88×10^{-4}
25 000	10.0	7.54×10^{-4}	5.46×10^{-3}

Table 6.6: Liquid properties used for the stirred tank crystallization reactor case.

Property	Value
Density, ρ (kg/m^3)	997
Dynamic viscosity, μ (Pa s)	0.89×10^{-3}
Turbulent Schmidt number, Sc_t	0.7
*Molecular diffusion coefficient, D_T (m^2/s)	1.0×10^{-9}

*Assumed value negligible compared to turbulent diffusion.

Table 6.7: Initial concentrations in the stirred tank crystallization reactor case.

Variable	Value
Concentration of injected acid, A_0 (H_2SO_4 mol/ m^3)	100, 150, 200, 300, 400 (See Table 3.2)
Concentration of borate ion, B_0 (H_2BO_3^- mol/ m^3)	90.9
Concentration of iodine ions, D_0 (mol/ m^3)	14
*Reaction rate constant, k_2 ($\text{m}^{12}/\text{mol}^4/\text{s}$)	See Eq. 3.66

*Note that the rate constant varies with ionic strength.

Table 6.8: Initial concentration of injected acid and source terms for each Reynolds number used in the stirred tank crystallization reactor cases.

Reynolds number, ($\rho ND^2/\mu$)	Concentration A_0 (mol/m^3)	*Velocity, u_z (m/s)	Volumetric Source (m^3/s)
16 667	50	-0.017	3.33×10^{-8}
8 333	100	-0.034	6.67×10^{-8}
16 667	100	-0.034	6.67×10^{-8}
25 000	100	-0.034	6.67×10^{-8}
8 333	150	-0.017	3.33×10^{-8}
16 667	150	-0.017	3.33×10^{-8}
25 000	150	-0.017	3.33×10^{-8}
8 333	200	-0.017	3.33×10^{-8}
16 667	200	-0.017	3.33×10^{-8}
25 000	200	-0.017	3.33×10^{-8}
8 333	300	-0.017	3.33×10^{-8}
16 667	300	-0.017	3.33×10^{-8}
25 000	300	-0.017	3.33×10^{-8}
8 333	400	-0.017	3.33×10^{-8}
16 667	400	-0.017	3.33×10^{-8}
25 000	400	-0.017	3.33×10^{-8}

*Negative indicates downward injection.

6.2. Results and Discussion

6.2.1. Yield in Mixing Sensitive Reactions

Figure 6.2 shows predicted segregation index as a function of injected acid concentration for fixed stir speeds. The engulfment parameter was evaluated using averaged variance weighted turbulence variables outlined in Chapter 3. Model trend predictions for the implemented E-model and DQMOM-IEM are in good agreement with experimental data. For each stir speed tested, as concentration of feed increases, the system moves through various levels of kinetic limitations. As confirmed through Figure 6.2, yield of the second reaction increases with increasing feed concentration, effectively pushing the system closer to kinetic controlled when compared to the mixing rate because the reaction rate increases with acid concentration. This is because as k_2 increases relative to a fixed mixing rate (stir speed), the rate of the iodide-iodate reaction rate becomes comparable to that of the instantaneous reaction. For an increase in stir speed, yield of the second reaction decreases, hinting that the system becomes more mixing limited. The increase in stir speed increases the mixing rate and mixing uniformity, leading to higher local energy dissipation rates that causes reactants to come in contact faster at the molecular level. Both DQMOM-IEM and

E-model predictions replicate the s-shaped function as confirmed in Figure 6.2 (top right). The DQMOM-IEM model predictions appear dampened when compared to E-model predictions. Similar to the Akiti and Armenante case in Chapter 5, E-model predictions tend to overpredict X_S at low Reynolds numbers and agree more closely with experimental measurements as Reynolds number increases. Differences in model predictions are likely due to the handling of local and averaged turbulent energy dissipation rates.

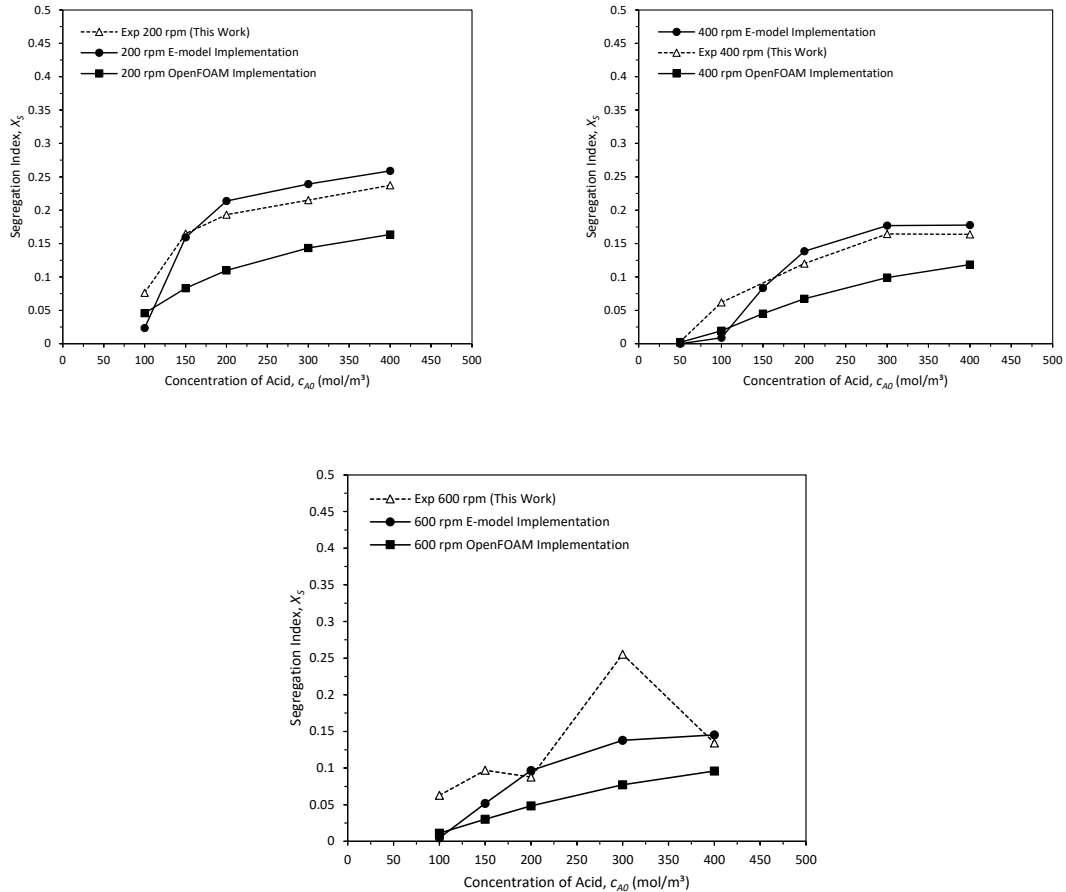


Figure 6.2: Comparisons between the experimental and simulated segregation index values for the crystallization stirred tank with varying injection acid concentration for $Re = 8333$ (top left), $Re = 16667$ (top right), and $Re = 25000$ (bottom) for the intermediate mesh summarized in Table 6.2.

A sensitivity study was performed to characterize the impact of varying Courant number on predicted segregation index by varying fixed time steps between 1×10^{-3} and 1×10^{-5} s, as summarized in Figure 6.3. The case was selected to represent the middle stir speed

and the middle concentration. The variance weighted turbulence parameters used as input for the E-model were found to not change with respect to Courant number, which leads to negligible changes in X_S as Courant number decreases. Segregation index calculated using the DQMOM-IEM model also stays constant with decreasing Courant numbers. The smaller time steps act as an effective relaxation on the mixture fraction variables. Duan et al. (2016) performed simulations using run time adjustable time stepping initially set to 1×10^{-4} s. Marchisio (2009) follow similar methodology using time steps ranging from 1×10^{-4} to 5×10^{-5} s for LES simulations. In this work, simulations using time steps of 1×10^{-3} s lead to poor convergence on mixture fraction variables compared to 1×10^{-4} s. Taken together, the overall impact of time stepping does not influence the results over the range of 1×10^{-4} – 5×10^{-5} s, but convergence requires time steps smaller than approximately 1×10^{-4} s.

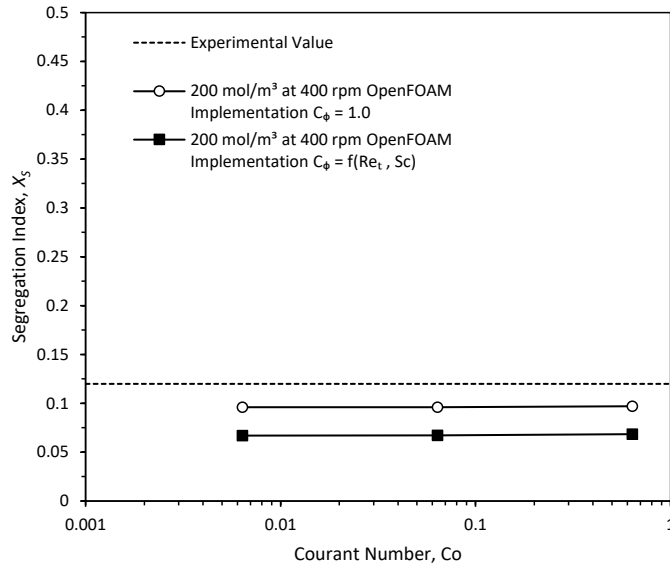


Figure 6.3: Impact of varying Courant number on segregation index in the stirred tank crystallization reactor case using the intermediate mesh shown in Table 6.2. Reynolds number of 16 667 and acid concentration of 200 mol/m^3 .

6.2.2. Mesh Dependence Study in Crystallization Reactors

A mesh dependence study was performed for the three meshes summarized in Figure 6.4. The 600 rpm stirring speed was tested with an acid injection concentration of 400 mol/m^3 to study the impact of mesh resolution on segregation index estimates. Figure 6.4 shows

the predicted segregation index varying with the number of mesh cells. It is clear that the segregation index is slightly underpredicted at low mesh resolution and stays relatively constant with an increase in resolution. E-model predictions are stable throughout the range of grids tested. This analysis has not been reported in literature, but it is well known that energy dissipation rate based power numbers underpredict experimental results and are improved by increasing mesh resolution. It is somewhat surprising that segregation index is less sensitive to mesh resolution since it is based on energy dissipation rate.

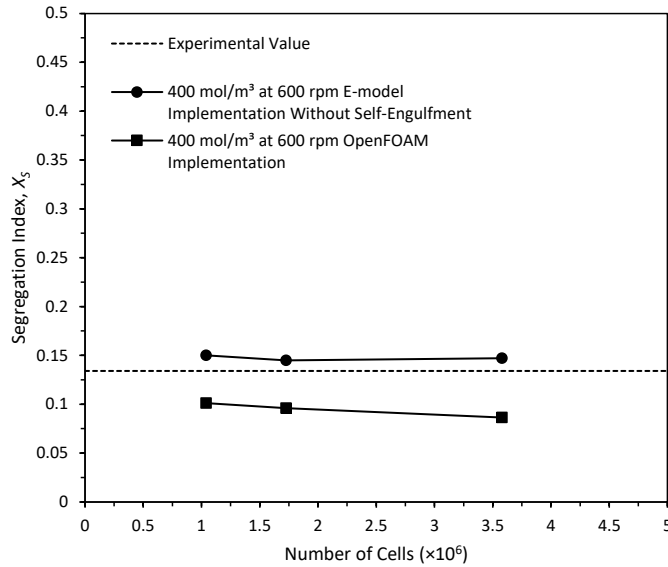


Figure 6.4: Impact of varying cell number on segregation index in the stirred tank crystallization reactor case using the meshes shown in Table 6.2. Reynolds number of 16 667 and acid concentration of 400 mol/m³.

Table 6.9 outlines the impact of grid size on segregation index for each mesh used in the mesh sensitivity study. The computational grids are summarized in Table 6.2. As seen in Table 6.9, X_S evaluated using the DQMOM-IEM model shows a slightly decreasing trend with increasing grid size. Model predictions from the E-model are proportional to the variance weighted turbulent energy dissipation rate as expected.

Table 6.9: Impact of grid size on segregation index for $Re = 25000$ and $C_{A0} = 400$ mol/m³ using each mesh summarized in Table 6.2.

Mesh	Variance-Weighted ϵ_R (m ² /s ³)	Variance-Weighted k_R (m ² /s ²)	Segregation Index from OpenFoam X_S	Segregation Index from E-model
Coarse	1.3779	0.0436	0.010	0.150
Mid	1.6110	0.0465	0.096	0.145
Fine	1.5254	0.0475	0.086	0.147

6.2.3. Mixing times

Blend times in the EasyMax 402 stirred tank reactor were determined for stir speeds of 50, 100, 200, 400, 600, and 800 rpm ($Re = 2\,083\text{--}33\,333$), as shown in Figure 6.5 using the intermediate mesh summarized in Table 6.2. Blend time was evaluated by injection of a passive non-reacting tracer into the fluid. Blend time is taken as the time required for the global coefficient of variation (COV) to stabilize at 5%. Other methods have been employed to calculate blend time, such as monitoring several probe locations. The advantage of monitoring COV across the full domain is that it guarantees that all fluid element regions have completely mixed.

Figure 6.5 shows a comparison between the empirical correlation of Grenville (1992) with blend time predicted by the DQMOM-IEM model. Over the range of Reynolds numbers tested, blend time is linear between $Re = 2083$ and $25\,000$. Around $Re = 33\,333$ and above, the system begins to behave nonlinearly, where increasing stir speed begins to influence the bulk blending less. At the highest Reynolds number, blend time was found to be 0.96 s, which is approximately one order of magnitude larger than the lowest 200 rpm t_{SSS} .

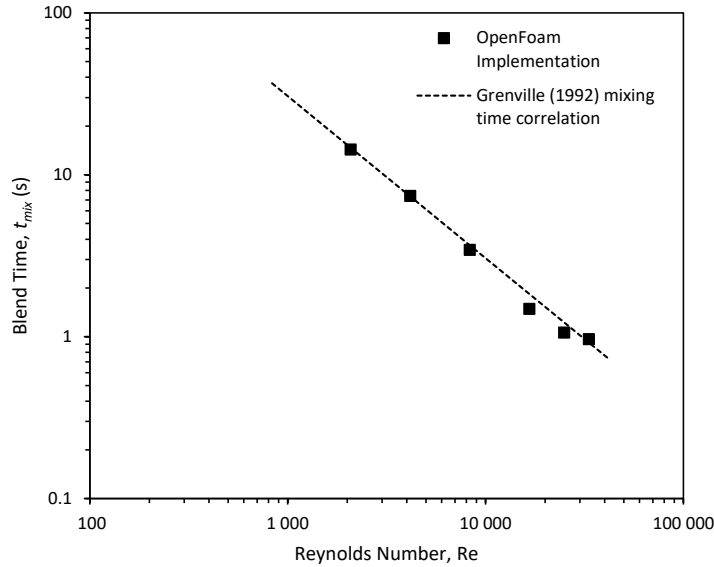


Figure 6.5: Impact of varying Reynolds number on global blend time in the stirred tank crystallization reactor case using the intermediate mesh shown in Table 6.2. Simulations performed over the range of Reynolds number of 2 083–33 333, corresponding to stirring speeds of 50, 100, 200, 400, 600, and 800 rpm.

Figure 6.6 presents the distribution of t_{SSS} at Reynolds numbers of 8333, 16667, and 25000. The distributions show a log-normal distribution spanning 1–3 orders of magnitude. As expected and confirmed in Figure 6.6, the average mixing time decreases as stir speed increases. The distributions show broadening as stir speed increases indicating regions of non-uniform mixing and large gradients in velocity.

The mean mixing times were evaluated for the EasyMax reactor as a volume-weighted mean of t_{SSS} and as a variance-weighted mean to represent the reaction zone as shown in Figure 6.7. For the volume-weighted mean values of t_{SSS} , the energy dissipation is taken as the volume-integral of turbulent energy dissipation rate of the whole tank. For the variance-weighted mean of t_{SSS} , the energy dissipation is taken as the variance-weighted turbulent energy dissipation rate. The mixing time in the reaction zone was calculated according to the following expression:

$$t_{mix} = \frac{\sum(a_2 t_{SSS})}{\sum(a_2)} \quad (6.1)$$

The mixing times are validated by comparison to the commonly cited reduced-order mixing model of Bourne and Baldyga (1989). Bourne and collaborators related mixing time as being inversely proportional to the power dissipation. The following empirical correlation relates the mixing time to the energy dissipation:

$$t_{mix} = 17.2(\nu/\varepsilon)^{0.5} \quad (6.2)$$

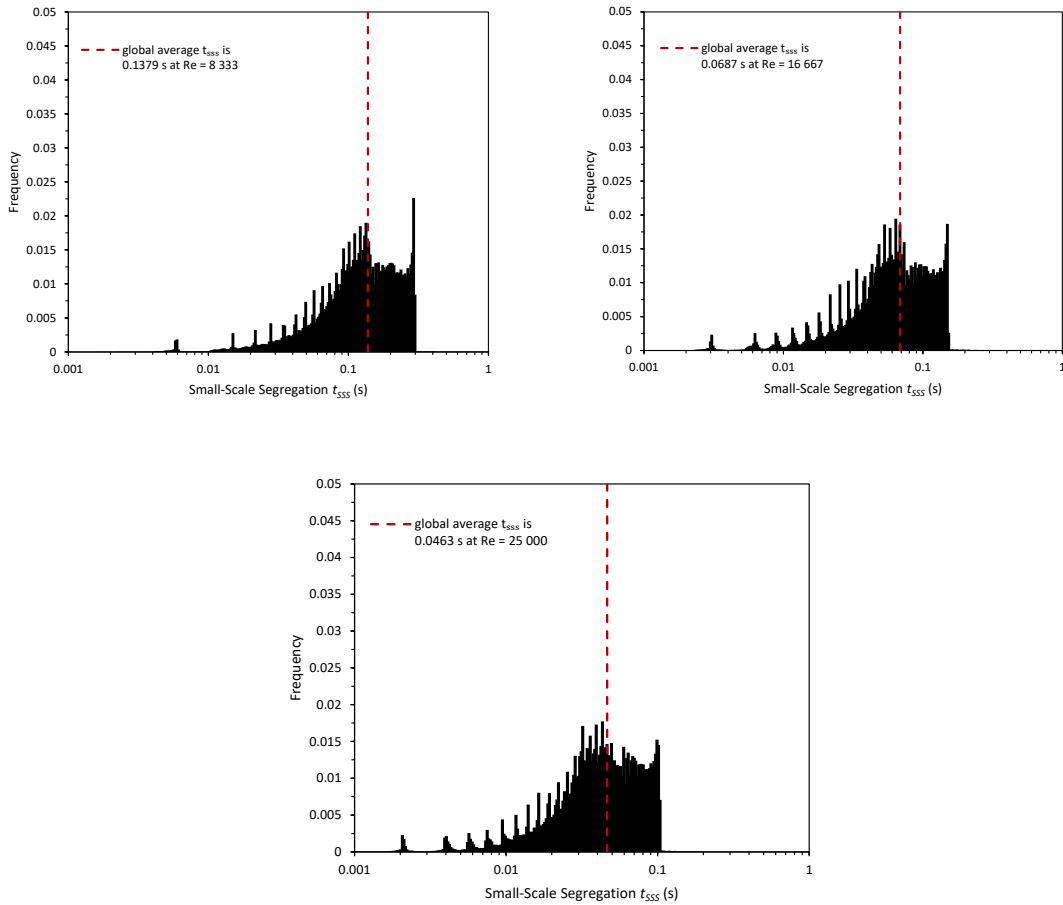


Figure 6.6: Small-scale segregation mixing time t_{SSS} for $Re = 8\,333$, $16\,667$, and $25\,000$ with the intermediate mesh.

The mixing time data shown in Figure 6.7 is in reasonable agreement with the model of Bourne and Baldyga. As expected, mixing times evaluated over the entire tank tend to be higher than mixing times evaluated in the reacting zone. This is due to the non-uniform mixing rate when averaging over the full domain. In the reaction zone, mixing and dissipation is localized because it is close to the high energy dissipation at the impeller. Although the slope from the two averaging schemes are similar, the slope from CFD

predictions is higher compared to the reduced order model. Bourne and collaborators derived the empirical correlations from experimental data collected for a mixing sensitive reaction scheme.

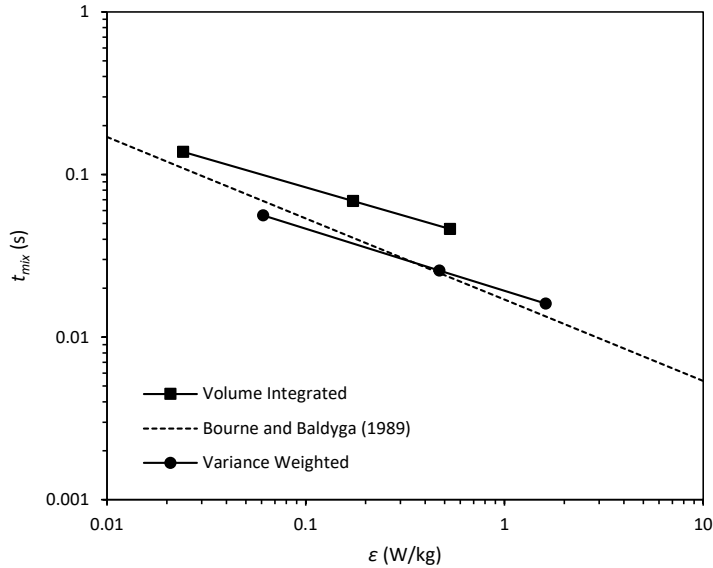


Figure 6.7: DQMOM-IEM predictions of the mean mixing time as a function of average energy dissipation compared to the reduced order model of Bourne and Baldyga (1989).

The simulation data presented here offers a unique methodology to aid scale-up when geometric similarity is not possible. Future work should focus on scale-up of the proposed two-step procedure. First, match global blend times in small-scale and large-scale stirred tank reactors to determine the equivalent impeller. Second, tune dosing location to match the distribution of local t_{SSS} . This ensures proper mixing uniformity between reactors. More information related to this proposed scale-up strategy using local parameters is outlined in section 6.2.4. The evaluation of mixing times outlined in section 3.8 can become challenging due to the underlying physics. As bulk blending is achieved, a_1 approaches zero in Eq. (3.92). Marchisio and Fox and colleagues determine t_{SSS} by volume averaging over the full domain. The E-model provides a convenient way to rapidly apply local averaging.

6.2.4. Reaction Zone

Figure 6.8 and Figure 6.9 shows a sensitivity analysis of the distribution of energy dissipation in the reaction zone for the crystallization reactor case at different Reynolds numbers and variance cut-off values. The results presented are for $Re = 16667$ and $Re = 25000$ and use the intermediate mesh summarized in Table 6.2. As seen in Figure 6.8, the size of the reaction zone generally decreases with increasing Re for a given variance cut-off value. Additionally, for fixed Re , decreasing variance ratio increases the volume in consideration, and in turn determines the range of energy dissipation in the reacting zone. A visual example of this is summarized in Figure 6.9, where the bigger reaction zones display a broadened log-normal distribution.

Following this definition for reaction zone using variance ratios $a_2/a_{2,max} \geq 1 \times 10^{-3}$ – 1×10^{-6} makes it challenging to analyze the results in terms of a local energy dissipation. Ideally, scale-up procedures can be made easier by linking local values to global values. Therefore, an alternative approach is proposed to represent the volume/visual reacting zone by matching the local average energy dissipation inside the volume with the global average energy dissipation of the whole tank. These distributions are displayed in Figure 6.10. The averages are summarized in Table 6.10. Although the average energy dissipation is roughly equal, the distributions differ in the lower energy dissipation rate range for each stir speed, as seen in Figure 6.10. The higher range of energy dissipation is more impactful on the average dissipation and the two curves for each stir speed overlap for approximately one order of magnitude.

From a scale-up perspective, matching local energy dissipation with global offers a theoretical way to scale-up. This is analogous to matching the bulk blend time with the local small-scale mixing time as described in the previous section 6.2.3. In this way, scale-up of liquid mixing with geometrically non-similar impeller and tank geometry can be made easier by manipulating as little as two variables: stir speed and feed location. Impeller speed is determined by matching global blend times, followed by adjusting feed location to match local small-scale mixing time with the blend time.

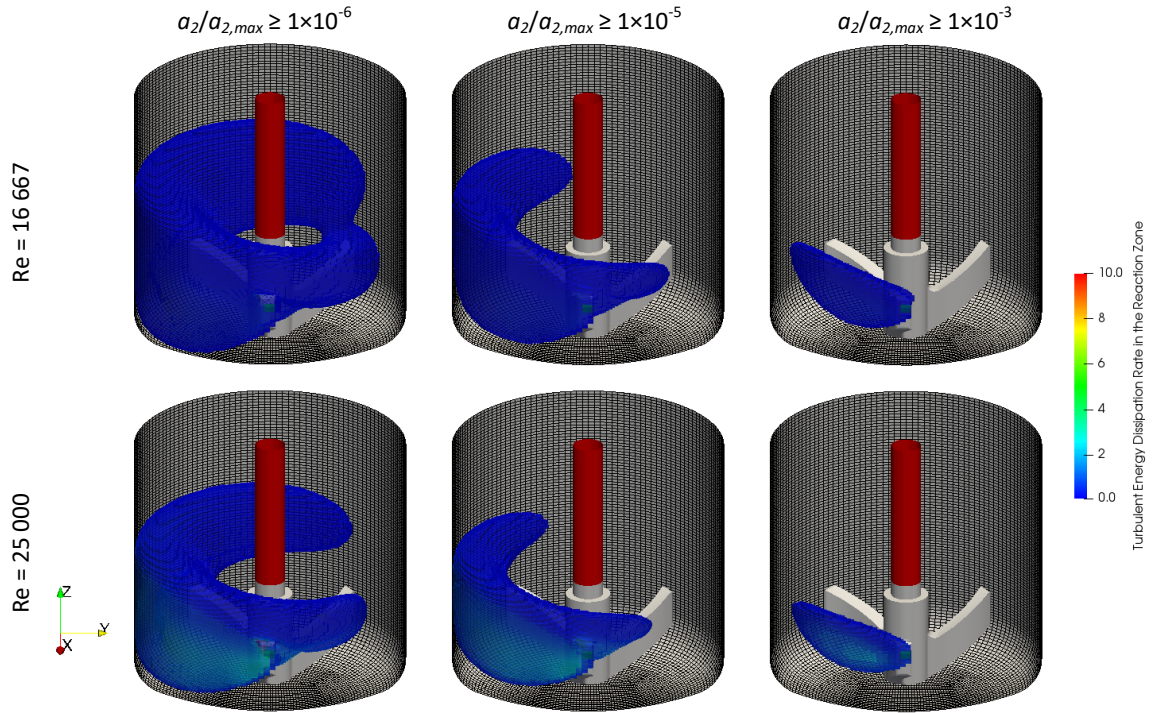


Figure 6.8: Turbulent energy dissipation rate distribution in the reaction zone for the crystallization reactor case for variance ratio 1×10^{-6} at $Re = 16\,667$ (top left), variance ratio 1×10^{-5} at $Re = 16\,667$ (top middle), variance ratio 1×10^{-3} at $Re = 16\,667$ (top right), variance ratio 1×10^{-6} at $Re = 25\,000$ (bottom left), variance ratio 1×10^{-5} at $Re = 25\,000$ (bottom middle), and variance ratio 1×10^{-3} at $Re = 25\,000$ (bottom right). All simulations use the intermediate mesh.

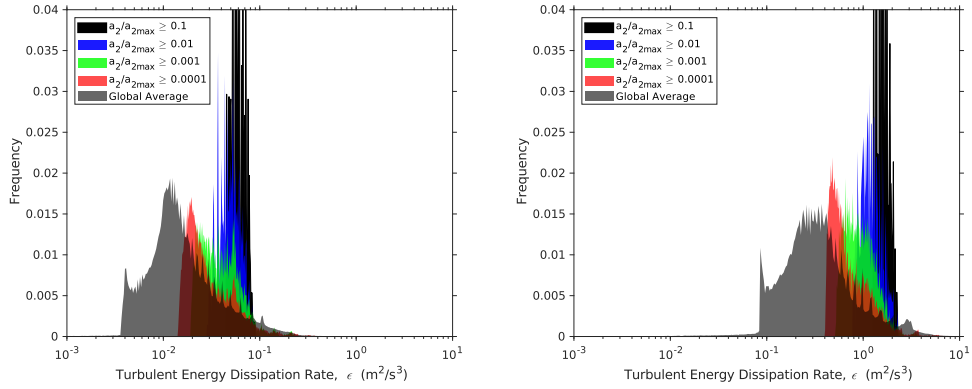


Figure 6.9: Turbulent energy dissipation rate distribution for the crystallization reactor case averaged over the full tank (transparent black), averaged over the reaction zone using a variance ratio of 1×10^{-4} (red), averaged over the reaction zone using a variance ratio of 1×10^{-3} (green), averaged over the reaction zone using a variance ratio of 1×10^{-2} (blue), averaged over the reaction zone using a variance ratio of 1×10^{-1} (solid black). Reynolds number $Re = 8\,333$ (200 rpm left) using intermediate mesh. Reynolds number $Re = 25\,000$ (600 rpm right) using intermediate mesh.

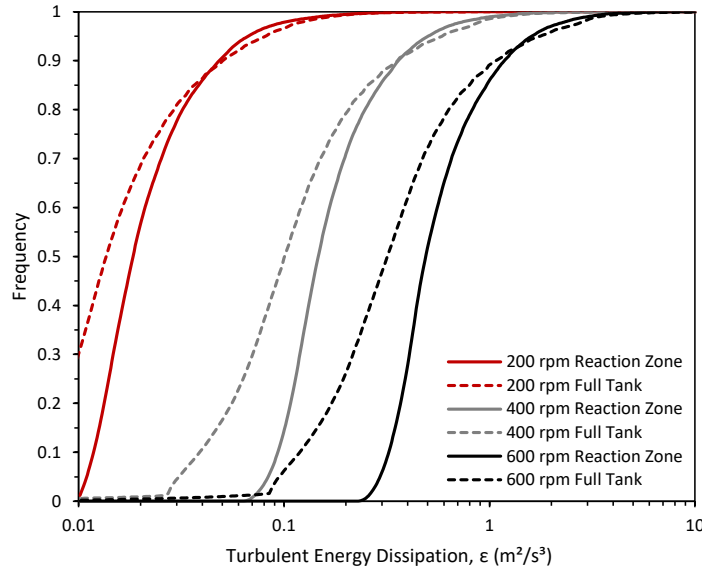


Figure 6.10: Turbulent energy dissipation rate distribution for the crystallization reactor case averaged over the full tank and averaged over the reaction zone by matching variance ratio. Reynolds number $Re = 8\,333$ (200 rpm), $16\,667$ (400 rpm) and $25\,000$ (600 rpm) using intermediate mesh.

Table 6.10: Segregation zone impact on mean energy dissipation rate for $Re = 8333$ – 25000 and $C_{A0} = 400 \text{ mol/m}^3$ with various cut-off variance ratio on the intermediate mesh.

Reynolds Number, Re	Average Energy Dissipation using $a_2/a_{2,max} \geq 0.1 \text{ (m}^2/\text{s}^3)$	Average Energy Dissipation using $a_2/a_{2,max} \geq 0.01 \text{ (m}^2/\text{s}^3)$	Average Energy Dissipation using $a_2/a_{2,max} \geq 0.001 \text{ (m}^2/\text{s}^3)$	Average Energy Dissipation using $a_2/a_{2,max} \geq 0.0001 \text{ (m}^2/\text{s}^3)$	Variance-Weighted Average Energy Dissipation $\epsilon_R \text{ (m}^2/\text{s}^3)$	Average Energy Dissipation of Tank $\text{(m}^2/\text{s}^3)$
8 333	0.061	0.050	0.043	0.036	0.061	0.024
16 667	0.472	0.376	0.316	0.265	0.471	0.173
25 000	1.619	1.247	0.990	0.819	1.611	0.532

* $k_R = 0.0055 \text{ m}^2/\text{s}^2$ for 200 rpm, $k_R = 0.0208 \text{ m}^2/\text{s}^2$ for 400 rpm, $k_R = 0.0465 \text{ m}^2/\text{s}^2$ for 600 rpm

6.2.5. Time Dependent Measurements

Segregation index varying with respect to time is given in Figure 6.11. Measurements collected in this work are compared with predictions made by the E-model without self-engulfment. E-model predictions for a given time point in experiments are represented by the amount of volume injected at the given time. Figure 6.11 (top left) shows time dependent data for the 200 mol/m^3 at 200 rpm case. Segregation index measurements begin to decrease after 6 minutes, caused by concentration of triiodide ion extending higher than the calibration range where Beers Law no longer applies. Average segregation index for these experiments are taken to be the values that lie in the calibration range. E-model predictions are generally in good agreement with experimental measurements. As expected, predictions tend to better match experiments at the higher Reynolds numbers, as displayed in Figure 6.11 (top right and bottom).

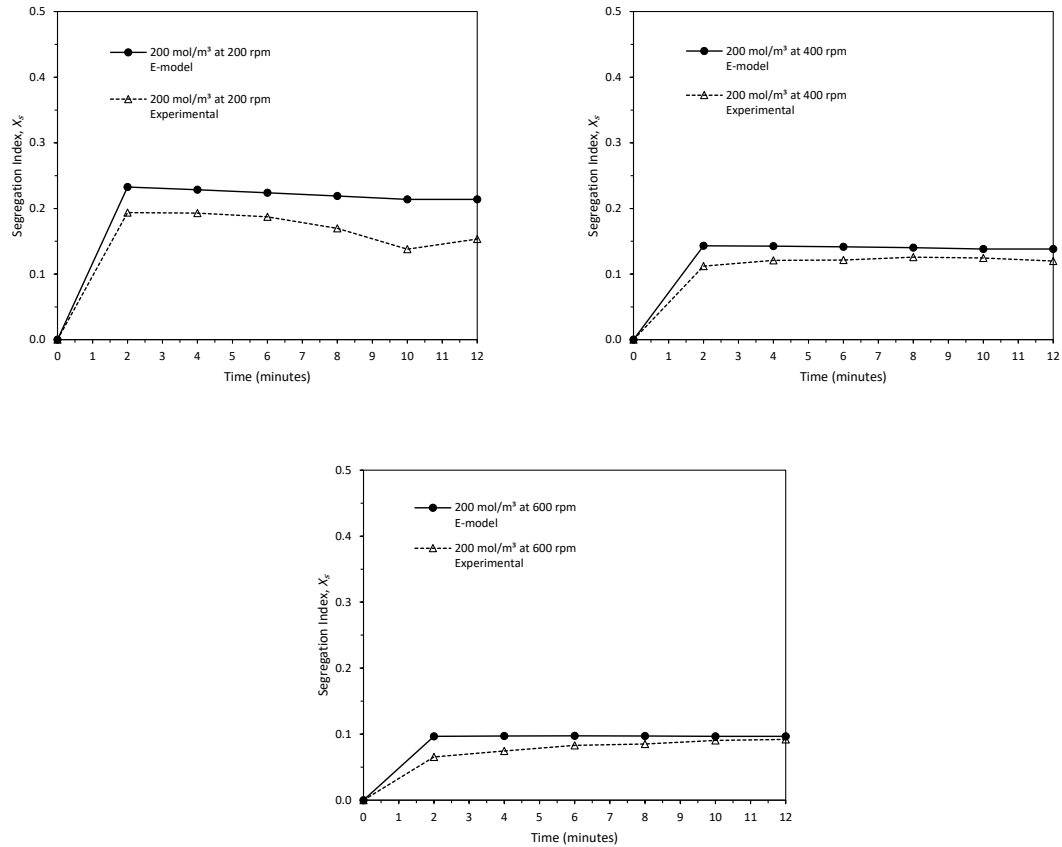


Figure 6.11: Segregation index varying as a function of crystallization reactor case using the intermediate mesh summarized in Table 6.2.

6.2.6. Sensitivity to Mixing Parameters

A comparison of self-engulfment and non self-engulfment E-model predictions of segregation index as a function of acid injection concentrations is given in Figure 6.12. This was done to test model sensitivity. The vertical shift in yield predictions that result from the self-engulfment model suggests blending is having an impact on reaction yield.

The empirical mixing coefficient C_ϕ that describes the mechanical-to-scalar-time-scale ratio directly influences the micromixing time parameter γ (s^{-1}) and the micromixing rate. The dependence of the predicted segregation index X_S on the empirical mixing coefficient C_ϕ for various acid injection concentrations is given in Figure 6.13. Each simulation was performed at a fixed stir speed of 400 rpm ($Re = 16\,667$). Trends of decreasing C_ϕ leading to an increase in X_S are consistent with literature investigations (Marchisio and Barresi, 2003). Under fully turbulent conditions, $C_\phi \approx 2.0$ is commonly used. If flow conditions are

not fully turbulent, $C_\phi \approx 2.0$ will overestimate the micromixing rate. Overestimating micromixing rate leads to an underestimate in X_S due to an artificially higher local mixing rate. Figure 6.13 shows X_S is almost identical for $C_\phi = 2.0$ and C_ϕ modelled as a function of the local Reynolds number, indicating C_ϕ is better suited for higher Reynolds numbers. Future work should focus on characterizing C_ϕ for lower Reynolds numbers as stirred tank reactor crystallization processes are often performed at lower impeller speed and higher fluid viscosity. Literature investigations focused on batch injection systems have used a range of approaches to model C_ϕ . The deviation in values suggest this constant is not well established for these systems. For example, Marchisio and Barresi (2003) used a constant value of $C_\phi = 1.0$ when simulating Villermaux-Dushman reactions in a Taylor-Couette reactor. Cheng et al. (2016) applied a constant value of $C_\phi = 0.5$ to study reactive precipitation in a liquid-liquid stirred tank reactor having volume of 10.9 L and Reynolds number range of 45 000 to 50 000. Although high Reynolds numbers, specific reaction kinetics in the reactive precipitation could explain the need for a low C_ϕ . Understanding this relationship should be investigated in future work.

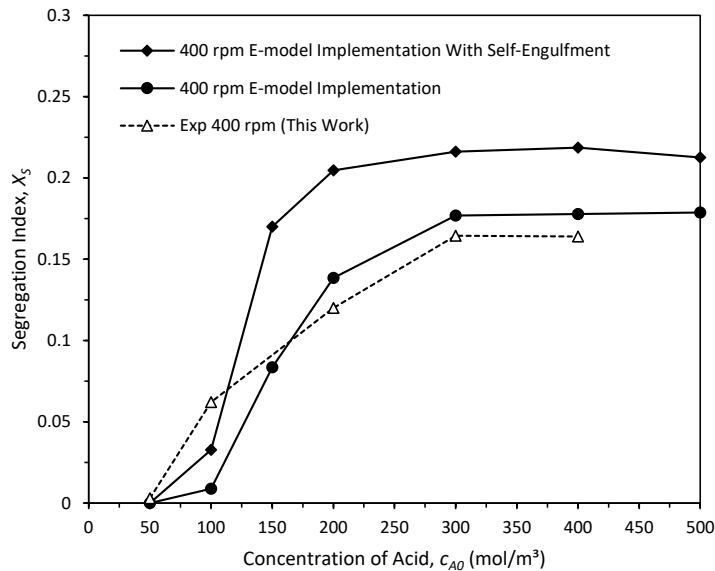


Figure 6.12: Effect of E-model predictions with and without self-engulfment on predicted segregation index X_S for Reynolds number $Re = 16\,667$ (400 rpm).

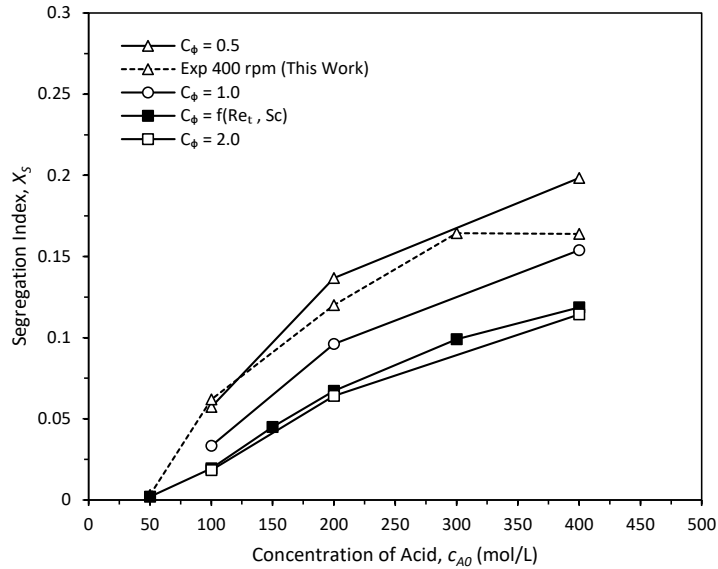


Figure 6.13: Effect of empirical mixing coefficient C_ϕ on predicted segregation index X_S for Reynolds Number $Re = 16\,667$.

6.3. Summary

Yield of Villermaux-Dushman reactions was investigated using the DQMOM-IEM and E-model solvers in a common small-scale crystallization reactor. The results suggest that these methods can be used to estimate the selectivity of these reactions well, which implies a good estimate of micromixing. It is recommended that scale-up procedures where reactor and impeller geometries cannot be maintained perfectly geometrically similar focus on maintaining approximately the same blend time and the same local mixing time in the impeller region. Maintaining similar local mixing times in the impeller region can be achieved through CFD simulation of an injected tracer. The effect of C_ϕ on CFD predictions was shown to be significant and should be further investigated at low Reynolds numbers due to the relevance in crystallization processes. The determination of this parameter should be further investigated for the type of small-scale stirred tank investigated in this study.

CHAPTER 7: CONCLUSIONS AND RECOMMENDATIONS

7.1. Conclusions

Simulation of mixing is important in many industrial applications. In crystallization processes, micromixing is a critical factor that impacts product quality. In this study, a DQMOM-IEM solver was developed in OpenFOAM to simulate fluid dynamics and competitive-parallel reaction yield. The CFD solver was also coupled to an E-model as an alternative method to predict competitive-parallel reaction yield. The fluid dynamics predictions of the CFD method were validated through comparison to power number and velocity profile data for two small-scale stirred tanks taken from the literature. The reactive CFD solver was validated by comparing simulation results with experimental data from the literature for one CIJR and two stirred tank reactor cases. The reactive CFD methods were then compared to experimental data collected in the present work.

To test fluid flow and turbulence predictions in stirred tank reactors, validation cases based on the experiments performed by Chapple et al. (2002) were simulated. The simulation and experimental results from Blais et al. (2016) were used to verify impeller motion modelling techniques. These validation cases simulated power number and local velocity profiles using the steady-state incompressible flow solver with k - ϵ turbulence modelling. Flow conditions were chosen such that Reynolds numbers ranged from laminar to turbulent. Two impeller types (pitched blade impeller and Rushton turbine) were studied to investigate the effects of geometry on power number. Various meshing strategies were used to test mesh dependence. Two different impeller motion models (sliding mesh and MRF) were applied to test the impact of transient and steady-state simulations on power number predictions. Comparison between sliding mesh and MRF techniques showed that results for power number did not significantly affect global turbulent kinetic energy dissipation rate. The results for different impellers were in good agreement when compared to experimental data. Local velocities were captured using the CFD solver for the pitched blade impeller. The results for the mesh dependence study underpredicted power number based on turbulent kinetic energy dissipation rate but improved with increasing number of volume

cells. Power number based on impeller torque remained unchanged with increasing mesh resolution. Overall, the predicted power number and local velocity profiles are in good agreement with experimental data.

Micromixing performance and competitive-parallel reactions were investigated in a small-scale stirred tank crystallization reactor and various larger-scale stirred tank reactors using a DQMOM-IEM OpenFOAM solver. Early model development in a CIJR was based on experiments performed by Johnson and Prud'homme (2003) and simulations conducted by Liu and Fox (2006). Validation cases based on experiments in larger-scale stirred tank reactors conducted by Assirelli et al. (2002) and Akiti and Armenante (2004). Simulation results from Duan et al. (2016) and Liu and Fox (2006) were used to verify the reactive solver predictions. Mesh dependence studies were performed on all simulation cases. The mesh dependency study showed reaction rates are impacted by number of cell volumes. The OpenFOAM solver tends to underpredict reaction rates of the slower reaction. Qualitative trends of selectivity are in good agreement with theory and experiments for both CIJR and stirred tank reactors.

Small-scale stirred tank crystallization reactors were investigated both experimentally and using simulation. The Villermaux-Dushman reactions were used by varying initial feed reactant concentration and impeller speed to characterize mixing rate and reaction rate independently for a small-scale 300 mL EasyMax stirred tank reactor. These experimental data was used as a direct comparison with simulation reaction yield results. Common literature post-processing techniques were used to analyze simulation results, such as the E-model of Bourne and Baldyga (1990). The analysis was extended by considering distributions of turbulent kinetic energy dissipation rate and micromixing rates. Overall, model predictions are in good agreement with experimental data. However, predictions were found to be impacted by mesh resolution and therefore care should be taken. Model predictions were found to be significantly impacted by the empirical micromixing rate constant, which has previously been used as a tuning parameter that can result in a better fit when compared to experimental data.

One of the main limitations to the implemented model is that it does not consider free surface effects. This can lead to error in systems operating without the use of baffles. Additionally, the turbulence modelling approach could be further expanded by transitioning from RANS based modelling to LES simulations. Further, a fully transient model requires the use of sliding mesh techniques coupled with time dependent LES turbulence modelling. This work avoided the use of these techniques due to the significant computational resources required in these simulations and less relevant to industry.

7.2. Future Work

For future work, more yield data should be gathered for different reactor scales with both geometric similarity and for non-similar geometries. More simulations should be done testing the suggested scale-up method of matching blend time with local mixing rates using the gathered data on similar and non-similar geometries. These simulations should be validated with either literature examples or gathered yield data. Further, a detailed investigation of the impact of empirical mixing coefficient on reaction yield should be performed. As discussed in section 6.2.3 and 6.2.4, this empirical mixing coefficient seems less established for low Reynolds numbers and could be integrated with the specific reaction kinetics used.

REFERENCES

- Akiti, O., & Armenante, P. M. (2004). Experimentally-validated micromixing-based CFD model for fed-batch stirred-tank reactors. *AIChE Journal*, *50*(3), 566–577. <https://doi.org/10.1002/aic.10051>
- Arian, E., & Pauer, W. (2021a). Contributions to the kinetics of the iodide–iodate test reaction for micromixing time calculation with extended incorporation models. *Chemical Engineering Science*, *237*, 116549. <https://doi.org/10.1016/j.ces.2021.116549>
- Arian, E., & Pauer, W. (2021b). Contributions to the kinetics of the iodide–iodate test reaction for micromixing time calculation with extended incorporation models. *Chemical Engineering Science*, *237*, 116549. <https://doi.org/10.1016/j.ces.2021.116549>
- Assirelli, M., Bujalski, W., Eaglesham, A., & Nienow, A. W. (2002). Study of micromixing in a stirred tank using a Rushton turbine: Comparison of feed positions and other mixing devices. *Chemical Engineering Research and Design*, *80*(8), 855–863. <https://doi.org/10.1205/026387602321143390>
- Baldyga, J., & Bourne, J. R. (1989). Simplification of micromixing calculations. I. Derivation and application of new model. *The Chemical Engineering Journal*, *42*(2), 83–92. [https://doi.org/10.1016/0300-9467\(89\)85002-6](https://doi.org/10.1016/0300-9467(89)85002-6)
- Baldyga, J., & Bourne, J. R. (1999). *Turbulent Mixing and Chemical Reactions* (1st ed.). John Wiley & Sons.
- Baldyga, J., Bourne, J. R., & Hearn, S. J. (1997). Interaction between chemical reactions and mixing on various scales. *Chemical Engineering Science*, *52*(4), 457–466. [https://doi.org/10.1016/S0009-2509\(96\)00430-7](https://doi.org/10.1016/S0009-2509(96)00430-7)

- Baldyga, J., Bourne, J. R., & Walker, B. (1998). Non-isothermal micromixing in turbulent liquids: theory and experiment. *Canadian Journal of Chemical Engineering*, 76(3), 641–649. <https://doi.org/10.1002/cjce.5450760336>
- Bałdyga, J., Makowski, Ł., & Orciuch, W. (2005). Interaction between Mixing, Chemical Reactions, and Precipitation. *Industrial & Engineering Chemistry Research*, 44(14), 5342–5352. <https://doi.org/10.1021/ie049165x>
- Bałdyga, J., & Pohorecki, R. (1995). Turbulent micromixing in chemical reactors — a review. *The Chemical Engineering Journal and the Biochemical Engineering Journal*, 58(2), 183–195. [https://doi.org/10.1016/0923-0467\(95\)02982-6](https://doi.org/10.1016/0923-0467(95)02982-6)
- Baqueiro, C., Ibaseta, N., Guichardon, P., & Falk, L. (2018a). Influence of reagents choice (buffer, acid and inert salt) on triiodide production in the Villermaux–Dushman method applied to a stirred vessel. *Chemical Engineering Research and Design*, 136, 25–31. <https://doi.org/10.1016/j.cherd.2018.04.017>
- Baqueiro, C., Ibaseta, N., Guichardon, P., & Falk, L. (2018b). Influence of reagents choice (buffer, acid and inert salt) on triiodide production in the Villermaux–Dushman method applied to a stirred vessel. *Chemical Engineering Research and Design*, 136, 25–31. <https://doi.org/10.1016/j.cherd.2018.04.017>
- Besten, M. (2021). *Experimental and Numerical Investigations on the Effects of Turbulent Boundary Layers on Micromixing Efficiency in a rotor-stator Spinning Disc Reactor*. Eindhoven University of Technology.
- Blais, B., Lassaigne, M., Goniva, C., Fradette, L., & Bertrand, F. (2016). A semi-implicit immersed boundary method and its application to viscous mixing. *Computers & Chemical Engineering*, 85, 136–146. <https://doi.org/10.1016/j.compchemeng.2015.10.019>
- Bourne, J. R. (2003). Mixing and the selectivity of chemical reactions. *Organic Process Research and Development*, 7(4), 471–508. <https://doi.org/10.1021/op020074q>

- Bourne, J. R. (2008). Comments on the iodide/iodate method for characterising micromixing. *Chemical Engineering Journal*, 140(1–3), 638–641. <https://doi.org/10.1016/j.cej.2008.01.031>
- Bourne, J. R., & Baldyga, J. (1990). The effect of micromixing on parallel reactions. *Biotechnology and Bioengineering*, 45(4), 907–918. <https://doi.org/10.1002/bit.260110206>
- Bourne, J. R., & Yu, S. (1994). Investigation of Micromixing in Stirred Tank Reactors Using Parallel Reactions. *Industrial and Engineering Chemistry Research*, 33(1), 41–55. <https://doi.org/10.1021/ie00025a007>
- Chapple, D., Kresta, S. M., Wall, A., & Afacan, A. (2002). The effect of impeller and tank geometry on power number for a pitched blade turbine. *Chemical Engineering Research and Design*, 80(4), 364–372. <https://doi.org/10.1205/026387602317446407>
- Cheng, D., Feng, X., Yang, C., & Mao, Z. S. (2016). Modelling and experimental investigation of micromixing of single-feed semi-batch precipitation in a liquid-liquid stirred reactor. *Chemical Engineering Journal*, 293, 291–301. <https://doi.org/10.1016/j.cej.2016.02.064>
- Cheng, D., Wang, S., Yang, C., & Mao, Z. S. (2017). Numerical Simulation of Turbulent Flow and Mixing in Gas-Liquid-Liquid Stirred Tanks. *Industrial and Engineering Chemistry Research*, 56(45), 13050–13063. <https://doi.org/10.1021/acs.iecr.7b01327>
- Cheng, J. C., & Fox, R. O. (2010). Kinetic Modeling of Nanoprecipitation using CFD Coupled with a Population Balance. *Industrial & Engineering Chemistry Research*, 49(21), 10651–10662. <https://doi.org/10.1021/ie100558n>
- Cheng, J., Feng, X., Cheng, D., & Yang, C. (2012). Retrospect and Perspective of Micromixing Studies in Stirred Tanks. *Chinese Journal of Chemical Engineering*, 20(1), 178–190. [https://doi.org/10.1016/S1004-9541\(12\)60378-4](https://doi.org/10.1016/S1004-9541(12)60378-4)

- Commence, J.-M., & Falk, L. (2011). Villermaux–Dushman protocol for experimental characterization of micromixers. *Chemical Engineering and Processing: Process Intensification*, 50(10), 979–990. <https://doi.org/10.1016/j.cep.2011.06.006>
- Coroneo, M., Montante, G., Paglianti, A., & Magelli, F. (2011). CFD prediction of fluid flow and mixing in stirred tanks: Numerical issues about the RANS simulations. *Computers and Chemical Engineering*, 35(10), 1959–1968. <https://doi.org/10.1016/j.compchemeng.2010.12.007>
- Costa, P., & Trevisoi, C. (1972). Reactions with non-linear kinetics in partially segregated fluids. *Chemical Engineering Science*, 27(11), 2041–2054. [https://doi.org/10.1016/0009-2509\(72\)87062-3](https://doi.org/10.1016/0009-2509(72)87062-3)
- Duan, X., Feng, X., Mao, Z. S., & Yang, C. (2019). Numerical simulation of reactive mixing process in a stirred reactor with the DQMOM-IEM model. *Chemical Engineering Journal*, 360, 1177–1187. <https://doi.org/10.1016/j.cej.2018.10.156>
- Duan, X., Feng, X., Peng, C., Yang, C., & Mao, Z.-S. (2020). Numerical simulation of micro-mixing in gas-liquid and solid-liquid stirred tanks with the coupled CFD-E-model. *Chinese Journal of Chemical Engineering*. <https://doi.org/10.1016/j.cjche.2020.06.016>
- Duan, X., Feng, X., Yang, C., & Mao, Z. (2018). CFD modeling of turbulent reacting flow in a semi-batch stirred-tank reactor. *Chinese Journal of Chemical Engineering*, 26(4), 675–683. <https://doi.org/10.1016/j.cjche.2017.05.014>
- Duan, X., Feng, X., Yang, C., & Mao, Z. S. (2016a). Numerical simulation of micro-mixing in stirred reactors using the engulfment model coupled with CFD. *Chemical Engineering Science*, 140, 179–188. <https://doi.org/10.1016/j.ces.2015.10.017>
- Duan, X., Feng, X., Yang, C., & Mao, Z. S. (2016b). Numerical simulation of micro-mixing in stirred reactors using the engulfment model coupled with CFD. *Chemical Engineering Science*, 140, 179–188. <https://doi.org/10.1016/j.ces.2015.10.017>

- Fitschen, J., Hofmann, S., Wutz, J., Kameke, A. v., Hoffmann, M., Wucherpfennig, T., & Schlüter, M. (2021). Novel evaluation method to determine the local mixing time distribution in stirred tank reactors. *Chemical Engineering Science: X*, 10, 100098. <https://doi.org/10.1016/j.cesx.2021.100098>
- Fournier, M. C., Falk, L., & Villermaux, J. (1996). A new parallel competing reaction system for assessing micromixing efficiency - Experimental approach. *Chemical Engineering Science*, 51(22), 5053–5064. [https://doi.org/10.1016/0009-2509\(96\)00270-9](https://doi.org/10.1016/0009-2509(96)00270-9)
- Fournier, M.-C., Falk, L., & Villermaux, J. (1996). A new parallel competing reaction system for assessing micromixing efficiency—Determination of micromixing time by a simple mixing model. *Chemical Engineering Science*, 51(23), 5187–5192. [https://doi.org/10.1016/S0009-2509\(96\)00340-5](https://doi.org/10.1016/S0009-2509(96)00340-5)
- Fox, R. O. (2003). Computational Models for Turbulent Reacting Flows. In *Computational Models for Turbulent Reacting Flows*. <https://doi.org/10.1017/cbo9780511610103>
- Gao, Z., Li, D., Buffo, A., Podgórska, W., & Marchisio, D. L. (2016). Simulation of droplet breakage in turbulent liquid–liquid dispersions with CFD-PBM: Comparison of breakage kernels. *Chemical Engineering Science*, 142, 277–288. <https://doi.org/10.1016/j.ces.2015.11.040>
- Gavi, E., Marchisio, D. L., & Barresi, A. A. (2007). CFD modelling and scale-up of Confined Impinging Jet Reactors. *Chemical Engineering Science*, 62(8), 2228–2241. <https://doi.org/10.1016/j.ces.2006.12.077>
- Grenville, R. K. (1992). *Blending of viscous Newtonian and pseudo-plastic fluids*. Cranfield Institute of Technology.
- Guichardon, P., & Falk, L. (2000). Characterisation of micromixing efficiency by the iodide-iodate reaction system. Part I: Experimental procedure. *Chemical Engineering Science*, 55(19), 4233–4243. [https://doi.org/10.1016/S0009-2509\(00\)00068-3](https://doi.org/10.1016/S0009-2509(00)00068-3)

- Habchi, C., Lemenand, T., Valle, D. Della, Khaled, M., Elmarakbi, A., & Peerhossaini, H. (2014). Mixing assessment by chemical probe. *Journal of Industrial and Engineering Chemistry*, 20(4), 1411–1420. <https://doi.org/10.1016/J.JIEC.2013.07.026>
- Haringa, C. (2022). An analysis of organism lifelines in an industrial bioreactor using Lattice-Boltzmann CFD. *Engineering in Life Sciences*. <https://doi.org/10.1002/elsc.202100159>
- Haworth, D. C. (2010). Progress in probability density function methods for turbulent reacting flows. *Progress in Energy and Combustion Science*, 36(2), 168–259. <https://doi.org/10.1016/j.pecs.2009.09.003>
- Hofinger, J., Sharpe, R. W., Bujalski, W., Bakalis, S., Assirelli, M., Eaglesham, A., & Nienow, A. W. (2011). Micromixing in two-phase (G-L and S-L) systems in a stirred vessel. *The Canadian Journal of Chemical Engineering*, 89(5), 1029–1039. <https://doi.org/10.1002/cjce.20494>
- Johnson, B. K., & Prud'homme, R. K. (2003). Chemical processing and micromixing in confined impinging jets. *AIChE Journal*, 49(9), 2264–2282. <https://doi.org/10.1002/aic.690490905>
- Kölbl, A., & Schmidt-Lehr, S. (2010a). The iodide iodate reaction method: The choice of the acid. *Chemical Engineering Science*, 65(5), 1897–1901. <https://doi.org/10.1016/j.ces.2009.11.032>
- Kölbl, A., & Schmidt-Lehr, S. (2010b). The iodide iodate reaction method: The choice of the acid. *Chemical Engineering Science*, 65(5), 1897–1901. <https://doi.org/10.1016/j.ces.2009.11.032>
- Kotowicz, M., & Jasińska, M. (2021). An improved model for interpretation of micromixing experiment with iodide–iodate method and sulphuric acid. *Chemical Engineering Research and Design*, 165, 270–279. <https://doi.org/10.1016/j.cherd.2020.10.035>

- Kresta, S. M., Etechells III, A. W., Dickey, D. S., & Atiemo-Obeng, V. A. (2016). Advances in Industrial Mixing: A Companion to the Handbook of Industrial Mixing. In *CFD Modeling of Stirred Tank Reactors* (pp. 123–148). John Wiley & Sons.
- Kuschel, M., Fitschen, J., Hoffmann, M., von Kameke, A., Schlüter, M., & Wucherpennig, T. (2021). Validation of Novel Lattice Boltzmann Large Eddy Simulations (LB LES) for Equipment Characterization in Biopharma. *Processes*, 9(6), 950. <https://doi.org/10.3390/pr9060950>
- L. Marchisio, D., & A. Barresi, A. (2003). CFD simulation of mixing and reaction: the relevance of the micro-mixing model. *Chemical Engineering Science*, 58(16), 3579–3587. [https://doi.org/10.1016/S0009-2509\(03\)00264-1](https://doi.org/10.1016/S0009-2509(03)00264-1)
- Lavino, A. D., Ferrari, M., Barresi, A. A., & Marchisio, D. L. (2021). Effect of different good solvents in flash nano-precipitation via multi-scale population balance modeling-CFD coupling approach. *Chemical Engineering Science*, 245, 116833. <https://doi.org/10.1016/j.ces.2021.116833>
- Lindenberg, C., Schöll, J., Vicum, L., Mazzotti, M., & Brozio, J. (2008). Experimental characterization and multi-scale modeling of mixing in static mixers. *Chemical Engineering Science*, 63(16), 4135–4149. <https://doi.org/10.1016/j.ces.2008.05.026>
- Liu, Y., & Fox, R. O. (2006). CFD predictions for chemical processing in a confined impinging-jets reactor. *AIChE Journal*, 52(2), 731–744. <https://doi.org/10.1002/aic.10633>
- Madadi-Kandjani, E., Fox, R. O., & Passalacqua, A. (2017). Application of the Fokker-Planck molecular mixing model to turbulent scalar mixing using moment methods. *Physics of Fluids*, 29(6), 065109. <https://doi.org/10.1063/1.4989421>
- Maluta, F., Paglianti, A., & Montante, G. (2021). Two-fluids RANS predictions of gas cavities, power consumption, mixing time and oxygen transfer rate in an aerated fermenter scale-down stirred with multiple impellers. *Biochemical Engineering Journal*, 166, 107867. <https://doi.org/10.1016/j.bej.2020.107867>

- Manzano Martínez, A. N., Haase, A. S., Assirelli, M., & van der Schaaf, J. (2020). Alternative Kinetic Model of the Iodide–Iodate Reaction for Its Use in Micromixing Investigations. *Industrial & Engineering Chemistry Research*, 59(49), 21359–21370. <https://doi.org/10.1021/acs.iecr.0c04901>
- Manzano Martínez, A. N., Haase, A. S., Assirelli, M., & Van Der Schaaf, J. (2020). Alternative Kinetic Model of the Iodide-Iodate Reaction for Its Use in Micromixing Investigations. *Industrial and Engineering Chemistry Research*, 59(49), 21359–21370. <https://doi.org/10.1021/acs.iecr.0c04901>
- Mao, Z., & Yang, C. (2017). Micro-mixing in chemical reactors: A perspective. In *Chinese Journal of Chemical Engineering* (Vol. 25, Issue 4, pp. 381–390). Chemical Industry Press. <https://doi.org/10.1016/j.cjche.2016.09.012>
- Marchisio, D. L. (2009). Large Eddy Simulation of mixing and reaction in a Confined Impinging Jets Reactor. *Computers & Chemical Engineering*, 33(2), 408–420. <https://doi.org/10.1016/j.compchemeng.2008.11.009>
- Marchisio, D. L., & Fox, R. O. (2005). Solution of population balance equations using the direct quadrature method of moments. *Journal of Aerosol Science*, 36(1), 43–73. <https://doi.org/10.1016/j.jaerosci.2004.07.009>
- McMaster-Carr*. (n.d.). Retrieved April 8, 2022, from <https://www.mcmaster.com/>
- Nienow, A. W. (2014). Stirring and Stirred-Tank Reactors. *Chemie Ingenieur Technik*, 86(12), 2063–2074. <https://doi.org/10.1002/cite.201400087>
- Öncül, A. A., Janiga, G., & Thévenin, D. (2009). Comparison of Various Micromixing Approaches for Computational Fluid Dynamics Simulation of Barium Sulfate Precipitation in Tubular Reactors. *Industrial & Engineering Chemistry Research*, 48(2), 999–1007. <https://doi.org/10.1021/ie800364k>
- Palmer, D. A., Ramette, R. W., & Mesmer, R. E. (1984). Triiodide ion formation equilibrium and activity coefficients in aqueous solution. *Journal of Solution Chemistry*, 13(9), 673–683. <https://doi.org/10.1007/BF00650374>

- Para, M. L., Alidoost, M., Shiea, M., Boccardo, G., Buffo, A., Barresi, A. A., & Marchisio, D. L. (2022). A modelling and experimental study on the co-precipitation of Ni_{0.8}Mn_{0.1}Co_{0.1}(OH)₂ as precursor for battery cathodes. *Chemical Engineering Science*, 254, 117634. <https://doi.org/10.1016/j.ces.2022.117634>
- Paul, E. L., Atiemo-Obeng, V. A., & Kresta, S. M. (2004). *Handbook of Industrial Mixing Science and Practice*. John Wiley & Sons.
- Qu, Y., Cheng, J., Mao, Z.-S., & Yang, C. (2021). A perspective review on mixing effect for modeling and simulation of reactive and antisolvent crystallization processes. *Reaction Chemistry & Engineering*, 6(2), 183–196. <https://doi.org/10.1039/D0RE00223B>
- Rave, K., Lehmenkühler, M., Wirz, D., Bart, H.-J., & Skoda, R. (2021). 3D flow simulation of a baffled stirred tank for an assessment of geometry simplifications and a scale-adaptive turbulence model. *Chemical Engineering Science*, 231, 116262. <https://doi.org/10.1016/j.ces.2020.116262>
- Rozen, A. (1995). Investigation of Micromixing in Viscous Liquids. In *Doktorat*. Warsaw University of Technology.
- Salome Platform - The open-source platform for numerical simulation*. (n.d.). Retrieved May 10, 2022, from <https://www.salome-platform.org/>
- Schikarski, T., Trzenschiok, H., Peukert, W., & Avila, M. (2019). Inflow boundary conditions determine T-mixer efficiency. *Reaction Chemistry & Engineering*, 4(3), 559–568. <https://doi.org/10.1039/C8RE00208H>
- Schwarzer, H.-C., & Peukert, W. (2004). Combined experimental/numerical study on the precipitation of nanoparticles. *AIChE Journal*, 50(12), 3234–3247. <https://doi.org/10.1002/aic.10277>
- Singh, H., Fletcher, D. F., & Nijdam, J. J. (2011). An assessment of different turbulence models for predicting flow in a baffled tank stirred with a Rushton turbine. *Chemical Engineering Science*, 66(23), 5976–5988. <https://doi.org/10.1016/j.ces.2011.08.018>

- Tang, Q., Zhao, W., Bockelie, M., & Fox, R. O. (2007). Multi-environment probability density function method for modelling turbulent combustion using realistic chemical kinetics. *Combustion Theory and Modelling*, 11(6), 889–907. <https://doi.org/10.1080/13647830701268890>
- Vicum, L., & Mazzotti, M. (2007). Multi-scale modeling of a mixing-precipitation process in a semibatch stirred tank. *Chemical Engineering Science*, 62(13), 3513–3527. <https://doi.org/10.1016/j.ces.2007.02.056>
- Vicum, L., Ottiger, S., Mazzotti, M., Makowski, Ł., & Bałdyga, J. (2004). Multi-scale modeling of a reactive mixing process in a semibatch stirred tank. *Chemical Engineering Science*, 59(8–9), 1767–1781. <https://doi.org/10.1016/j.ces.2004.01.032>
- Villermaux, J., & Falk, L. (1994). A generalized mixing model for initial contacting of reactive fluids. *Chemical Engineering Science*, 49(24), 5127–5140. [https://doi.org/10.1016/0009-2509\(94\)00303-3](https://doi.org/10.1016/0009-2509(94)00303-3)
- Wang, L., & Fox, R. O. (2004). Comparison of micromixing models for CFD simulation of nanoparticle formation. *AIChE Journal*, 50(9), 2217–2232. <https://doi.org/10.1002/aic.10173>
- Wenzel, D., Assirelli, M., Rossen, H., Lopattschenko, M., & Górak, A. (2018). On the reactant concentration and the reaction kinetics in the Villermaux-Dushman protocol. *Chemical Engineering and Processing - Process Intensification*, 130, 332–341. <https://doi.org/10.1016/j.cep.2018.06.022>
- Yang, H.-J., Chu, G.-W., Zhang, J.-W., Shen, Z.-G., & Chen, J.-F. (2005). Micromixing Efficiency in a Rotating Packed Bed: Experiments and Simulation. *Industrial & Engineering Chemistry Research*, 44(20), 7730–7737. <https://doi.org/10.1021/ie0503646>

APPENDIX A: CALIBRATION PROCEDURES

Calibration procedures followed the work of Fournier et al. (1996), Assirelli (2002), and Tunestal (2012). The calibration has 12 different concentrations of triiodide ion. Three different stock solutions were prepared and used for calibration to ensure errors within the stock did not carry through the full set. The stock solutions had concentrations for potassium iodide (KI) and iodine (I₂) of 0.5 g/L and 0.2 g/L, respectively. The solutions were prepared by mixing different amounts of potassium iodide, iodine, and water in a 100 mL volumetric flask. The mixing ratios are summarized in Table A.1.

Table A.1: Mixing ratios for calibration on triiodide (I₃⁻).

Volume of Potassium Iodide (KI) Solution (mL)	Volume of Iodine (I ₂) Solution (mL)	Volume of Water (mL)
2	25	73
5	25	70
10	25	65
15	25	60
2	50	48
5	50	45
10	50	40
15	50	35
2	75	23
5	75	20
10	75	15
15	75	10

Figure A.1 shows results of the calibration curve for triiodide. This evaluation was carried out by measuring the UV readings of mixtures containing iodine (I₂) and iodide ion (I⁻) with various concentrations. The equilibrium triiodide ion (I₃⁻) concentration was then determined through the equilibrium constant. Its value corresponds to 786 L/mol at 20 °C. The slope of the line in Figure A.1 corresponds to the extinction coefficient at 353 nm for triiodide and was determined to be 2 227.2 m²/mol. The value is in good agreement with literature data and typically ranges between 2 200 and 2 600 m²/mol (Pinot et al., 2014).

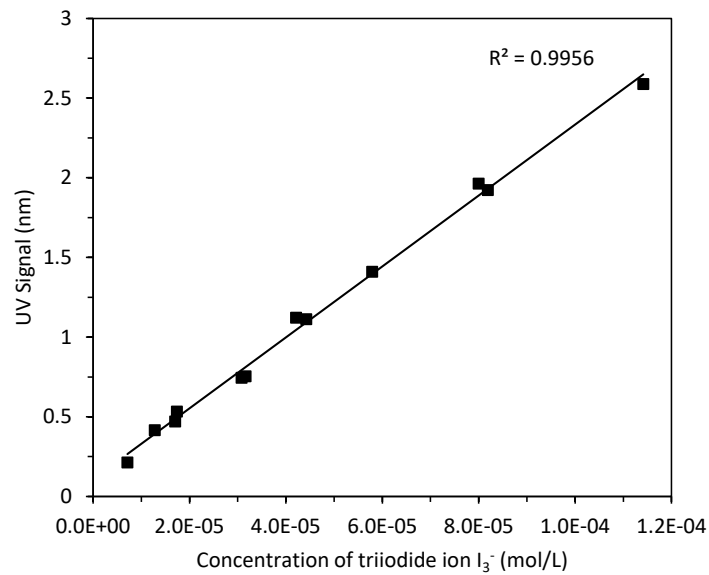


Figure A.1: Calibration curve for triiodide ion performed for various concentrations of iodide ion and iodine in water.